5-2009

Patient-specific quality assurance for IMRT

Michelle Lynn Neeley
University of Tennessee

To the Graduate Council:

I am submitting herewith a thesis written by Michelle Lynn Neeley entitled "Patient-specific quality assurance for IMRT." I have examined the final electronic copy of this thesis for form and content and recommend that it be accepted in partial fulfillment of the requirements for the degree of Master of Science, with a major in Physics.

Marianne Breinig, Major Professor

We have read this thesis and recommend its acceptance:

Accepted for the Council:
Carolyn R. Hodges

Vice Provost and Dean of the Graduate School

(Original signatures are on file with official student records.)

To the Graduate Council:

I am submitting herewith a thesis written by Michelle Lynn Neeley entitled “Patient-Specific Quality Assurance for IMRT.” I have examined the final electronic copy of this thesis for form and content and recommend that it be accepted in partial fulfillment of the requirements for the degree of Master of Science, with a major in Physics.

Marianne Breinig

Major Professor

We have read this thesis
and recommend its acceptance:

Chester Ramsey

Katherine Grzywacz Jones

Accepted for the Council:

Carolyn R. Hodges

Vice Provost and Dean of the Graduate School

(Original signatures are on file with official student records.)

Patient-Specific Quality Assurance for IMRT

A Thesis Presented for
the Master of Science Degree
The University of Tennessee, Knoxville

Michelle Lynn Neeley
May 2009

ACKNOWLEDGEMENTS

I would like to thank everyone who contributed to my learning at the Thompson Cancer Survival Center and especially to Dr. Chester Ramsey. With out his guidance, encouragement, and creative thought, the following studies would have never been possible.

ABSTRACT

In radiation therapy, QA is an integral part of the IMRT treatment process. This study evaluated two different QA modalities, a heterogeneous RANDO phantom and the MatriXX Detector. The RANDO phantom study evaluated the dosimetric accuracy of a helical TomoTherapy system which resulted in a benchmark being established for dosimetric accuracy in heterogeneous materials. The MatriXX study evaluated the performance of the MatriXX Detector to determine if it could be used as a substitute for radiographic film in rotational IMRT delivery techniques. At least twenty test cases were selected for each study, and treatment plans were created using the Hi-Art TomoTherapy treatment planning and delivery system. Kodak EDR2 radiographic films were used and processed in batches of five films at least one hour after irradiation. Horizontal profiles, vertical profiles, and Gamma pass/fail plots were calculated for each test case. For the Gamma calculations, the threshold parameters were set to a 3% dose difference and a 3-mm distance-to-agreement.

Analysis of the gamma pass/fail plots for the RANDO phantom study showed the lung cases had 27.2% of the pixels exceeding gamma, while the prostate patients had 14.7%. For the prostate test cases, only two of the films had greater than 20% of the pixels exceeding the gamma threshold, while only four of the lung test cases were below the 20% pixel threshold. Analysis of the gamma pass/fail plots from the MatriXX study showed the percent of pixels exceeding gamma was 10.8 ± 6.7% for the film verses 23.4 ± 13.8% for the

MatriXX detector. The MatriXX appears to function well in high-dose low-gradient regions and low-dose low-gradient regions. However, the MatriXX has difficulty in regions with steep dose gradients due to volume averaging across the ion chambers, and the coarse 7.62 mm center-to-center spacing of the chambers. The RANDO phantom study analysis revealed that discrepancies between calculated and measured dose distributions occurred at tissue-bone interfaces. Further investigation will be needed to determine if these errors are due to film response at heterogeneous tissue interfaces or from actual dose calculation errors in the treatment planning system.

PREFACE

This work is divided into six chapters. The first three chapters provide an introduction to medical physics and radiation therapy, the clinical accelerators used in this study, and the need for quality assurance and the modalities used. The last three chapters cover the study set-up, results, and conclusion. Figures corresponding to the study are found in Appendix I and tables in Appendix II. Portions of this work were taken from supporting documents submitted to the 50th annual American Association of Physicists in Medicine meeting (AAPM). Those documents were a collaboration between Dr. Chester Ramsey and me. The RANDO phantom study was presented at the 50th annual AAPM meeting.

TABLE OF CONTENTS

Chapter **Page**

LIST OF TABLES

Table **Page**

LIST OF FIGURES

Figure **Page**

Chapter 1

Introduction

1.1 Medical Physics and Radiation Therapy

The primary use of radiation therapy is to eliminate cancerous cell populations. These cell populations are identified through an imaging modality such as computed tomography (CT) or positron emission tomography (PET). Once identified, these cell populations are exposed to fields of ionizing radiation which damage the cells' DNA eventually causing cell death. Ionizing radiation can be delivered using a clinical linear accelerator or using radioactive materials. Brachytherapy is a form of cancer treatment that uses small radioisotopes placed inside a body cavity delivering gamma rays to the surrounding tissue. The most common form of radiation delivery is through the use of a linear accelerator or linac. Linacs deliver external beam radiation therapy by utilizing ionizing radiation to penetrate a cancerous cell population and deliver a prescribed dose. The prescribed dose is achieved in multiple fractions using a beam that is shaped and delivered from multiple angles sparing as much healthy surrounding tissue as possible.

Medical physics is an applied branch of physics that is concerned with the safe delivery of radiation in order to achieve a therapeutic effect. As a patient progresses through the cancer treatment process, many people play an active role. The medical physicist's role is to ensure radiation safety, help to develop

new therapeutic techniques, collaborate with the radiation oncologists to design treatment plans, and to monitor equipment and patient procedures through quality assurance [1].

1.2 Biological Effects of Radiation

When external beam radiation is chosen as the cancer treatment modality, it is delivered using a linac. Both electrons and photons are used in cancer treatment and are forms of ionizing radiation. Electrons are directly ionizing due to the fact that they have enough kinetic energy to produce ionizing effects through collisions as they penetrate through matter. This is better known as the bremsstrahlung process. The electron interactions are provoked by the Coulomb force between the electric field of the penetrating electron and the electric fields of the orbital electrons and nuclei of atoms in the material. In radiation therapy, electron energies range from 6MeV (mega-electron volts) up to 20MeV.

Photons are an indirect form of ionizing radiation. They liberate directly ionizing particles, such as electrons, from matter during their interactions. When photons are used in radiation therapy, their ionization ability is dominated by the Compton process [2]. In the Compton process, the initial photon interacts with a free electron in matter (an electron whose binding energy is very small compared to the energy of the initial photon) transferring part or all of its energy creating a fast electron. The fast electron then directly ionizes the surrounding matter. If the initial photon didn't transfer all of its energy, it will continue on a

deflected path repeating the Compton process until it transfers all of its energy. The fast electrons produced are able to ionize other atoms of the material, break vital chemical bonds, and ultimately lead to the chain of events known as biological damage [2].

The biologic effects of the x-rays can be a result of a direct action from the fast electrons or an indirect action. A direct action is when the fast electron or recoil electron directly ionizes the target molecule. An indirect action is when the fast electrons interact with another molecule, such as water, to produce a radical which interacts with the target molecule causing damage. The majority of damage from x-rays is caused by indirect action to the target molecule's DNA. In radiation therapy, the allowable photon energies are 6MV (mega volts) to 18MV.

CHAPTER 2

CLINICAL ACCELERATORS

2.1 Basic Components

The prescribed dose of radiation is delivered using a linac. Linacs use high-frequency electromagnetic waves to accelerate charged particles, such as electrons, to high energies through a linear accelerating tube. The high-energy electron beam can be used for treating superficial tumors, or it can be made to strike a target producing x-rays for treating deep-seated tumors [3, 4]. A linac has two main parts, a stand and the gantry. These two parts house all the necessary internal components for operation. All linacs have the same basic internal components. The components found in the stand are a cooling water system, power supply, modulator, klystron/magnetron, waveguide, and circulator. The electron gun, accelerating structure, and bending magnet are found in the gantry. These components are shown in Figures 1 and 2. All figures are found in Appendix I.

The cooling water system is a necessary element found in the base of the stand which has two functions. First, it cools parts of the accelerator that dissipate energy as heat, and secondly, it keeps the accelerator at a stable operating temperature that is above room temperature in order to avoid condensation from forming inside the accelerator. The power supply provides direct (DC) power to the modulator, which produces high-voltage, flat-toped DC

pulses that are microseconds in duration. These pulses are sent simultaneously to the electron gun and the magnetron/klystron. The klystron/magnetron uses the high-voltage DC pulses to produce pulsed microwaves which are carried via the waveguide to the accelerating structure. Klystrons are used in high-energy accelerators due to the fact that they can deliver higher power levels which are required as the beam energy reaches greater than 12MV.

Although it may be more expensive, most linacs contain circulators. This is a device that is inserted into the waveguide to stop microwaves from being reflected back into the klystron/magnetron via the waveguide. If reflected microwaves were able to reach the klystron, it would damage or detune the structure resulting in the inability to produce microwaves. The electron gun is located at the end of the accelerating structure near the waveguide. The electron gun is a simple cathode that injects electrons into the accelerating structure. These electrons are energized by the pulsed microwaves from the klystron/magnetron. In the accelerating structure, the electrons are sent through a linear series of cavities.

Most accelerating structures in present-day linacs are standing wave accelerators due to the fact that they are much shorter than traveling wave accelerating structures. The electric wave in a standing wave accelerator varies in magnitude with time in a sinusoidal pattern, but remains stationary along the axis (not advancing). This can be visualized by imaging a string fixed at both ends, but oscillating up and down. As the electric field oscillates, the electrons

are accelerated forward through the structure. With every pulsed microwave, a new group of electrons are accelerated down the structure resulting in incident and reflected waves. These incident and reflected waves combine to produce standing waves that oscillate back and forth approximately one hundred times during a five microsecond pulse [3]. The resulting standing waves have stationary nodes that are located within every other cavity of the accelerating structure and contain no electric field. Because there is no electric field in the nodal cavities, they do not contribute to the acceleration of the electrons. These cavities can therefore be moved off axis and shortened due to the fact that the resonance of a cavity is not based on length, but diameter. This results in shortening of the whole structure. After the electrons pass through the accelerating structure, they are sent into the bending magnet which deflects the electrons into a 270^{o} loop focusing the electron beam.

2.2 The Gantry Head

The gantry head is a very important component of the linac. This is where beam shaping, localizing, and monitoring take place [3]. The gantry head not only contains the bending magnet, but the retractable x-ray target, flattening filter, scattering foils, ionization chambers, and the collimators (primary and secondary) as seen in figures 3 and 4. The retractable x-ray target is a thin, high Z material, such as tungsten, that produces photons when bombarded with electrons. The resulting photon beam is forward peaked meaning that the greatest intensity of

photons are near the beam's central axis and less intense elsewhere. To correct the forward peaked beam, a very thin, conical metal absorber is placed in front of the beam. This allows for absorption of photons from the more intense region of the central axis resulting in a uniform dose distribution across the beam.

In electron therapy, the x-ray target and flattening filter are retracted and the scattering foil is inserted into the path of the electron beam. The scattering foil spreads out the focused beam coming from the bending magnet (figure 5). The scattering foil is only used for electron therapy. As figure 5 shows, there is a set of ion chambers that sit below the carousel for the flattening filter and scattering foil. This set of ion chambers samples the radiation beam (photons or electrons) as it passes through the head of the gantry. These ion chambers send a signal back to the treatment control station reporting how much dose has been delivered, and terminates the treatment when the prescribed dose has been achieved. The purpose for having two ion chambers is simply to have two independent measurements using one measurement to check the other.

The last important component of the gantry head is the primary and secondary collimators. As seen in figures 4 and 5, the primary collimator sits just below the x-ray target and initially shapes the photon beam, where as the electron beam is still focused and passes through to the scattering foil. The secondary collimator is a set of four, thick tungsten blocks that move in pairs. These pairs are called jaws, and they help create sharp edges on all sides of the electron or photon beam. These sharp beam edges are necessary to minimize

penumbra. Penumbra is the region at the edge of the radiation beam where dose changes rapidly as a function of distance from the beam axis. The jaws can create field sizes up to 40 x 40 cm at a distance of 1 meter from the target.

A special case of collimation for treatment fields that are not rectangular in shape is the use of a multileaf collimator (MLC) (figure 6). The MLC is built into the gantry head and is found below the secondary collimator. It is the last component that the beam passes through before entering the patient. The MLC is typically made up of 80 (40 pairs) collimating blocks or leaves that are independently motor driven to produce a field of any shape or size up to 40cm x 40cm. Each MLC is made out of tungsten, and collectively they have a leaf thickness sufficient enough to block 98% of the photon beam at any given position [4]. This allows for a more conformal treatment area that targets the tumor volume and spares healthy surrounding tissue.

2.3 Varian Clinac 2100 EX

The Thompson Cancer Survival Center (TCSC) has two clinical linear accelerators, one of which being a Varian Clinac 2100 EX (Varian Medical Systems, Palo Alto, CA) and the other a HI-ART TomoTherapy linac (TomoTherapy, Inc., Madison, WI). The Varian 21EX is the most prevalent type of linac used in cancer treatment. The linac consists of the stand and gantry which both house the same basic components and design as mentioned above. In this machine, the standing waveguide is used in conjunction with a triode

electron gun. A triode gun uses an additional grid to control the electron beam current, which is normally held negative to the cathode, in order to cut off the current to the anode. By using this design, the additional grid is able to control the timing and magnitude of the current pulses injected into the accelerating structure.

The Varian 21EX is klystron driven with allowable photon energies of 6 MV and 18 MV, and allowable electron energies ranging from 6 MeV to 20 MeV. The linac has the capability of delivering dose from 100 to 600 MU/min to field sizes ranging from as small as 0.5 cm^2 up to 40.0 cm^2. The Varian 21EX employs a 120-tungsten leaf MLC consisting of fifteen 1cm thick leaves at the top and bottom of the MLC carriage and thirty 0.5 cm thick leaves in the middle of the MLC allowing for greater conformity around the target. The Varian 21EX has image guidance capabilities referred to as PortalVision. Portal Vision is a megavoltage imaging system used to ensure treatment plan verification, accurate patient setup, and effective treatment delivery. PortalVision takes low energy x-rays allowing clinicians to ensure the patient is properly set-up and the target volume is in the treatment area [5].

The Varian 21EX employs a hydraulic treatment couch that is capable of withstanding 300+ pounds and moves vertically and horizontally for patient positioning. The Varian 21EX at TCSC was manufactured so that its isocenter is located at 100 cm from the target source in the gantry head. The machine's isocenter is the imaginary intersection point in space of the axis of rotation of the

collimator and the axis of rotation of the gantry. Patients are typically set up using wall and ceiling mounted lasers placing the center of the target tissue at isocenter.

2.4 Tomotherapy

Besides traditional linear accelerators, there is Tomotherapy (figure 7). Tomotherapy is a linear accelerator with CT capability that is designed to deliver a more conformal dose distribution for Intensity Modulated Radiation Therapy (IMRT) treatments. The machine's design is based largely on the concept of a CT scanner. Internally, Tomotherapy geometrically employs a ring gantry design with a binary multi-leaf collimator which rotates simultaneously with the couch's linear motion into the gantry bore. This results in delivery of a continuous, helical (360^{o}) dose pattern around the patient (Figure 8).

Tomotherapy contains all the major components of a traditional linear accelerator and are arranged to fit inside the doughnut-like shape of the machine. Tomotherapy employs a 3GHz magnetron to produce pulsed microwaves instead of a klystron due to the low energy needed for treatment. A 6MV linear accelerator is mounted on the ring gantry which delivers an IMRT treatment plan specific to each patient. Opposite the treatment head is a 13cm thick lead counter weight attached to the gantry that acts as a rotating beam stopper. Tomotherapy's binary MLC consists of 64 tungsten leaves that are individually 10cm high.

The MLC defines the treatment field as a narrow open slit creating a wide fan beam in the axial direction. The maximum width of the projected beam to the axis is 40 cm, thus defining the maximum width for any patient treatment field as 40 cm. During treatment, the MLC leaves are either open or closed, and each leaf moves independently to modulate and shape the beam as the gantry moves around the patient. As the gantry rotates, Tomotherapy's couch is designed to move the patient at a constant velocity into the gantry bore and a maximum of 160 cm during the course of treatment. This defines the maximum length of any patient treatment field to be 160 cm. Because Tomotherapy's couch is designed to move during treatment, a larger volume can be treated in one set-up.

The fan beam design of Tomotherapy allows radiation to be delivered in a slice-by-slice manner. Tumor volumes are subdivided into a stack of slices that are independently irradiated and collectively result in a 3D conformal dose distribution. Tomotherapy employs 51 beams spaced roughly seven degrees apart creating a continuous treatment field [6, 7]. Because of Tomotherapy's dynamic nature, it is critical that the couch, gantry, and MLC leaves are all in sync.

Tomotherapy is an example of Image-Guided Radiation Therapy (IGRT). The linac is designed with a built-in CT scanner which provides image guidance in the treatment room. MVCT (megavoltage CT) imaging is performed prior to each treatment to ensure the patient is correctly placed on the treatment couch, and to confirm the tumor volume resides within the volume to be treated. The

resulting MVCT images are fused and registered with the planning CT images at the treatment console to determine if the patient needs to be repositioned for treatment. Tomotherapy's couch automatically adjusts the patient vertically and longitudinally to account for roll. To account for yaw and pitch, patient immobilization and positioning devices are used during treatment. The use of IGRT before treatment has helped to identify the exact 3D location of tumor volumes on a daily basis while sparing health surrounding tissue [6].

CHAPTER 3

QUALITY ASSURANCE

In static external beam photon radiation therapy treatments, the photon beam has a uniform intensity across the field. Because of this, a simple hand calculation can be performed independent of the planning station to verify the dose being delivered to the patient and the planning station dose are in agreement. With recent technological advances, linear accelerators have the ability to deliver IMRT treatments. IMRT treatments do not have a uniform intensity across the field. Instead, the intensity is modulated by the MLC and delivered from a multitude of beam angles to make an optimal composite dose distribution.

Because the field is not uniform, a hand calculation is impossible to perform, and therefore, the dose must be verified using another modality. A protocol for patient-specific quality assurance (QA) was developed to solve this problem and has become a major component of the IMRT clinical process [8]. The objective of this often time-intensive measurement process is to verify that the prescribed dose is accurately being delivered to the target volume (tumor) while sparing the healthy surrounding tissue. This study investigates two different modalities for IMRT QA, evaluates the dosimetric accuracy of both a helical tomotherapy system and Varian linac system, and investigates the benefits of constant dose rate (CDR) VMAT delivery techniques.

3.1 IMRT Treatments

The main objective of IMRT is to treat patients from a number of different angles with non-uniform intensity beams that have been optimized to deliver a high dose to the tumor and a very low dose to healthy surrounding tissue and critical structures. IMRT is a radiation delivery technique that uses inverse planning software to "shape" or conform a photon beam using a computer controlled MLC. The MLCs are employed as compensators to modify the intensity profile by moving in and out of the beam's path in order to meet the goals of a composite plan. This non-uniform fluence can be delivered to the patient from any angle.

As with any radiotherapy plan, a 3D CT data set is needed, along with image registration, critical structure contours, and beam selection and placement. For IMRT, the planning software must have the ability to create beam segments and contain an IMRT optimization algorithm. The user enters the dose criteria for the target (tumor) and critical structures. The software then optimizes the intensity profiles for each beam and calculates the composite dose distribution. After the generation of an acceptable IMRT plan, the intensity profiles for each beam are electronically transferred to the linear accelerator's delivery system [4].

There are three types of static IMRT delivery techniques, step-and-shoot, sliding window, and intensity modulated arc therapy (IMAT). Of these three techniques, step-and-shoot is the most widely used delivery technique, and the technique used in this study. In the step-and-shoot delivery technique, the

patient is treated with multiple beams that are individually subdivided into a series of segments or different shapes. These segments are created by the planning software, shaped using the MLC, and are delivered successively without operator intervention. Each beam segment produces a unique intensity profile, modulating the beam from segment to segment. After the completion of all segments for one beam angle, the operator must move the gantry to the next beam angle where the process repeats itself. The accelerator's beam is not turned on during MLC movement or gantry rotation resulting in its name, step-and-shoot IMRT. A subfield of step-and-shoot IMRT is dynamic-step-and-shoot. In this method the accelerator's beam is turned on throughout the delivery, even when the MLC leaves are moving. Tomotherapy employs this method of step-and-shoot IMRT.

IMAT takes the idea of dynamic step-and-shoot IMRT one step further. IMAT uses multiple beam angles to create a 360^{o} arc treatment in the linac's arc therapy mode. As in dynamic step-and-shoot, each field (arc) is divided into subfields of uniform intensity that collectively result in the desired intensity modulation. The MLCs are constantly moving and shaping the beam as the gantry rotates, while the accelerator's beam stays turned on throughout the treatment. One MLC subfield is delivered per gantry angle resulting in multiple overlapping fields. The number of gantry angles is determined by the gantry spacing set between each angle. The IMAT treatment planning algorithm divides the two-dimensional intensity distribution created by inverse planning into

multiple one-dimensional intensity profiles. These one-dimensional profiles are then decomposed into discrete intensity levels that are to be delivered by the subfields in a stack arrangement. The super imposed subfields create the intensity modulation at each gantry angle [9].

3.2 VMAT Treatments

IMRT does deliver more conformal dose distributions while sparing healthy surrounding tissue at the expense of longer treatment delivery times, multiple beam angles, and increased monitor units (MU). In radiation therapy, a monitor unit (MU) is a measure of machine output for a linear accelerator. Linear accelerators are calibrated for a specific energy such that 1 MU gives an absorbed dose of 1 centigray (cGy) at a depth of Dmax (or maximum dose) for a field size of 10x10 cm^2 for a source-to-axis (SAD) distance of 100 cm.

In an attempt to increase treatment efficiency, Volume Modulated Arc Therapy (VMAT) was developed. VMAT is a special type of IMRT in which radiation is delivered in single or multiple gantry rotations using a dynamic MLC and modulated gantry speeds. There are two types of VMAT, constant dose rate (CDR) and variable dose rate (VDR). CDR VMAT is when the dose rate is set at one specific rate throughout the treatment delivery. For example, the dose rate could be set to 300MU/min. VDR VMAT is when the dose rate changes throughout the treatment delivery. In VDR, the dose rate could be programmed to begin with 400 MU/min, then change to 200 MU/min at a specific gantry angle

partially through the treatment, and end with 600 MU/min. The main objective of VMAT is to deliver a treatment that is just as conformal, if not better, than a step-and-shoot IMRT treatment and hopefully, in less time. Before the invention of VMAT, Tomotherapy was the only efficient arc treatment technique available. With improvements in recent technology, conventional linacs will have the ability to deliver 360^{o} arc treatments with the instillation of the appropriate software upgrades [10, 11].

3.3 Devices Used

In order to perform patient specific QA, the composite IMRT dose distributions must be measured. Measurement of the dose distributions can be achieved using a wide variety of techniques and devices known as dosimeters. Some such devices include film (radiographic and radiochromic), ion chamber arrays (MatriXX Detector), diode arrays, and Electronic Portal Imaging Devices (EPIDs). Composite dose distributions are obtained by irradiating a test phantom containing dosimeter(s).

3.3.1 Phantoms, Film, and Ion Chambers

Of all the available modalities, film is still one of the most versatile and most frequently utilized measurement systems. When film is utilized as the dosimeter, it is placed in a coronal, sagittal, or transverse plane inside a phantom (figure 9). Because the film is irradiated using the same delivery sequence used

to treat the patient, the dose given to specific anatomical structures (such as the parotids, spinal cord, bladder, rectum etc…) can be evaluated.

Radiographic film and homogeneous solid water phantoms are commonly used in patient-specific quality assurance testing. At TCSC Kodak radiographic EDR2 film is commonly used. This type of film is used for doses delivered above 100 cGy, but below 600 cGy and comes sealed in a light safe jacket. Radiographic film consists of three layers. The first layer is a transparent film base made of polyester resin. The middle or second layer is a double emulsion containing very small crystals of silver bromide which is topped by another transparent film base. When the film is exposed to radiation (or visible light), the silver bromide crystals undergo a chemical change forming a latent image. When the film is developed, the crystals that have undergone a chemical change reduce to small grains of metallic silver. As the film is fixed, the unaffected silver bromide crystals are dissolved by the fixing solution resulting in a clear film. The metallic silver crystals are unaffected by the fixing solution resulting in a dark appearance, and thus a negative film results. The intensity of darkening on a film depends on the amount of metallic silver created by the radiation energy absorbed [12].

The darkness of the film can be measured by determining the optical density or absorbance of the film using a densitometer. A densitometer consists of a light source passing light through a diffusing screen incident on a small aperture. The film being tested sits on top of the aperture. The light transmitted

through the aperture and film is detected using a photocell. The photocell collects all light coming through the aperture regardless of its direction. The transmitted light is known as I_t. The amount of light detected when no film is in place is known as I_o. The optical density is calculated by comparing these two values using, $\log(I_o/I_t)$. The optical density is affected by radiation exposure and development procedures. To be a useful dosimeter, the film development must be carefully monitored to ensure the correct chemical(s), time, temperature, and agitation are taken into account. For each type of film used, a calibration of density versus exposure should be performed [4, 12]. This will be discussed further in chapter 5.

When using film as the dosimeter for patient specific QA, phantoms are used to simulate the patient. There are primarily two types of phantoms, homogeneous or heterogeneous. Homogeneous phantoms are made out of a material, referred to as solid water, which is the same density as human soft tissue. Solid water can come in the form of square blocks of different thicknesses or in the shape of a cylinder with a specific thickness (figure 10). Regardless of which form of solid water is used, the film is placed between two pieces of the phantom in a coronal, saggital, or transverse plane. Upon placement, the film is typically pricked with a pin to release any air bubbles in the film jacket and to create fiducial marks on the film. There are very few heterogeneous phantoms used in patient specific QA. One such phantom is the RANDO phantom. This phantom simulates the different densities of bone, soft

tissue, and air cavities in the body. These phantoms tend to be big, bulky, and heavy making QA set-up difficult and time consuming. Due to the fact that the treatment planning stations take into account patient heterogeneities, and not much is known about the accuracy of heterogeneous phantoms, most institutions do not use them regularly.

In conjunction with film and phantoms as QA modalities, ionization chambers are frequently used to measure absorbed dose at a specific point in the treatment volume. The ionization chamber is placed inside the phantom and connected to an electrometer where the charge collection is displayed in nanocoulombs. After irradiation, the ionization reading can then be converted into dose using equation 1.

$$D_w^Q = M k_Q N_{D,w}^{^{60}\mathrm{Co}} \qquad (1)$$

D^Q_w is the absorbed dose to water at the point of measurement of the ion chamber placed under reference conditions, M is the fully corrected ion chamber reading, k_Q is the quality conversion factor which converts the calibration factor for a ^{60}Co beam to that for a beam of quality Q, and $N^{60Co}_{D,W}$ is the ion chamber absorbed-dose-to-water calibration factor [4, 12, 13].

There are many different types of ionization chambers, but the most widely used for patient specific IMRT QA are thimble chambers. A basic ionization chamber is an enclosure containing two or more electrodes in which an electric current is passed when the enclosed gas is ionized by radiation. Specifically for this study, the gas used in thimble chambers is air and is ionized

using a photon beam. The design of thimble chambers takes on the look of a sewing thimble (figure 11). A low atomic numbered material is used for the walls, which are typically 5 mm thick, in order to have the same effective number as atmospheric air. Because of this, the materials of the wall and electrodes produce ionization essentially similar to that produced in a free-air ionization chamber. The inside of the solid chamber wall is made into an electrode by the application of a special material (graphite, Bakelite, or plastic coated graphite and Bakelite) to make it electrically conducting. The second electrode is a rod of low atomic number material (graphite or aluminum) that is held at the center of the thimble, but electrically insulated from it. In order to collect the ions produced from irradiation of the chamber, a voltage is applied between the two electrodes. Ion chambers do require periodic calibration [4, 12].

3.3.2 MatriXX Detector

Radiation therapy patients that are treated with Intensity Modulated Radiation Therapy (IMRT) and Volume Modulated Arc Therapy (VMAT) must have their calculated dose distributions verified with calculations and/or measurements as stated earlier. In the past, radiographic film has typically been used to measure and verify IMRT dose distributions as part of the quality assurance process. Many radiation therapy departments have transitioned to digital imaging systems, and the medical physicist(s) may no longer have access to chemical-based “wet” film processors. As a result, there are now a variety of

new media and devices that could potentially be used as a substitute for radiographic film. One such device is the IBA MatriXX Detector (IBA Dosimetry America, Bartlett, TN) (figure 12). The MatriXX is a vented ionization chamber array with 1020 separate 4.5 x 5 mm^2 ion chambers. Each chamber has a volume of 0.08 cm^3, and the detectors are spaced 7.62-mm center to center. The chambers are arranged in a 32 x 32 grid with an active area of 24.4 cm^2. The device itself has 3.3-mm of water equivalent material on the top surface, and 22-mm of backscatter material on the bottom. The MatriXX detector comes with its own software that has analysis capabilities, but it was not used for the analysis of this study [14].

CHAPTER IV

Quality Assurance Clinical Set-up and Experimental Specifications

In the discussion of the following studies regarding patient specific QA for IMRT, specific clinical set-ups were used and will now be described.

4.1 Rando Phantom

Heterogeneous phantoms that simulate the different tissue densities in the human body do exist, but are infrequently used for patient-specific IMRT QA. The potential advantage of using heterogeneous phantoms is that the measured dose distributions will more adequately reflect the clinical dose distributions in the patients. The use of homogenous phantoms during IMRT quality assurance can potentially mask errors that arise from limitations in the treatment planning system's modeling of density corrections. This study evaluated the dosimetric accuracy of a helical tomotherapy system using an anthropomorphic RANDO phantom for patient-specific QA. The results of this study allowed a benchmark to be established for dosimetric accuracy in heterogeneous materials.

Patient-specific IMRT dosimetric verification was performed for twenty-four patients using a male Alderson RANDO Phantom (The Phantom Laboratory,

Salem, NY) (figure 13). The complete male RANDO phantom represents a 5' 9", 163 lb human male and is separated transversely into 2.5-cm slices. Each slice consists of a natural human skeleton cast inside a material that is radiologically equivalent to human soft tissue. The soft tissue simulates human muscle tissue with randomly distributed fat. The lung portion of the phantom is made with a lower density material simulating human lungs in a median respiratory state molded to naturally fill the rib cage (figure14) [15]. For this study, the phantom was divided into two separate sections: 1.) A lung phantom consisting of slices 14 through 19; and 2.) A pelvic phantom consisting of slices 26 through 35. The setup of both phantom sections is shown in Figure 15.

In order to use the RANDO phantom for QA purposes, images of the phantom needed to be imported into the treatment planning station. This was done via a CT scan of each phantom (lung and pelvic). During "CT Simulation," the RANDO lung and pelvic sections were each placed in Vac-Lok cushions (CIVCO, Orange City, IA) in order to hold the phantom sections together and to help ensure a reproducible set-up for QA delivery. Vac-Lok cushions are inflatable bags that are filled with small Styrofoam balls. Once inflated, patients are typically placed on top of the bags in their specific treatment position. As the bag is deflated, it can be molded around the patient creating an outline of their shape and position. Vac-Lok cushions can also be used for phantoms, as in this case. Rigid molds of each phantom set-up were created and used for each of the patient-specific IMRT measurements.

In order to perform patient specific QA, QA treatment plans have to be created for each patient within the treatment planning station. This is accomplished by using the QA tools on the planning station to overlay the patient's optimized IMRT dose distribution onto a section of phantom and determine where the film should be placed if used as the dosimeter. The treatment planning station takes into account the difference in densities between the patient and the phantom and adjusts the dose distribution accordingly. If an ionization chamber is going to be used, the treatment planning station can calculate dose specifically for the location of the chamber in the phantom in order to compare the calculated dose with the measured dose obtained from the electrometer reading.

For the RANDO phantom study, treatment plans were created for 12 prostate and 12 lung patients using the Hi-Art TomoTherapy treatment planning and delivery system. For the lung cases, the gross tumor volume or clinical target volume (CTV) consisted of the primary tumor volume as visualized on CT or PET/CT. For the prostate test cases, the prostate CTV included the prostate gland and seminal vesicles. IMRT QA plans were created for each patient using the corresponding phantom section (lung or pelvis), and the QA plans were designed so the tumor volume from the patient resided in the same anatomical site inside the RANDO phantom.

To deliver the planned QA procedure, the corresponding phantom section was placed on the tomotherapy high-performance couch in the Vac-Lok cushion.

For the prostate test cases, an A1SL thimble ionization chamber (Standard Imaging, Middleton, WI) was placed in the phantom in the center of the target volume. Ionization chamber readings were not taken for the lung cases due to the random location of the tumor site within the lung. Kodak radiographic EDR2 film was placed in a transverse plane between two of the phantom slices for both the prostate and lung cases. The film was taped to the inside surface of the phantom to prevent film movement, and marked in three locations relative to the machine isocenter (Figure 16). The phantom was then compressed using a belt mechanism to eliminate gaps and air pockets between the phantom slices.

Once the phantom was correctly placed on the treatment table using the wall mounted lasers and prior to irradiation, the phantom was imaged using Tomotherapy's MVCT system. The MVCT images were fused with the treatment planning CT images using a pixel-by-pixel mutual information image registration algorithm. From the image registration, the phantom was automatically repositioned in the anterior-posterior, superior-inferior, and lateral directions by the high-performance couch. In addition, the roll corrections were automatically implemented by adjusting the treatment start angle within the treatment delivery system. Yaw and pitch corrections were applied manually by moving and then re-imaging the phantom until values of zero were obtained in the treatment delivery system.

After applying all the set-up corrections and correcting for pitch and yaw, the QA procedure was ready to be delivered. After irradiation, all EDR2 QA films

were processed at least one hour after exposure in batches of five films. The films were scanned using a Vidar 16 Dosimetry Pro (Vidar Systems, Herndon, VA) and analyzed using both the Tomotherapy IMRT QA software and the RIT dosimetry software (Radiological Imaging Technology, Colorado Springs, CO) (figure 17). The calculated dose distribution obtained during the QA procedure planning and the measured dose distribution obtained from irradiating the film were registered with one another using a fiducial-based registration system with the marks placed on the film prior to irradiation. In addition to the IMRT QA films, calibration films were also shot. The calibration films were shot on the Varian 21EX using a 13 segment step-and-shoot sequence (see chapter 5 for more information).

4.2 MatriXX Detector

The primary objective of this portion of the study was to determine if the MatriXX detector could be used as a substitute for radiographic film in rotational IMRT delivery techniques, such as Tomotherapy. In order to be useful for these delivery techniques, the device must be angular independent in dose-response and be capable of measuring composite dose distributions created during rotation. In order to evaluate its performance, the MatriXX and radiographic film measurements were taken using one Volume Modulated Arc Therapy (VMAT) and nineteen Helical Tomotherapy treatment deliveries.

Twenty random patients who were treated with helical tomotherapy during the Fall of 2007 were selected for this comparative analysis. The original clinical treatment plans were created and delivered using the TomoTherapy planning and delivery system (Version 3.1). Treatment planning for the VMAT test case was performed using the Pinnacle treatment planning system (Version 8.0, Philips Medical Systems, Bothell, WA) and delivered on the Varian 21EX. The VMAT treatment plan was created using Pinnacle's Direct Machine Parameter Optimization (DMPO) algorithm and was modeled and optimized as 51 equally-spaced fixed beams with one fixed MLC aperture per gantry angle. The plan was modeled this way due to the fact that VMAT planning software had not been developed yet.

The MatriXX detector was setup with a single 5 x 30 x 30-cm^3 slab of water-equivalent material (Solid Water, GAMMEX, Middleton, WI) centered over the detector array to provide sufficient buildup during treatment delivery. The device was positioned flat on the table top for coronal imaging with the electronics pointing toward the end of the couch in order to avoid the radiation field. Just as in the RANDO phantom experiment, the detector array in the MatriXX was CT imaged. A 50-cm field-of-view and a slice thickness of 2-mm were used as the imaging parameters. When the CT images were imported into the Tomotherapy treatment planning system, they were automatically down-sampled to 256 x 256 pixels in order to decrease computational times. As a result, the final pixel dimensions for the MatriXX after import was 2-mm^3. In order

to maintain consistency in the VMAT experiment, the down-sampled CT images of the MatriXX were also imported into Pinnacle and assigned as an IMRT phantom. The Tomotherapy and VMAT quality assurance plans were created in the respective planning systems by copying the patient's plan to the CT images of the MatriXX and re-computing the dose.

Measurements were performed with the MatriXX in the same setup and configuration as in the CT phantom plan. The MatriXX was initially positioned on the treatment table using the wall mounted lasers in the treatment room. For the Tomotherapy test cases, the MatriXX was MVCT imaged and repositioned for treatment using the same image-guidance technique as described in the RANDO phantom study excluding the pitch and yaw corrections. In order to compare the MatriXX with radiographic film, Kodak EDR2 film was placed on the surface of the MatriXX under the 5-cm thick slab of solid water. The position of the film relative to the machine isocenter was marked using a pin to prick the film jacket. The position of the MatriXX relative to the machine isocenter was determined relative to the center of the array. The same film calibration sequence used in the RANDO phantom study was also used in this study. All MatriXX QA films were processed at least one hour after exposure in batches of five films. The films were scanned using a Vidar 16 Dosimetry Pro and analyzed using the RIT dosimetry software.

CHAPTER V

Quality Assurance Analysis and Results

5.1 RIT Software Analysis

Because IMRT treatments are too complex for QA hand calculations, specific software is used in the IMRT QA analysis process. Radiological Imaging Technology (RIT) is recognized as one of the leading companies in automated IMRT QA analysis software. The RIT software has the ability to automatically calculate a variety of methods including gamma analysis, vertical and horizontal profiles, and addition and subtraction plots to analyze an IMRT treatment. If radiographic film is used as the QA dosimeter, the RIT software requires several initial tasks before the QA analysis can be performed. The software requires a film calibration curve, importation of the dose map from the treatment planning station (TPS), and registration between the film and the TPS dose map.

5.1.1 Film Calibration Dose to Density Curve

The film calibration curve is a calibration file created with in the RIT software using actual dose measurements taken on the linac to assign film pixel values a dose value. Several centimeters of solid water, a parallel-plate ionization chamber, and film are placed on the couch of the linac and positioned at the machine's isocenter. Several centimeters of solid water are used to prevent backscatter of radiation which would result in a false ionization chamber

reading. The film and ionization chamber are irradiated using a 13-step-and-shoot dynamic MLC file. This file is programmed to deliver 13 stripes of radiation with each consecutive strip delivering slightly less radiation. The ionization chamber is centered in the first stripe to acquire its ionization reading. Once the reading has been recorded, the chamber has to be physically moved to the next stripe in order to acquire the second stripe's reading. This results in running the dynamic MLC file 13 times to acquire ionization readings for all 13 stripes. Film is only used the first time the MLC file is ran to prevent saturation. Once the film is processed and scanned into the RIT software, the calibration curve can be created (figure 18). Using the parallel dose calibration option within the software allows the optical density of the 13 stripes on the scanned film to be assigned a dose value which is obtained from the ionization readings. The readings are converted to dose using equation 1. By creating this film calibration file and applying it to any film during the analysis process, the software is able to assign a dose value which corresponds to the film's optical density. Without this calibration file, the analysis software dose not know how to interpret the film's optical density, and therefore IMRT analysis can not be performed.

5.1.2 Film Registration

When analyzing IMRT QA films in RIT, registration between the film and the TPS dose image must be performed in order to define a coordinate system corresponding to both images. The TPS dose image is considered the

calculated image, i.e. what the film or measured image should look like after irradiation. The TPS dose image must be imported, and the irradiated film must be scanned into the RIT software. Once the film has been scanned into the software, the film calibration curve needs to be applied in order to assign dose to the irradiated parts of the film. Once the scanned film has been calibrated, the film and TPS dose image can be registered and analyzed. Registration between the two is typically performed using a fiducial-based registration system. Marks are placed on the film relative to the machine's isocenter prior to being radiated using a pin to prick the film jacket. This allows visible light through the light-safe film jacket in those areas causing saturation of the film.

Once the film is developed these fiducial marks appear as white dots (Figure 16). All films should be marked identically with respect to the machine's isocenter. By doing this, a coordinate-based template can be created in RIT. This template is then applied to both the film and TPS dose image during the registration process. The application of the template defines the corresponding coordinate system that links the two images for IMRT QA analysis. Registration can also be performed manually. This entails the user randomly selecting corresponding points between the TPS dose image and the film. This form of registration allows for a great deal of user error due to the limitation of the human eye, and therefore is not frequently used or recommended.

5.1.3 IMRT Analysis Profiles

After applying the calibration curve to the scanned film, and registering the TPS dose image and the film, RIT can perform the automated IMRT QA analysis. The software is programmed to compare the two images on a pixel by pixel basis using different criterion for different profiles. For example, the Van Dyk criterion is used for histograms or any of the gradient profiles comparing the patient exposure to the TPS calculated exposure pixel by pixel [16].

Horizontal and vertical profiles are typically used in IMRT QA analysis to detect any spatial discrepancies between the calculated and measured dose distribution. After registering the images, this analysis plots a line profile spatially corresponding to either a horizontal or vertical line in both images (Figure19). For each profile there will be two lines, a solid line and a dashed line. One line corresponds to the film (measured) dose distribution image, and the other line corresponds to the TPS (calculated) dose distribution image. If the images are registered properly and the QA was accurately delivered, the two lines should virtually overlap. Due to small errors in MLC movement, QA set-up, and registration, the lines may not be identical, but should be extremely similar in shape. The horizontal and vertical profile lines can be moved in both images to spatially evaluate different areas of the dose distribution.

Besides horizontal and vertical profiles, the gamma function is one of the most widely used analysis profiles due to its ability to analyze high gradient regions of the dose distribution. The gamma function combines a dose

difference measurement with a distance to agreement (DTA) measurement to assign a numerical value to each pixel in the distribution. A gamma value greater than one indicates a failure of both measurements, and the pixel appears red in color. The dose difference measurement is a user specified tolerance dependent on the calculated dose from the TPS. For example, if the TPS calculated a pixel value to be 10 cGy and the dose difference tolerance was set to +/- 3%, the software would search the measured (film) pixel values until it found a pixel between 9.7 cGy and 10.3 cGy. The DTA measurement is the distance between a measured pixel (film) and the nearest calculated pixel (TPS) that contains the same dose value. For this part of the gamma analysis, the user defines a maximum search area (in mm) where the calculations are to be performed. Adding onto the above example for the dose difference measurement, the software is now constrained to a specific search radius. If the DTA criterion was set to 3mm, the software would look for another pixel that was between 9.7 cGy and 10.3 cGy, and was 3mm or less in distance from the original pixel. At TCSC, we use a 3% dose tolerance and a 3mm distance to agreement as our gamma criteria.

The calculation of gamma throughout the measured dose distribution provides a visual analysis that quantitatively indicates the delivery accuracy relative to the acceptance tolerances, and is displayed as a Gamma Pass/Fail plot. This type of analysis is based on a technique created by Lowe et al of the Mallinckrodt Institute [17-19].

5.2 Rando Phantom Results

A study performed by Thomas et al published in “Medical Physics” recently reported the results of IMRT verifications for ten patients planned and treated with helical Tomotherapy. This study reported that nearly 92% of the film pixels within the analyzed region of interest were within a gamma criterion of 2 mm and 2% [20]. Like most Tomotherapy users, Thomas et al used a test phantom made of homogeneous water equivalent material which could have masked potential errors that arise from limitations in the treatment planning system’s modeling of density corrections. This study evaluated the dosimetric accuracy of a helical tomotherapy system using an anthropomorphic RANDO phantom for patient-specific QA. The results of this study allowed a benchmark to be established for dosimetric accuracy in heterogeneous materials.

A 3mm DTA and 3% dose difference tolerance were used as the gamma analysis criteria for the RANDO phantom study. The results using the RANDO phantom were in stark contrast to those of Thomas *et al*. The mean gamma index value and the percent of pixels exceeding the gamma threshold for the RANDO phantom study are shown in Table I. Upon examination of Table I, it is apparent that the calculated and measured dose distributions for the prostate test cases had a better agreement than the lung cases. On average, the lung patients had 27.2% of the pixels exceeding gamma, and the prostate patients had 14.7% of the pixels exceeding gamma. For the prostate test cases, only two of the films had greater than 20% of the pixels exceed the gamma threshold. In

contrast, sixteen of the lung test cases had pixels that exceeded the gamma threshold.

A close investigation of the calculated versus measured dose distributions for the 24 test patients provides insight into the source of these differences. The gamma pass/fail plots for the lung cases are shown in Figures 20-31, and the prostate cases are shown in Figures 32-43. For the lung cases, the greatest discrepancy between calculated and measured dose occurred at or near a drastic change in tissue density. A discrepancy is defined as a pixel that fails to meet the gamma criteria. Discrepancies appeared at the tumor-low density lung tissue interface as well as the tumor-bone interface. All the lung cases except numbers 4, 8, 9, and 12 had pixels that exceeded that gamma threshold limit of 20%. The sixteen patients who did not meet the 20% gamma threshold limit had tumor volumes that were near one of the above mentioned interfaces. These discrepancy regions were also high-gradient dose regions located near the edge of the tumor volume. This area is known as the penumbra region where the dose rapidly changes as a function of distance from the beam axis.

Despite the prostate calculated and measure dose distributions having better agreement, the same trend identified in the lung cases was apparent in the prostate gamma pass/fail analysis plots. The prostate cases had virtually no discrepancies at the tumor-tissue interface. This is most likely due to the fact that the prostate itself is soft tissue and is surrounded by soft tissue in the pelvis; therefore there is not change in tissue density. The prostate cases had the

greatest discrepancy at or near the tumor-bone interfaces in the pelvis (pubic symphasis and ischial tuberoscities). Further inspection of the prostate cases showed that prostate cases 2, 3, 8, and 11 displayed the greatest discrepancy in the gamma analysis. The pixels that failed the gamma criteria were located mainly at or near the pubic symphasis. The pubic symphasis is commonly referred to as the pubic bone, and is located at the top of the prostate. The horizontal and vertical profiles for all the RANDO test cases are shown in Figures 44-67. The profiles indicate that for the majority of the test cases the dose distributions were spatially correct. Lung cases 3 and 11 and prostate case 3 seemed to have the greatest discrepancy spatially with the vertical profile. All RANDO test case dose distributions were spatially aligned horizontally.

Because the RANDO phantom contains both bone and soft tissue, it is not surprising that the results of the IMRT QA analysis in this study are different from those obtained using homogenous phantoms. At the bone-tissue interface (prostate and pubic symphasis), there is a greater amount of electron backscatter as the beam interacts with the bone causing a slight dose enhancement in the tissue adjacent to the bone, which is limited to a few millimeters [4, 21-27]. On the transmission side of the tissue-bone interface, there is a slight forward scatter of electrons from the bone. This forward scatter can cause a build-up of electrons in the soft tissue giving rise to a dose perturbation. In contrast to published results, it is a possibility that the backscatter effect could be causing the gamma deficiencies due to the fact that previous tests only simulated

heterogeneous phantoms and were not true RANDO phantoms. Previous reports used make-shift phantoms of balsa wood and different density materials to simulate a heterogeneous phantom. Unlike the RANDO phantom, these phantoms did not have real human skeleton, lung cavities, or water equivalent material to represent human soft tissue. At low energies like that of Tomotherapy, The American Association of Physicists in Medicine Task Group 65 reported that these dose enhancements should not cause great change in the dose distribution [21].

Many reports have revealed that incorrect doses can be computed within or near a low-density medium such as the lung, particularly when the field size is small [28-32]. In the lung where there is a tumor-low density lung tissue interface, Kornelson and Young state that there is a loss of lateral electronic equilibrium when a high energy photon beam traverses the lung due to the face that an increasing number of electrons travel outside the geometrical limits of the beam. This causes a loss of dose on the beam axis and results in a less sharp dose distribution profile. Kornelson and Young state this is only for small field sizes ($<6x6cm^2$) and for energies above 6MV [33]. Epps et al suggests that a decrease in dose occurs at the surface beyond the cavity for large cavities such as the lung and small field sizes [34, 35]. Both of these reports used homogeneous phantoms and did not take into account contributions from tissue-bone interfaces. Since the RANDO phantom QA plans were designed so that the tumor resided inside the phantom in the same anatomical site as in the

patient, some tumors were located at or near a tissue-bone interface. Taking into account the electron scatter effect at the tumor edge and possible backscatter effects from tissue-bone interfaces, introduces a possible cause as to why lung cases 1, 2, 5, 6, and 11 failed to meet the gamma criteria.

While it is clear that the heterogeneities have an effect on the measured dose distributions, it is unclear if these errors are due to film response at the tissue-bone interfaces or from actual dose calculation errors [21-38]. In order to rule out set-up error as a cause of the above mentioned discrepancies, the reproducibility of the film dosimetry was tested for two prostate and two lung cases. Repeat measurements were taken on three separate occasions, and the films were processed on separate days from one another (Figure 68). The standard deviation for the number of pixels exceeding the gamma threshold was 3.9%. For the prostate cases, the spatial location of the dose errors was not consistent between measurements as shown in repeat measurement two. In contrast, the spatial location of the maximum error for the lung cases was consistent from measurement to measurement. Because the prostate measurements were not consistent, set-up errors could not be ruled out as a possible cause of the discrepancies.

5.3 MatriXX Detector Results

The primary objective of this portion of the study was to determine if the MatriXX detector could be used as a substitute for radiographic film in rotational

IMRT delivery techniques, such as Tomotherapy. In order to be useful for these delivery techniques, the device must be angular independent in dose-response and be capable of measuring composite dose distributions created during rotation. A total of twenty helical tomotherapy test cases have been measured and evaluated (12 prostates, 3 head & neck, 2 paraspinal metastasis, 1 brain tumor, 1 esophageal tumor, and 1 mesothelioma). This group of patients represented a broad spectrum of patients treated with rotational modulated delivery.

After analyzing and comparing the gamma pass/fail plots for EDR2 film and the MatriXX detector, it was shown that the EDR2 film had a much better agreement between calculated and measured dose distributions than the MatriXX data (Figures 69-88). From the gamma analysis, the percent of pixels exceeding the threshold with a 3% dose difference tolerance and 3-mm DTA criteria was 10.8 ± 6.7% for the EDR film verses 23.4 ± 13.8% for the MatriXX as shown in Table II. For the EDR film, test case 14 was the only case to have more than 20% of the pixels exceed the gamma threshold. In contrast, half of the MatriXX test cases exceeded the gamma threshold by more than 20%. While some test cases had large discrepancies between calculated and measured dose distributions in both the film and the MatriXX data (Patients 2, 11, and 14), the patient with the worst agreement using the MatriXX (Patient 8) appeared normal in the film analysis.

Further investigating the tumor volume size and the MatriXX specifications, it was determined that the MatriXX appears to function well in high-dose low-gradient regions and low-dose low-gradient regions. The gamma pass/fail plots confirmed the MatriXX has difficulty in regions with steep dose gradients, such as the penumbra region at the edge of the tumor volume. This is likely due to a combination of two issues. The first issue is the fact that the MatriXX performs volume averaging across the 4.5 x 5 mm^2 chambers. The size of the ion chambers used in the MatriXX seem small, but are actually quite large in reference to tumor size and high-gradient regions. Because of this, errors seem to be intensified. The second issue is the coarse 7.62 mm center-to-center spacing of the chambers. In rotational IMRT delivery, the dose gradients are frequently 5-10% per mm. Given the geometry and spacing of the individual detectors, the dose can easily be out of tolerance in the gamma calculations [39, 40]. In this study, the MatriXX was set to interpolate the measured doses to a 3 mm resolution during data acquisition. Even with the interpolation between the measured data points, it was very difficult to meet the 3-mm spatial DTA criteria for the gamma pass/fail plots.

CHAPTER VI

Conclusion

6.1 RANDO Phantom

The RANDO phantom study evaluated the dosimetric accuracy of a helical tomotherapy system using an anthropomorphic RANDO phantom for patient-specific QA. The results of this study allowed a benchmark to be established for dosimetric accuracy in heterogeneous materials. Using a 3mm DTA and 3% dose difference tolerance, 12 prostate and 12 lung test cases were analyzed. The results using the RANDO phantom were in stark contrast to those of homogeneous phantom studies, especially for the lung test cases. While it is clear that the heterogeneities of the RANDO phantom have an effect on the measured dose distributions, it is unclear if these errors are due to film response at the tissue-bone interfaces or from actual dose calculation errors. As shown from the repeat measurements, set-up error can not be ruled out as a possible contributor to the analysis discrepancies. The size, weight, and inefficient set-up do not make the RANDO phantom a good modality for IMRT QA at the present time. More investigation is needed before this becomes a routine modality for IMRT QA.

6.2 Matrixx Detector

The primary objective of the MatriXX study was to determine if the MatriXX detector could be used as a substitute for radiographic film in rotational IMRT delivery techniques, such as Tomotherapy. A total of twenty helical tomotherapy test cases were analyzed using a 3mm DTA and 3% dose difference tolerance. The results showed that the MatriXX appears to function well in high-dose low-gradient regions and low-dose low-gradient regions. The gamma pass/fail plots confirmed the MatriXX has difficulty in regions with steep dose gradients due to volume averaging and the coarse 7.62 mm center-to-center spacing of the chambers. Because of this, the dose can be out of tolerance considering the dose gradients are frequently 5-10% per mm for rotational IMRT. Based on the analysis of the MatriXX data, half of the patients in this study would not have passed our institution's patient-specific IMRT QA testing. In contrast, only one patient would not have passed for measurements taken with film. The MatriXX is limited in its spatial resolution and has difficulty adequately verifying plans with steep dose gradients. At this time, the MatriXX may not be the best modality for rotational IMRT delivery techniques. Further investigation is needed.

LIST OF REFERENCES

1. www.aapm.org/medical_physicist/default.asp

2. Hall, Eric J. Radiobiology for the Radiologist. Lippincott Williams & Wilkins, 6th edition (2006).

3. Karzmark, C.J.; Morton, R. A Primer on Theory and Operation of Linear Accelerators in Radiation Therapy. Medical Physics Publishing, 2nd edition (1998).

4. Khan, Faiz M. The Physics of Radiation Therapy. Lippincott Williams & Wilkins, 3rd edition (2003).

5. Varian Medical Systems, Inc 1999-2009. ClinacTreatment Delivery Overview. Retrieved November 7, 2008 from http://www.varian.com/us/oncology/radiation_oncology/clinac

6. Holmes, T.; Mackie, T. TOMOTHERAPY. The Wiley Encyclopedia of Medical Devices and Instrumentation. Second Edition (April 2006).

7. Tomotherapy Incorporated, 2008. Precision. Retrieved February 25, 2008 from http://www.tomotherapy.com/index.php/difference/precision

8. Low, D. Quality Assurance of Intensity-Modulated Raiotherapy. Seminars in Radiation Oncology, July 2002; 12 (3), pp 219-228.

9. Yu, C.; Chen, D.; Li, A.; Ma, L.; Shapard, D.; Sarfaraz, M.; Holmes, T. Clinical Implementation of Intensity-Modulated Arc Therapy. Engineering in Medicine and Biology Society, 2000. Proceedings of the 22nd Annual International Conference of the IEEE, July 2000; (4), pp 3035 – 3037.

10. Otto, K. Volumetric modulated arc therapy: IMRT in a single gantry arc. Medical Physics, January 2008; 35 (1), pp 310-317.

11. Wang, C.; Luan, S.; Tang, G.; Chen, D.; Earl, M.; Yu, C. Arc-modulated radiation therapy (AMRT): a single arc form of intensity-modulated arc therapy. Phys. Med. Biol. 2008; (53), pp 6291-6303.

12. Harold, J., Cunningham, J. The Physics of Radiology. Thomas Books, 4th edition (1983).

13. Almond, P.; Coursey, B.M.; Hanson, W.F.; Saiful Huq, M.; Nath, R.; Rogers, D.W.O. AAPM's TG-51 protocol for clinical reference dosimetry of high-energy photon and electron beams. Medical Physics, September 1999; 26 (9), pp 1847-1870.

14. The MatriXX user manual

15. The Phantom Laboratory. RANDO Phantom. Retrieved February 25, 2008 from www.phantomlab.com

16. Van Dyk, J., Barnett, R., Cygler, J, and Shragge, P., "Commissioning and Quality Assurance of Treatment Planning Computers," Int. Journal Radiation Oncology, Biol. Phys., (26), pp 261-273.

17. Low, D., Harms, Mutic, Purcy, "A Technique for the quantitative evaluation of dose distributions," Medical Physics, May 1998; (25), pp 656-661.

18. Low, Dempsey, Mutic, “Evaluation of the gamma dose distribution comparison method”, Medical Physics, September 2003; 30(9), pp 2455-2464.

19. Radiological Imaging Technology, 2009. IMRT, IGRT, & VMAT Analysis. Retrieved January 10, 2009 from http://www.radimage.com/imrt_igrt/imrtigrtanalysis.php

20. Thomas, S.D.; Mackenzie, M.; Field, G.C.; Syme, A.M.; Fallone, B.G.; Patient specific treatment verifications for helical tomotherapy treatment plans. Medical Physics, December 2005; 32 (12), pp 3793-3800.

21. Papanikolaou, N. Tissue Inhomogeneity Corrections for Megavoltage Photon Beams. American Association of Physicists in Medicine Radiation Therapy Committee Task Group 65, Medical Physics Publishing, 2004.

22. Spiers, W. The influence of energy absorption and electron range on dosage in irradiated bone. Br. J. Radiol. 1949; (22) pp 521-533.

23. Spiers, W. Dosage in irradiated soft tissue and bone. Br. J. Radiol. 1951; (25) pp 365-370.

24. Sinclair, W.K.. The relative biological effectiveness of 22-MV x-rays, cobolt-60 gamma rays, and 200-kVp x-rays. Absorbed dose to the bone marrow in the rat and the mouse. Radiat. Res. 1962; (16) pp 369-383.

25. Aspin, N; Johns, H.E. The absorbed dose in cylindrical cavities within irradiated bone. Br. J. Radiol. 1963; 36 (425) pp 350-362.

26. Das, I.J. Study of Dose Perturbation at Bone-Tissue Interfaces in Megavoltage Photon Beam Therapy. Ph.D. Thesis, University of Minnesota, 1988.

27. Reft, C.S.; Kuchnir, F.T. Dose Correction Factors at Bone-Tissue Surface for High Energy Photon Beams. Presented at annual AAPM meeting 1986.

28. Engelsman, M; Damen, E.; Kiken, P.W.; Mijnheer, B.J. Impact of simple tissue inhomogeneity correction algorithms on conformal radiotherapy of lung tumours. Radiother. Oncol. 2001; (60) pp 299-309.

29. Mackie, T.; El-Khatib, E.; Battista, J.; Scrimger, J.; Van Dyk, J.; Cunningham, J.R. Lung dose correction for 6 MV and 15 MV x-rays. Medical Physics 1985; (12) pp 327-332.

30. O'Connor, J; Malone, D. An equivalent shape approximation for phrton doses in lung Phys. Med. Biol 1990; 35 (2) pp 223-234.

31. Metcalfe, P.; Wong, T.; Hoban, P. Radiotherapy x-ray beam inhomogeneity corrections: the problem of lateral electronic disequilibrium in lung. Australas. Phys. Eng. Sci. Med. 1993; (16) pp 155-167.

32. Mayer, R.; Williams, A.; Frankel, T.; Cong, Y.; Simons, S.; Yang, N.; Timmerman, R. Two-dimensional film dosimetry application in heterogeneous materials exposed to megavoltage photon beams. Medical Physics 1997; (24) pp 455-460.

33. Kornelson, R.O.; Young, M.J.; Changes in the dose-profile of a 10MV x-ray beam within and beyond low density material. Medical Physics 1982; 9:114.

34. Epp, E.; Boyer, A.; Doppke, K.; Underdosing of lesions resulting from lack of electronic equilibrium in upper respiratory air cavities irradiated by a 10MV x-ray beam. International Journal of Radiation Oncology Biol. Phys 1977; 2:613.

35. Epp, E.; Lougheed, M.; McKay, J. Ionization buildup in upper respiratory air passages during tletherapy units with cobalt 60 radiation. British Journal of Radiology 1958; 31:361.

36. Chaudhari, S.; Goddu, S.; Mutic, S.; Esthappan, J.; Kawamura, S.; Low, D. Dosimetric Validation of Tomotherapy in Heterogeneous Media. Medical Physics, June 2006; 33 (6), pp 2093-2093.

37. Yan, Y.; Papanikolaou, N.; Weng, X.; Penagaricano, J.; Ratanatharathorn, V.; Fast radiographic film calibration procedure for

helical tomotherapy intensity modulated radiation therapy dose verification. Medical Physics, 2005; (32), pp 1566-1570.

38. Davidson, S.; Ibbott, G.; Prado, K.; Dong, L.; Liao, Z.; Followill, D. Accuracy of two heterogeneity dose calculation algorithms for IMRT in treatment plans designed using an anthropomorphic thorax phantom. Medical Physics, May 2007; 34 (5), pp 1850-1857.

39. S.Amerio, et al, Dosimetric characterization of a large area pixel-segmented ionization chamber. Medical Physics, 2004; 31(2) pp 414-420.

40. E Spezi, et al, Characterization of a 2D ion chamber array for the verification of radiotherapy treatments. Phys. Med. Biol., 2004; (50) pp 3361-3373.

APPENDIX I - Figures

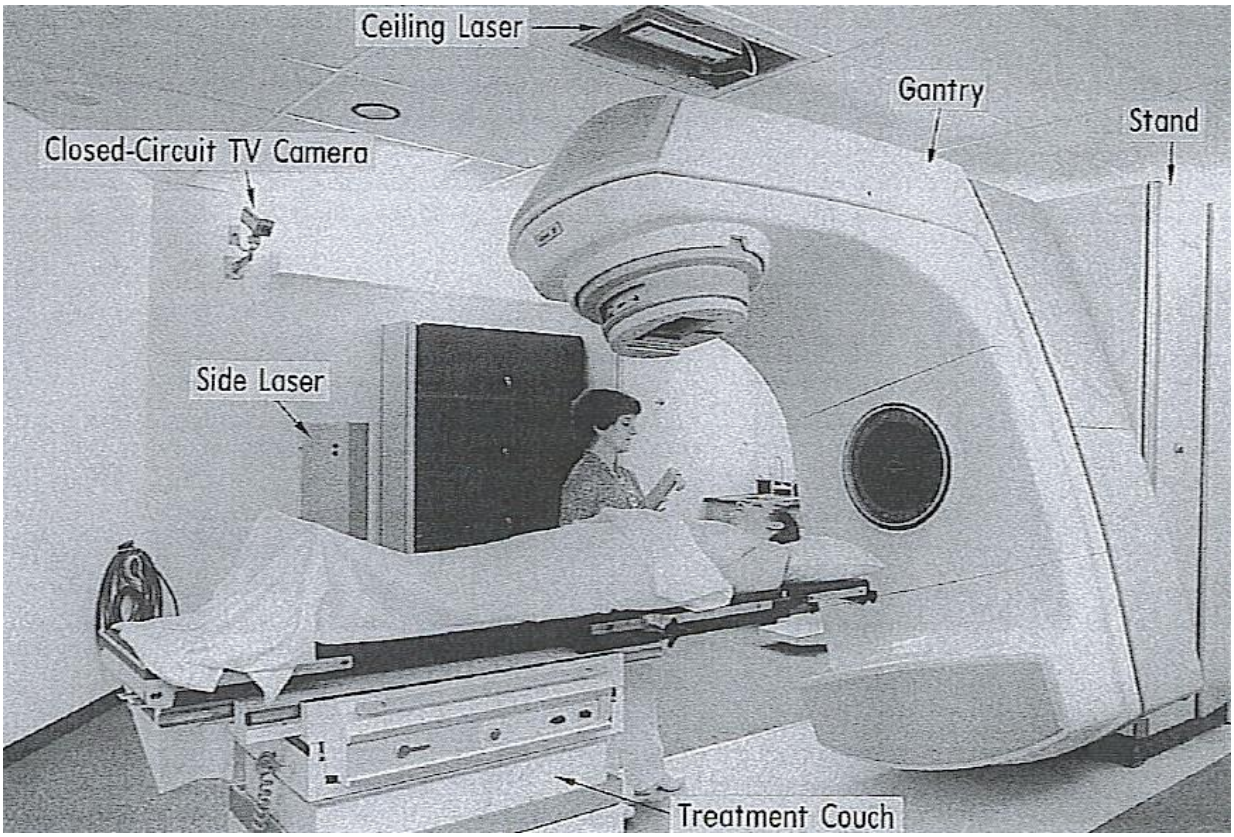

Figure 1: The external components of a traditional clinical linear accelerator and treatment room [3].

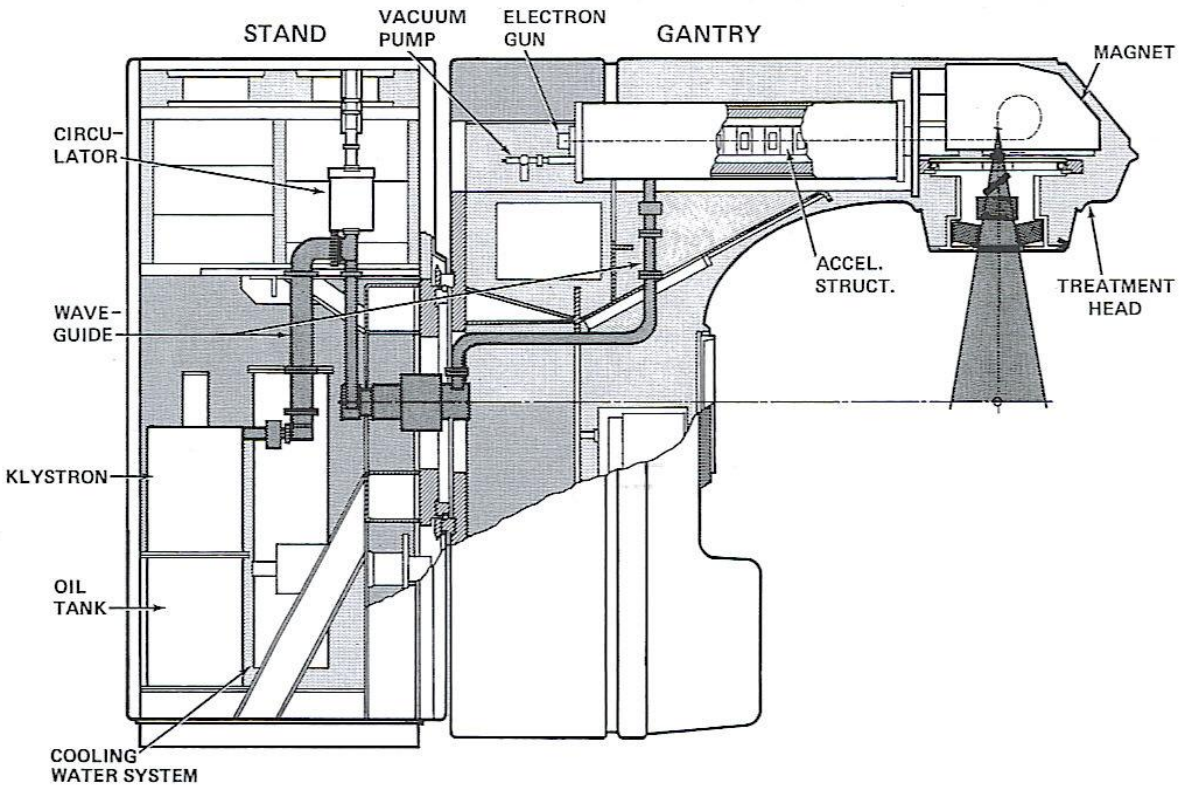

Figure 2: The internal components of a traditional linear accelerator [3].

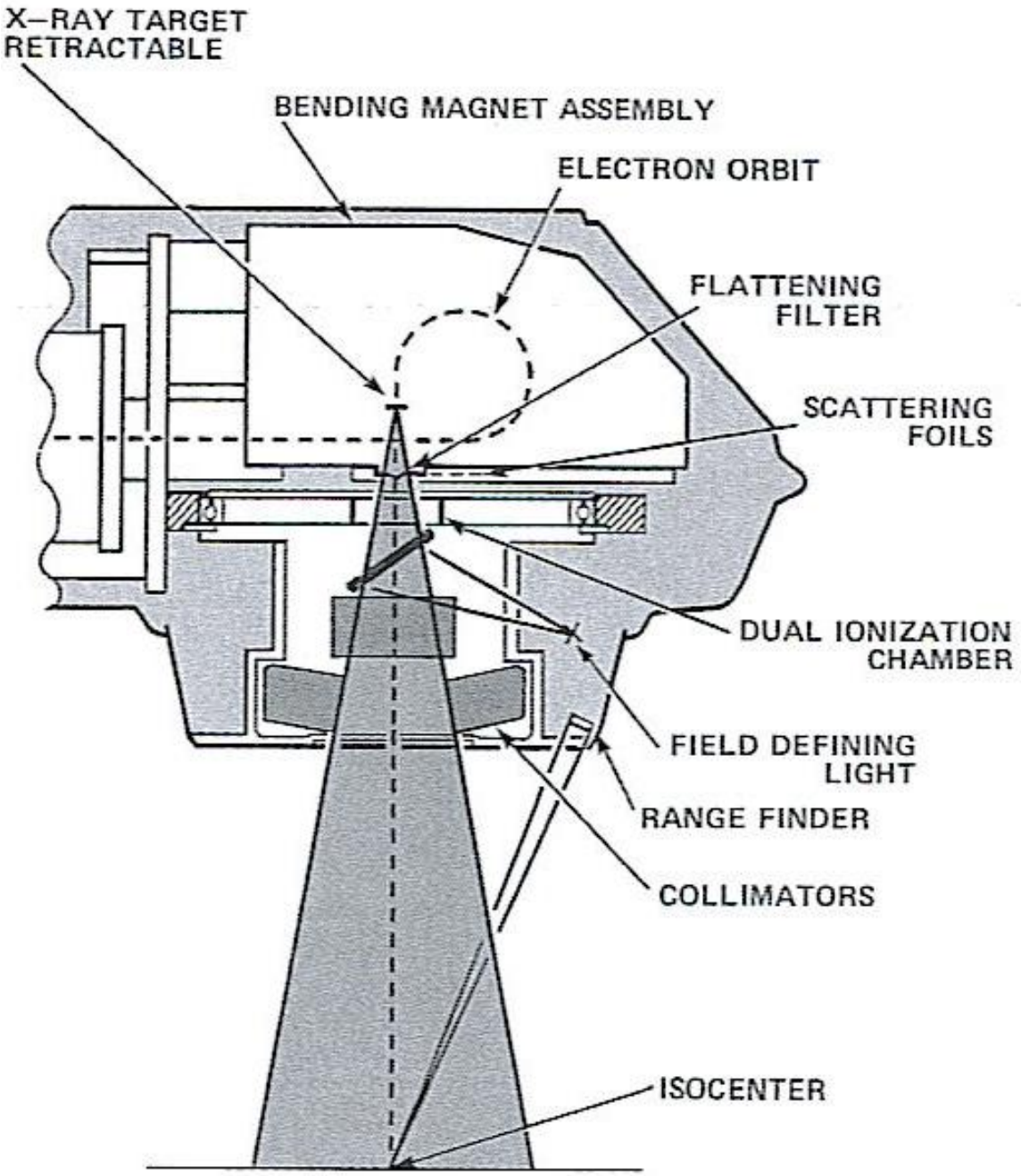

Figure 3: Gantry head components [3].

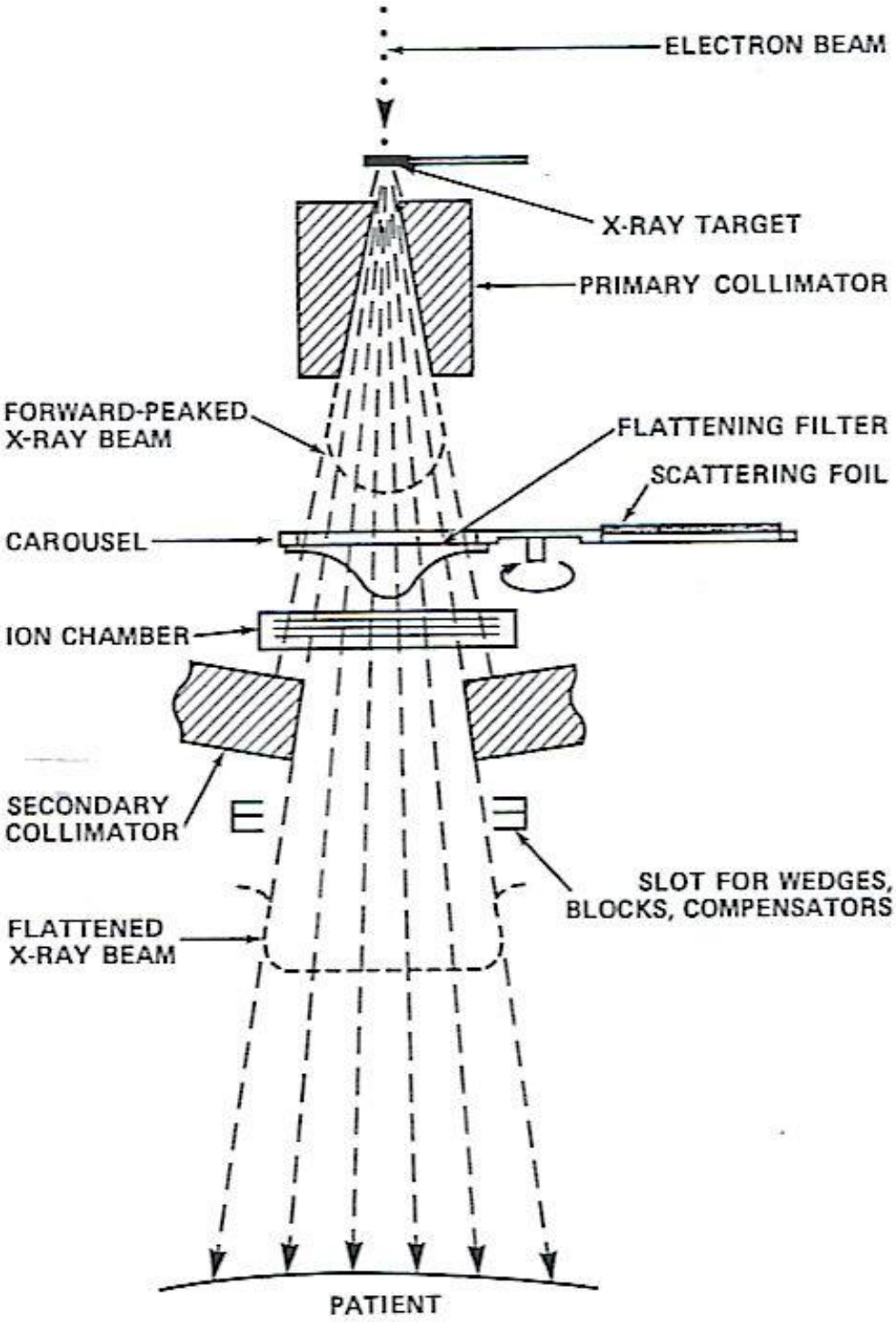

Figure 4: Gantry head components below the bending magnet for a photon beam [3].

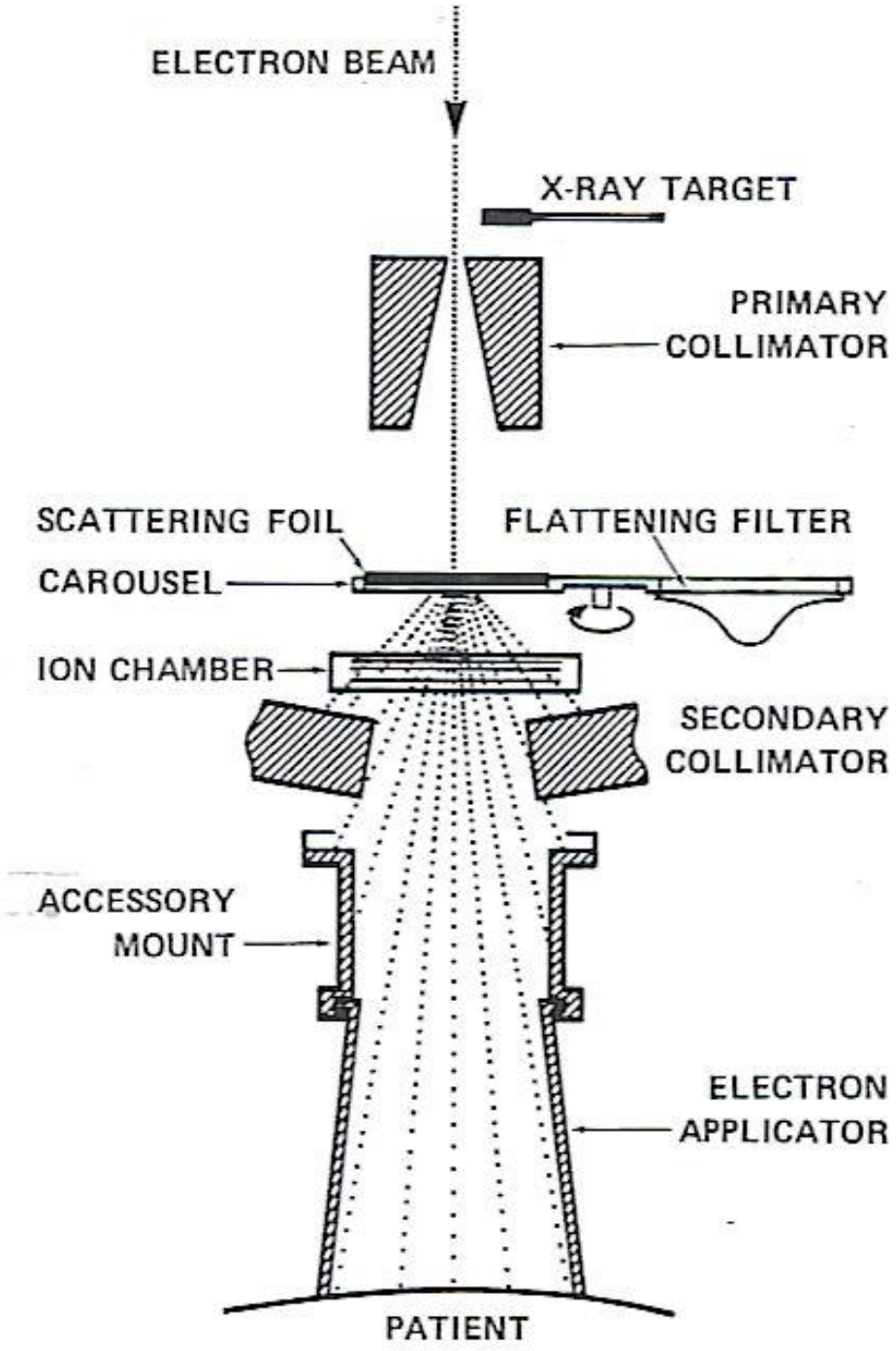

Figure 5: Gantry head components below the bending magnet for an electron beam [3].

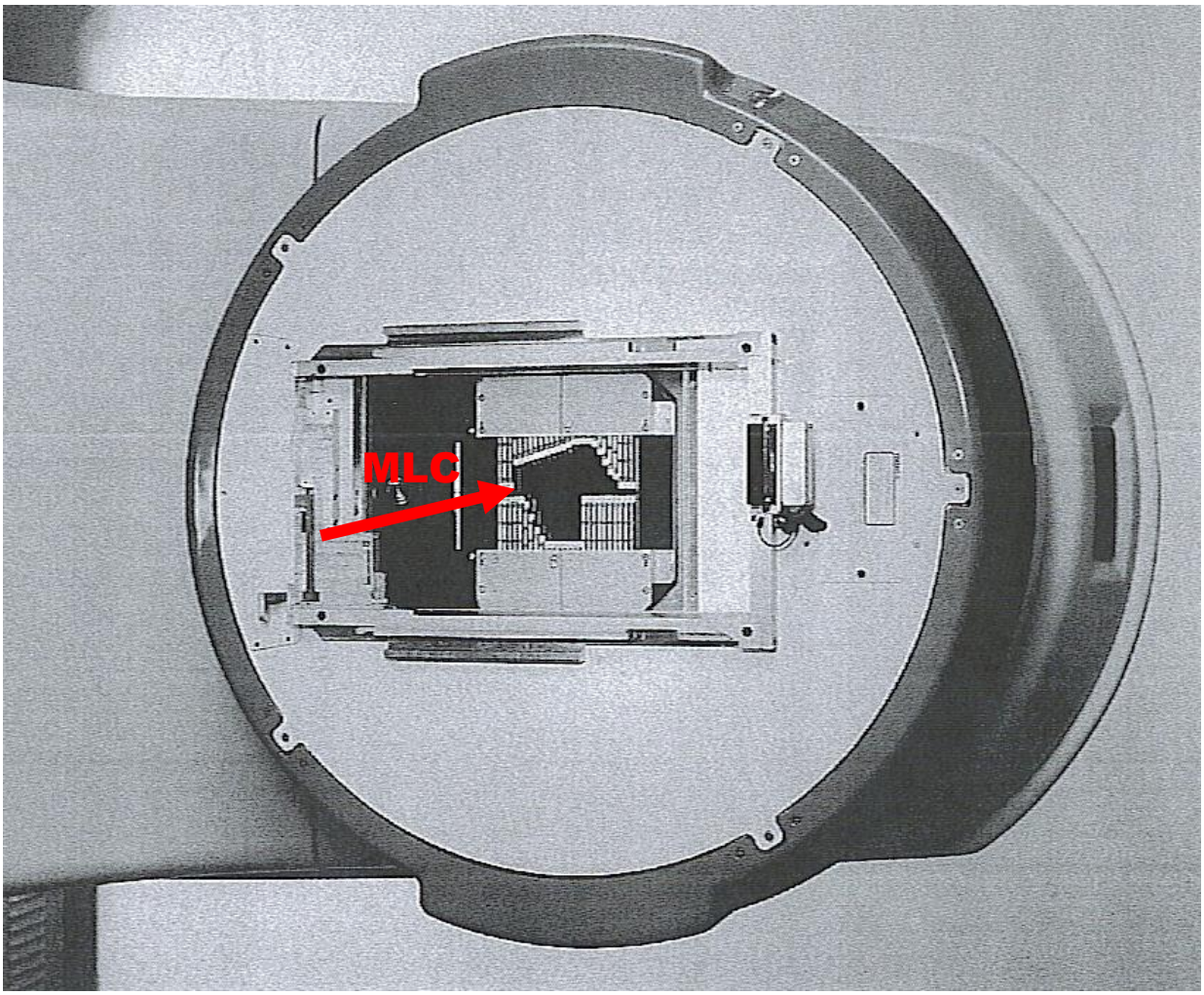

Figure 6: MLC seen through the bottom of the collimator [4].

Figure 7: The Tomotherapy linac at Thompson Cancer Survival Center.

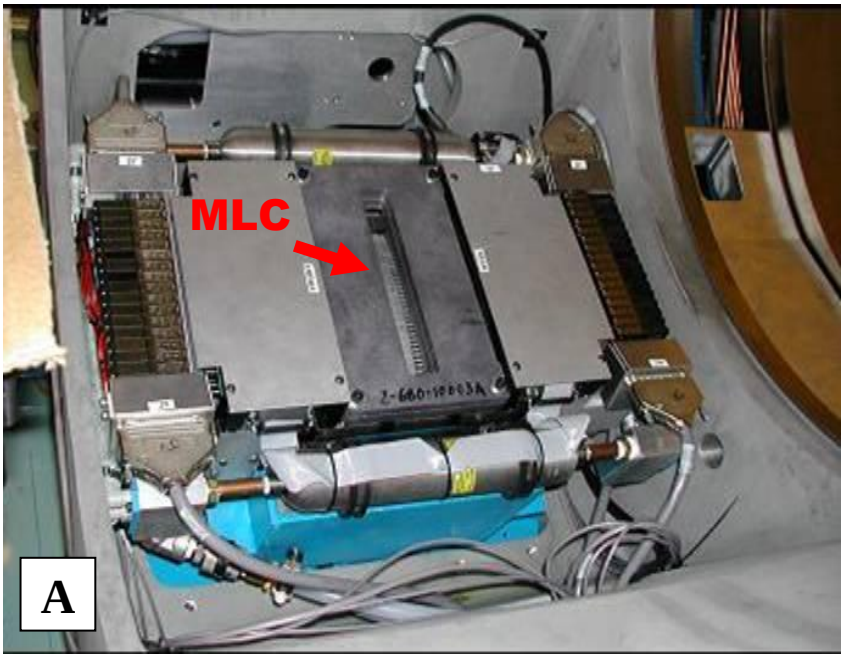

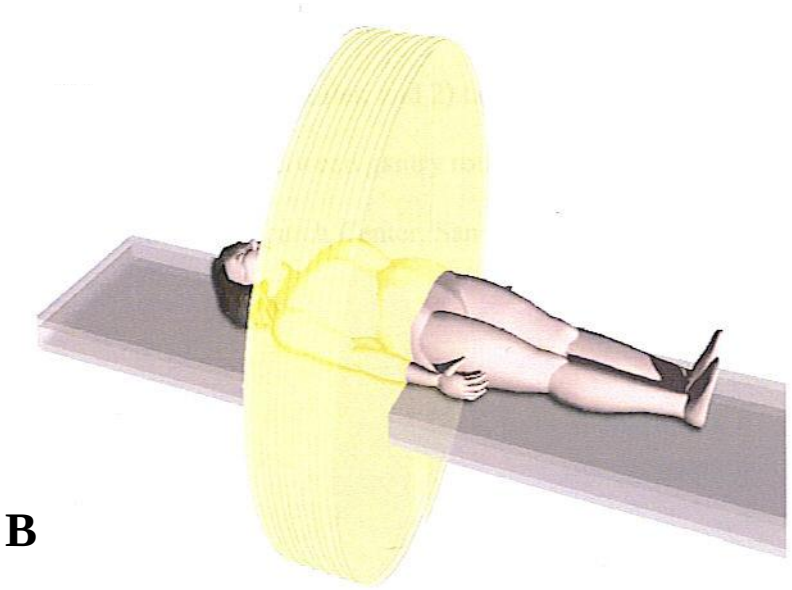

Figure 8: Tomotherapy's binary MLC is shown in picture A. Picture B shows the resultant delivery dose pattern around a patient as Tomotherapy's binary multi-leaf collimator rotates simultaneously with the couch's linear motion into the gantry bore.

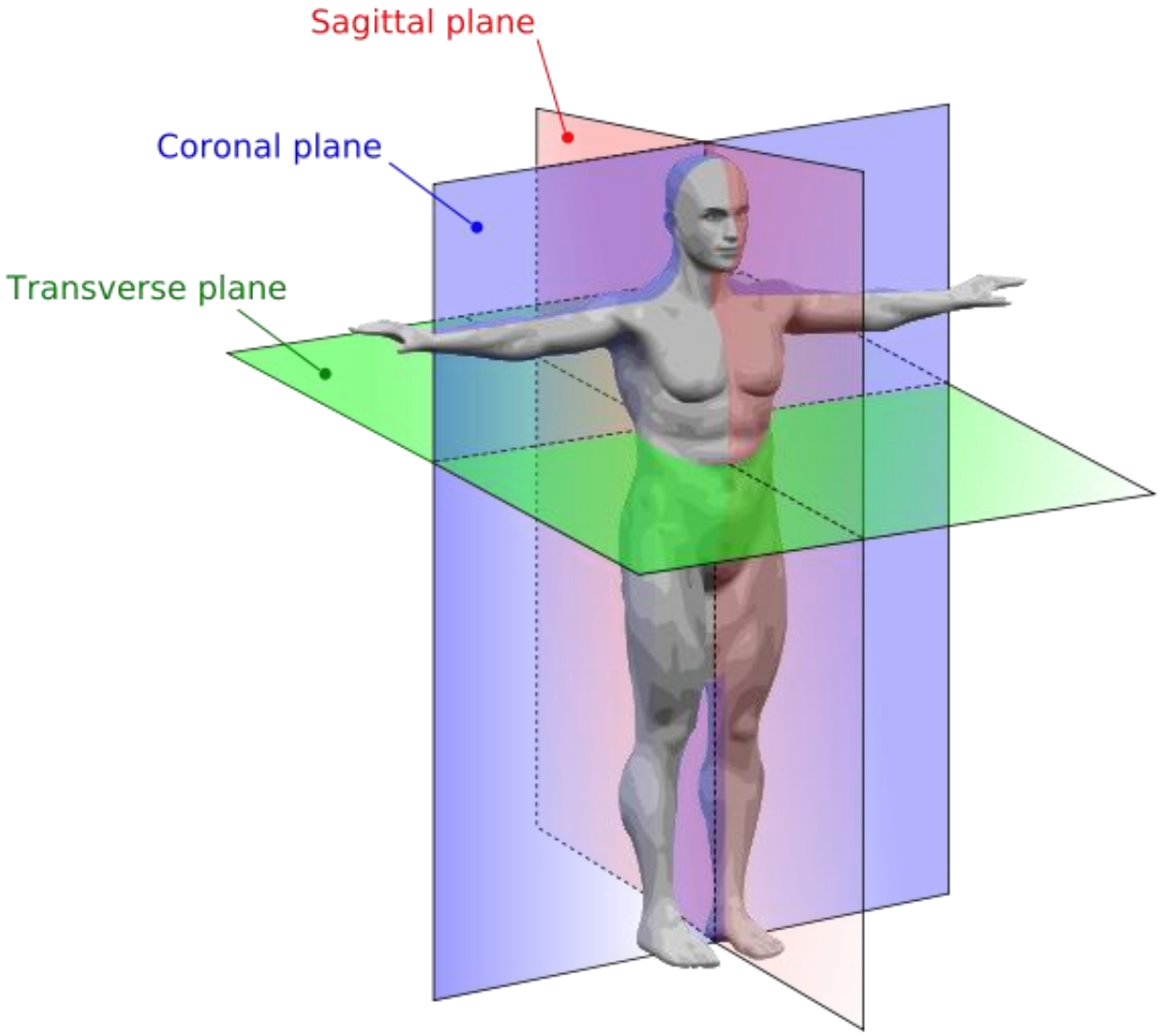

Figure 9: When quality assurance is performed in radiation therapy and film is used as the dosimeter, a coronal, sagittal, or transverse plane is chosen for the film placement.

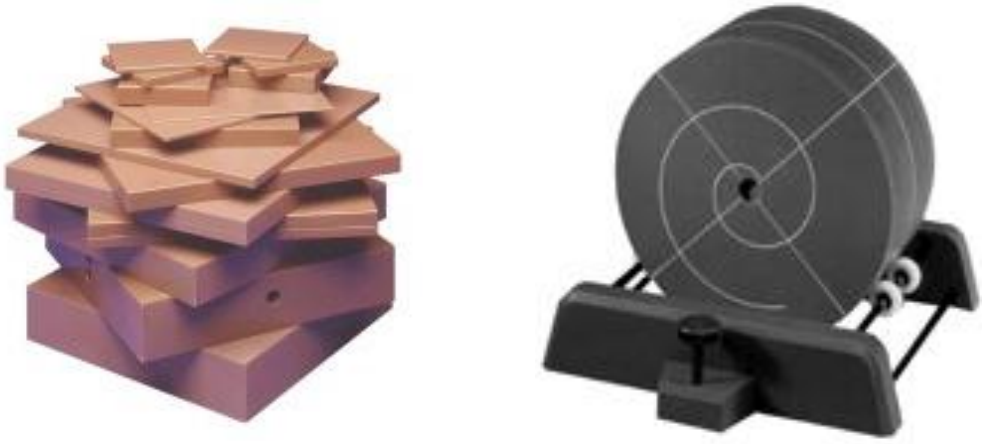

Figure 10: Solid water phantoms used in quality assurance tests, solid water slabs, and a cylindrical phantom

Figure 11: A thimble ionization chamber commonly used in radiation therapy quality assurance testing.

Figure 12: The MatriXX detector from IBA Dosimetry used for IMRT quality assurance in radiation therapy [14].

Figure 13: The male Alderson RANDO phantom representing a 5'9", 163 lb human male separated transversely into 2.5-cm slices [15].

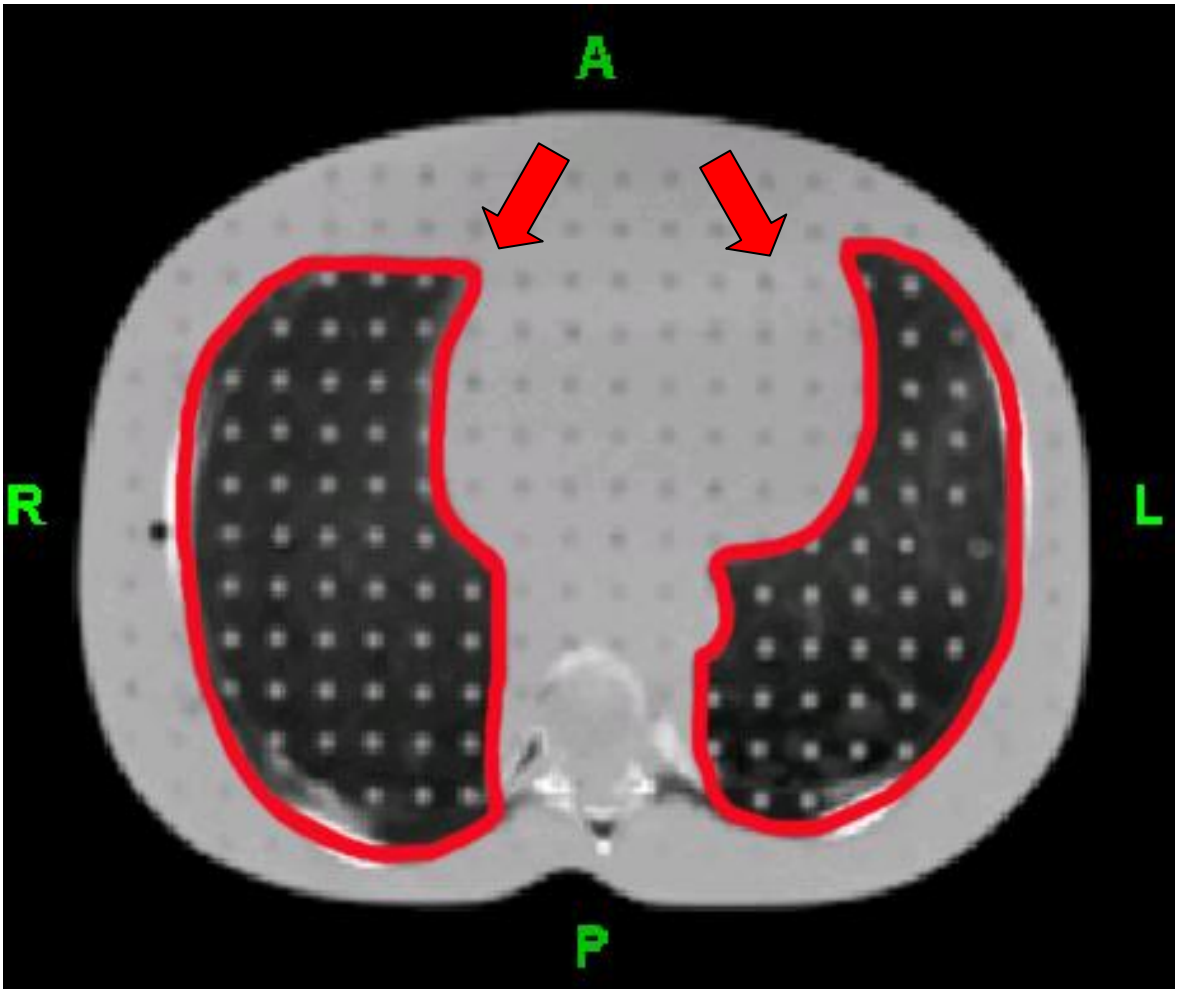

Figure 14: A 2.5 cm slice of the lung portion of the RANDO phantom. The lung portion is made with a lower density material simulating human lungs in a median respiratory state

Figure 15: The Pelvic and Lung phantoms used in the RANDO phantom study. The pelvic section consisted of slices 26-35, and the lung section consisted of slices 14-19.

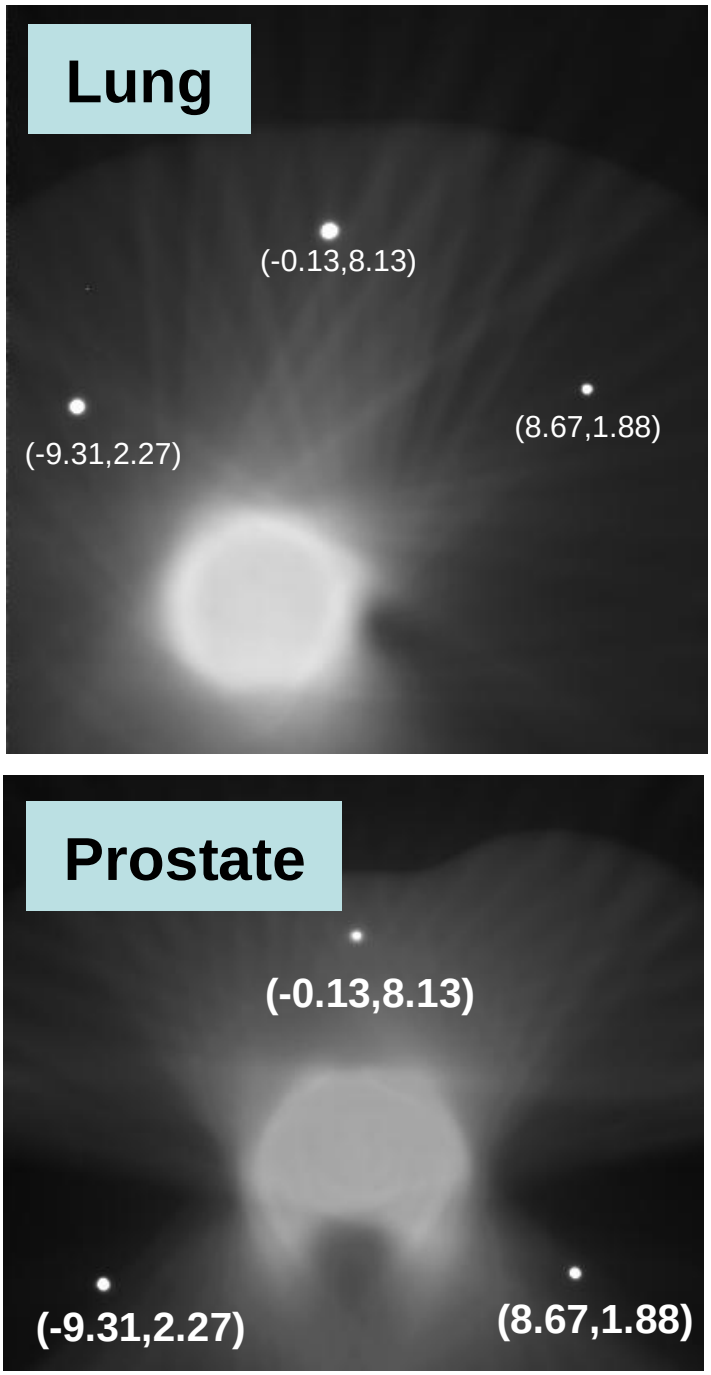

Figure 16: Film fiducial marks made prior to irradiation relative to the linac's isocenter.

Figure 17: The Vidar 16 Dosimetry Pro at the Thompson Cancer Survival Center used to scan the processed films.

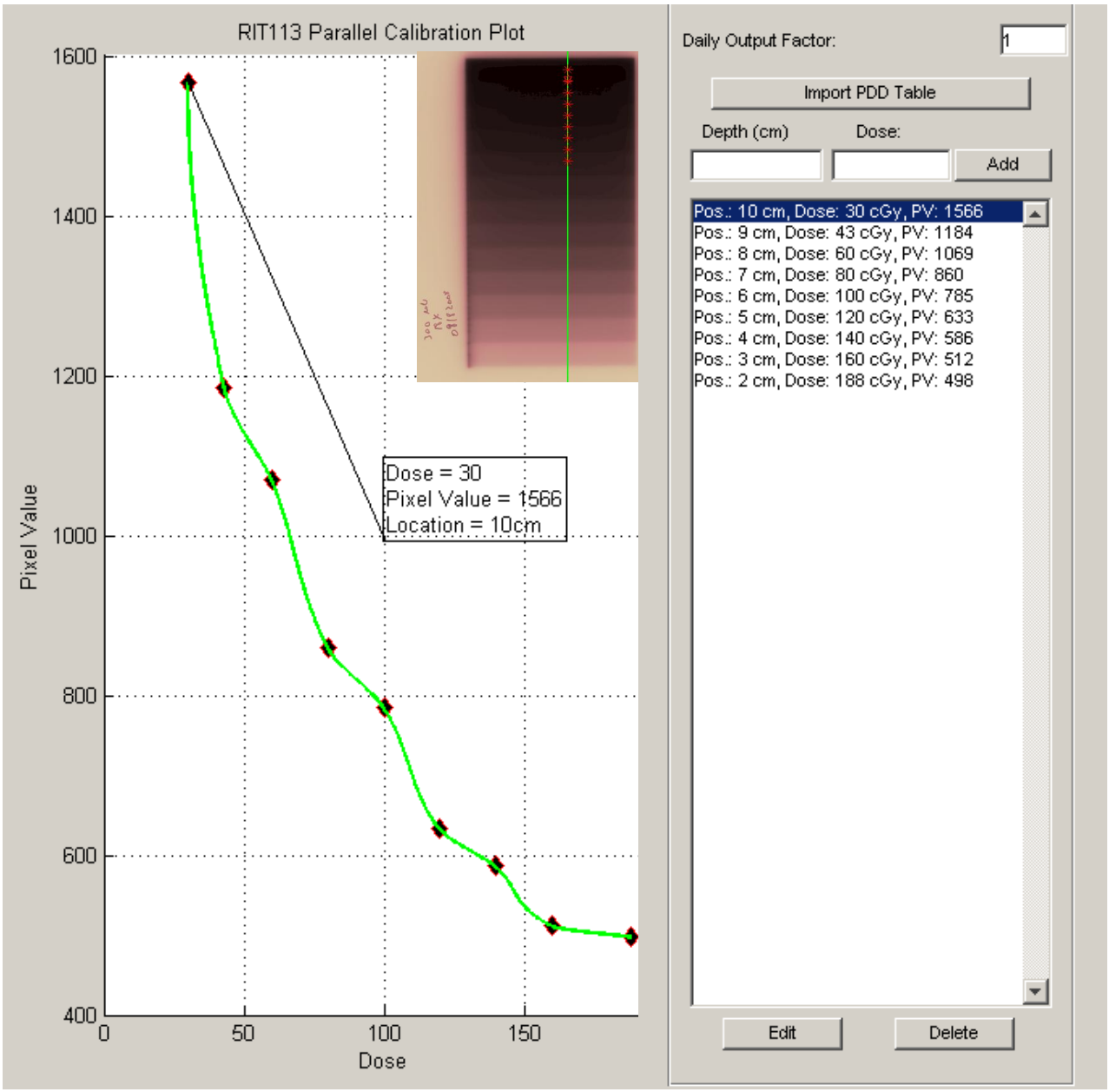

Figure 18: Calibration curve created from 13-segment irradiated film

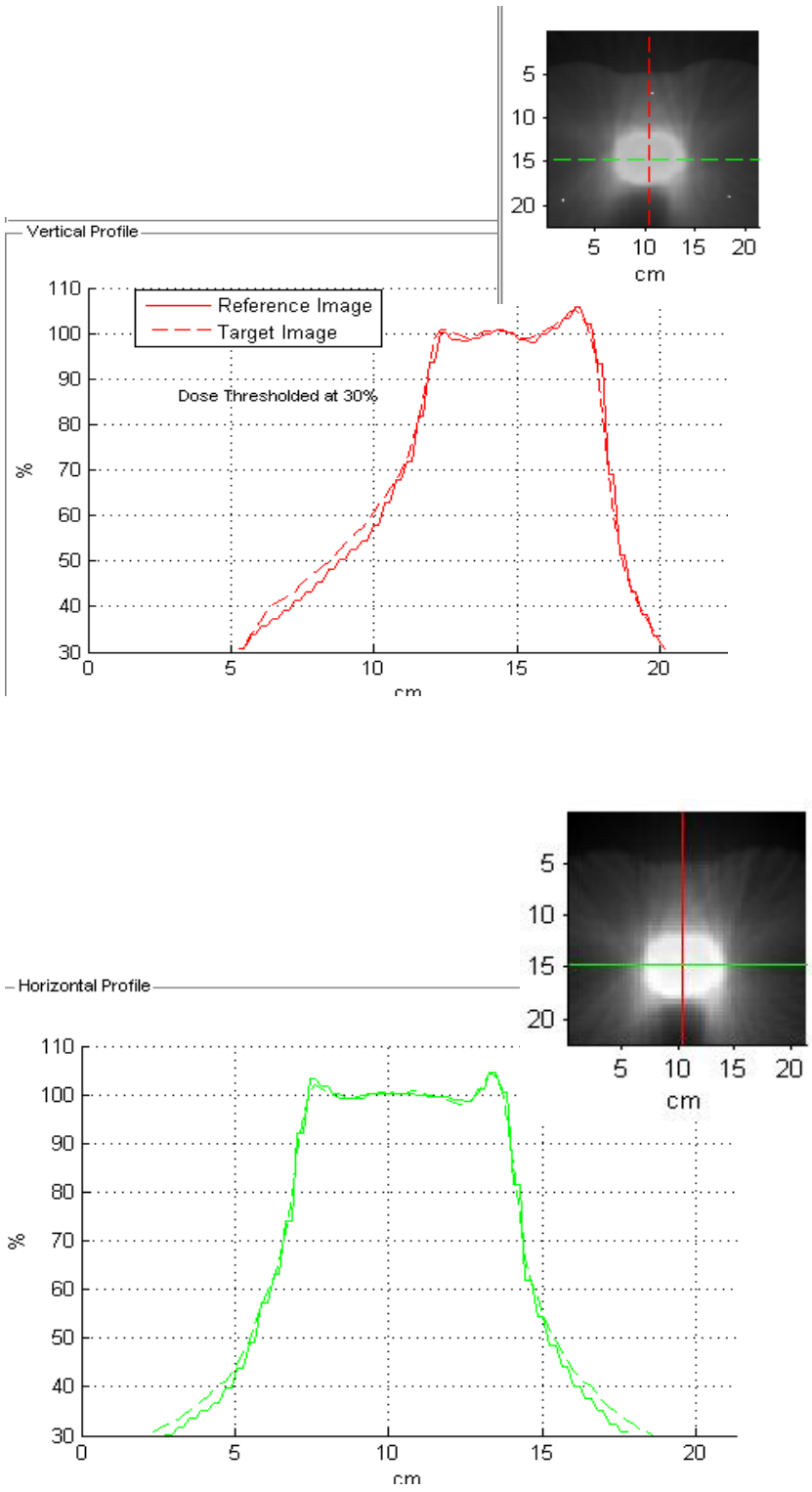

Figure 19: Vertical and Horizontal profiles used to spatially compare the calculated and measure dose distributions. If dose distributions are in complete agreement, solid line and dashed line will be superimposed.

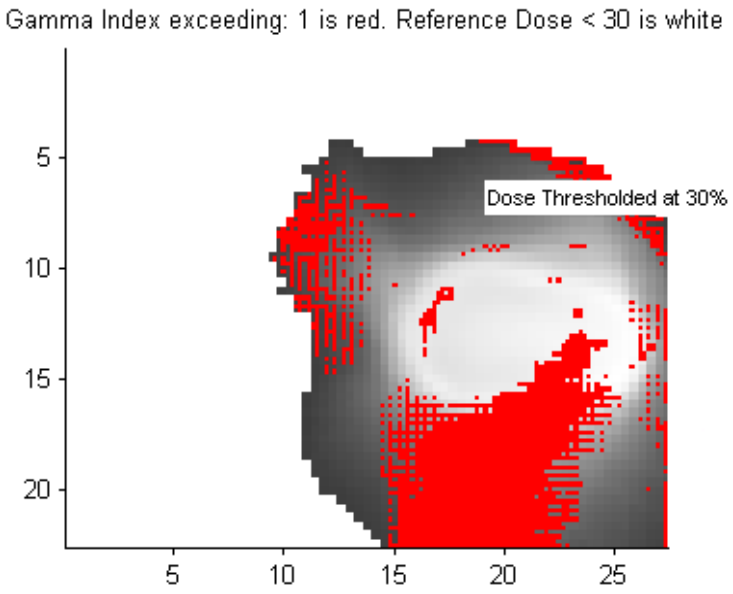

Figure 20: Gamma Pass/Fail diagram for RANDO Lung patient 1 using a 3mm DTA and 3% dose difference tolerance. The analysis region was defined as the area of film receiving over 30% of the prescribed dose.

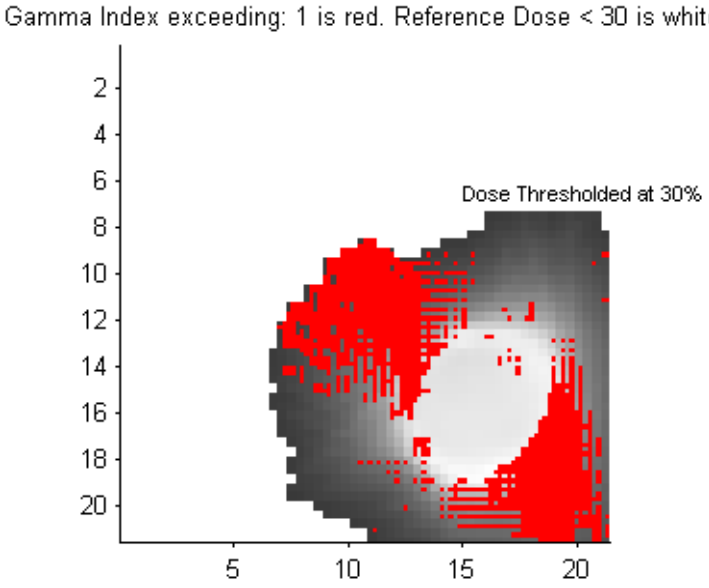

Figure 21: Gamma Pass/Fail diagram for RANDO Lung patient 2 using a 3mm DTA and 3% dose difference tolerance. The analysis region was defined as the area of film receiving over 30% of the prescribed dose.

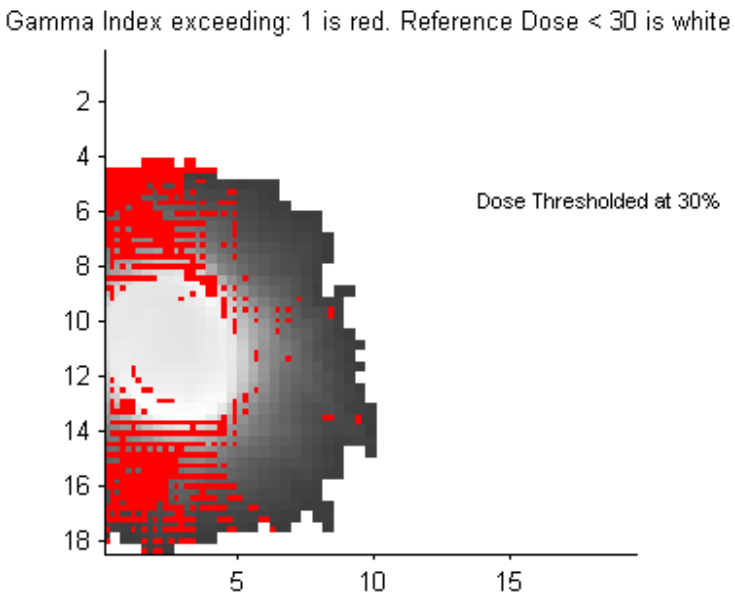

Figure 22: Gamma Pass/Fail diagram for RANDO Lung patient 3 using a 3mm DTA and 3% dose difference tolerance. The analysis region was defined as the area of film receiving over 30% of the prescribed dose.

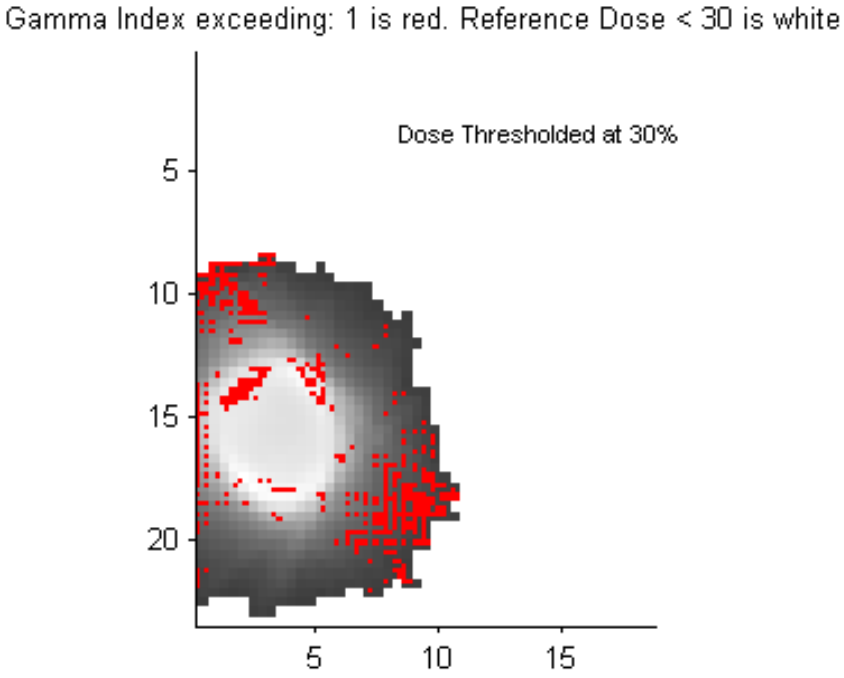

Figure 23: Gamma Pass/Fail diagram for RANDO Lung patient 4 using a 3mm DTA and 3% dose difference tolerance. The analysis region was defined as the area of film receiving over 30% of the prescribed dose.

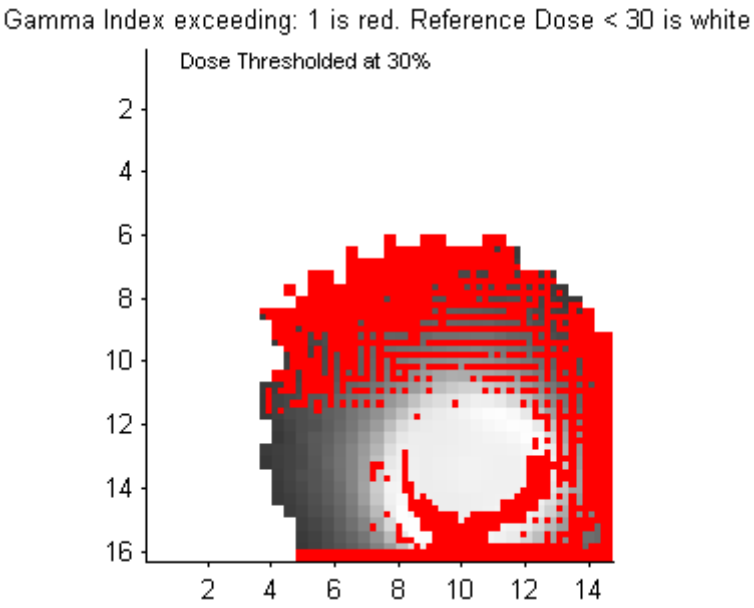

Figure 24: Gamma Pass/Fail diagram for RANDO Lung patient 5 using a 3mm DTA and 3% dose difference tolerance. The analysis region was defined as the area of film receiving over 30% of the prescribed dose.

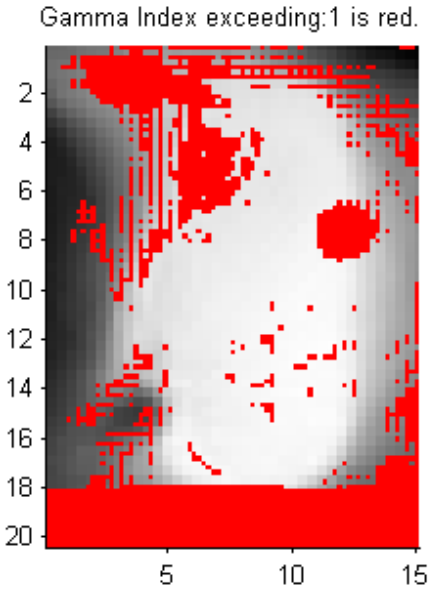

Figure 25: Gamma Pass/Fail diagram for RANDO Lung patient 6 using a 3mm DTA and 3% dose difference tolerance. The analysis region was defined as the area of film receiving over 30% of the prescribed dose.

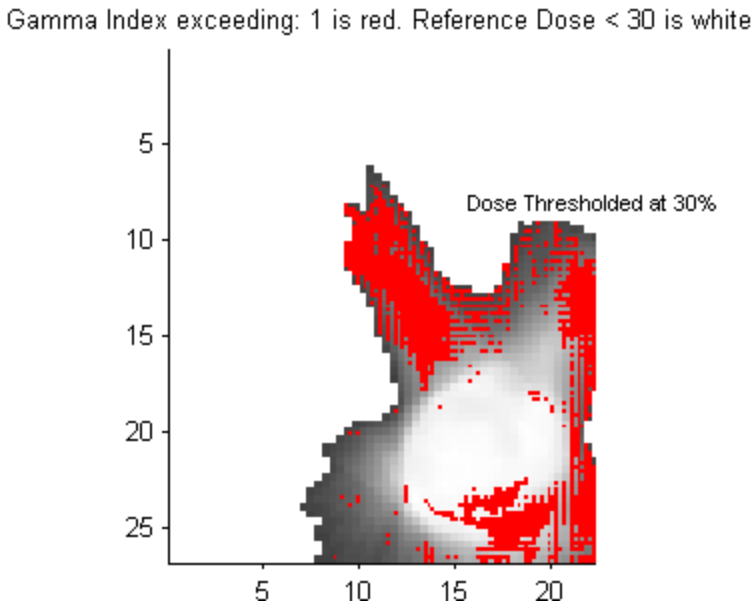

Figure 26: Gamma Pass/Fail diagram for RANDO Lung patient 7 using a 3mm DTA and 3% dose difference tolerance. The analysis region was defined as the area of film receiving over 30% of the prescribed dose.

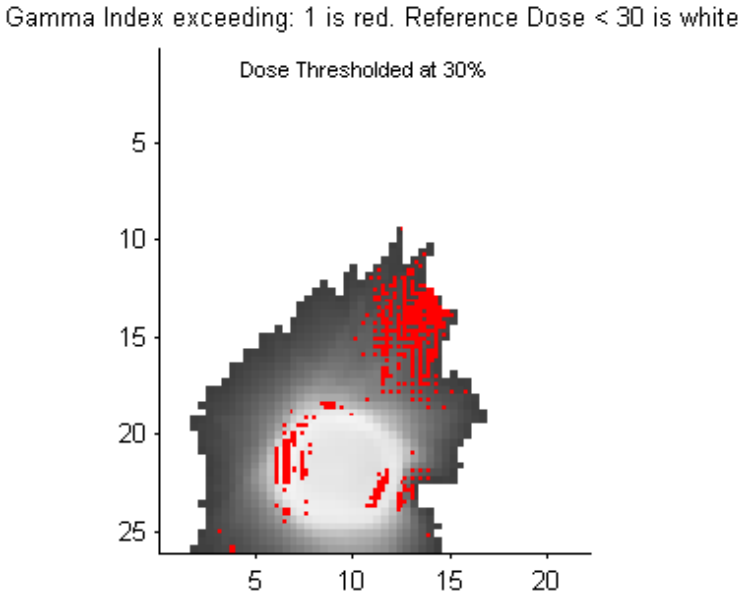

Figure 27: Gamma Pass/Fail diagram for RANDO Lung patient 8 using a 3mm DTA and 3% dose difference tolerance. The analysis region was defined as the area of film receiving over 30% of the prescribed dose.

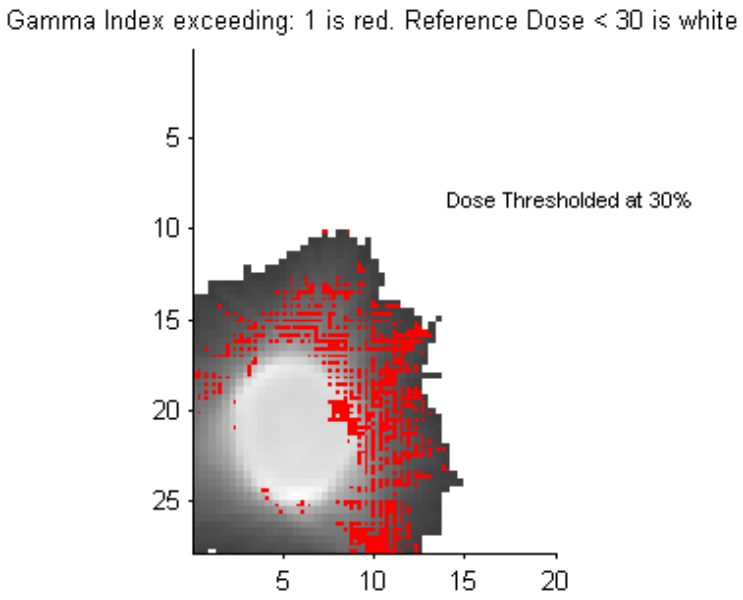

Figure 28: Gamma Pass/Fail diagram for RANDO Lung patient 9 using a 3mm DTA and 3% dose difference tolerance. The analysis region was defined as the area of film receiving over 30% of the prescribed dose.

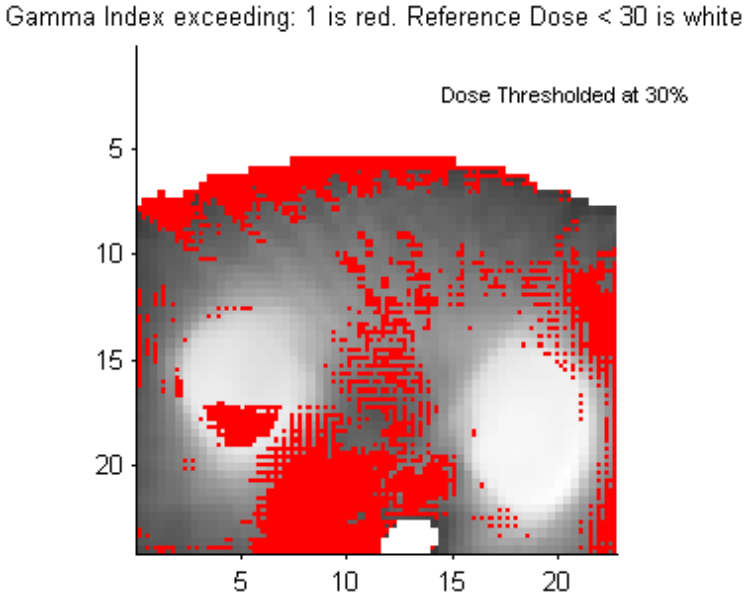

Figure 29: Gamma Pass/Fail diagram for RANDO Lung patient 10 using a 3mm DTA and 3% dose difference tolerance. The analysis region was defined as the area of film receiving over 30% of the prescribed dose.

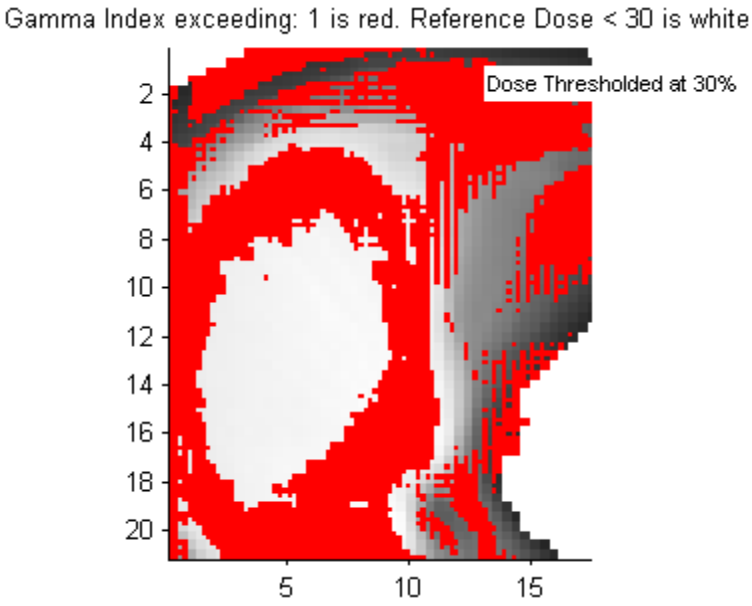

Figure 30: Gamma Pass/Fail diagram for RANDO Lung patient 11 using a 3mm DTA and 3% dose difference tolerance. The analysis region was defined as the area of film receiving over 30% of the prescribed dose.

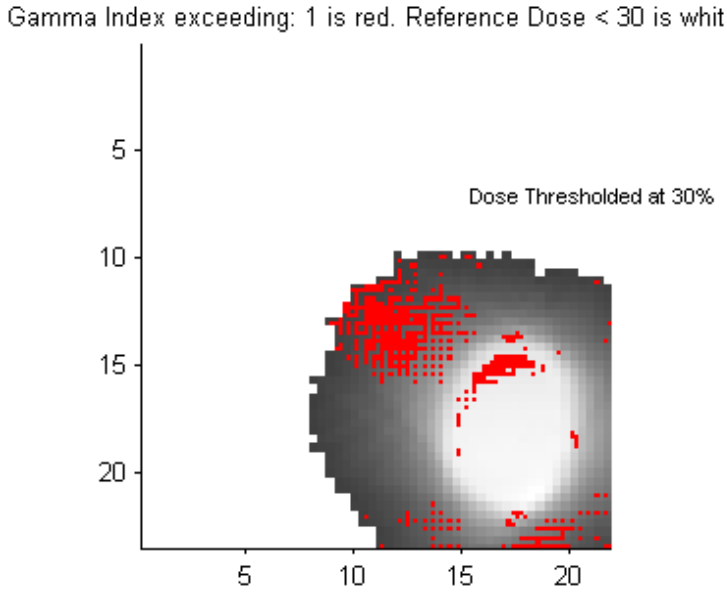

Figure 31: Gamma Pass/Fail diagram for RANDO Lung patient 12 using a 3mm DTA and 3% dose difference tolerance. The analysis region was defined as the area of film receiving over 30% of the prescribed dose.

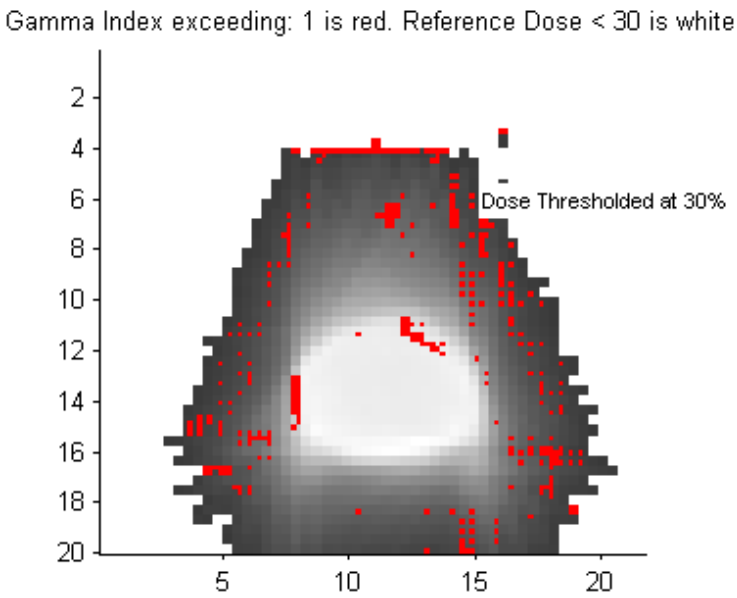

Figure 32: Gamma Pass/Fail diagram for RANDO Prostate patient 1 using a 3mm DTA and 3% dose difference tolerance. The analysis region was defined as the area of film receiving over 30% of the prescribed dose.

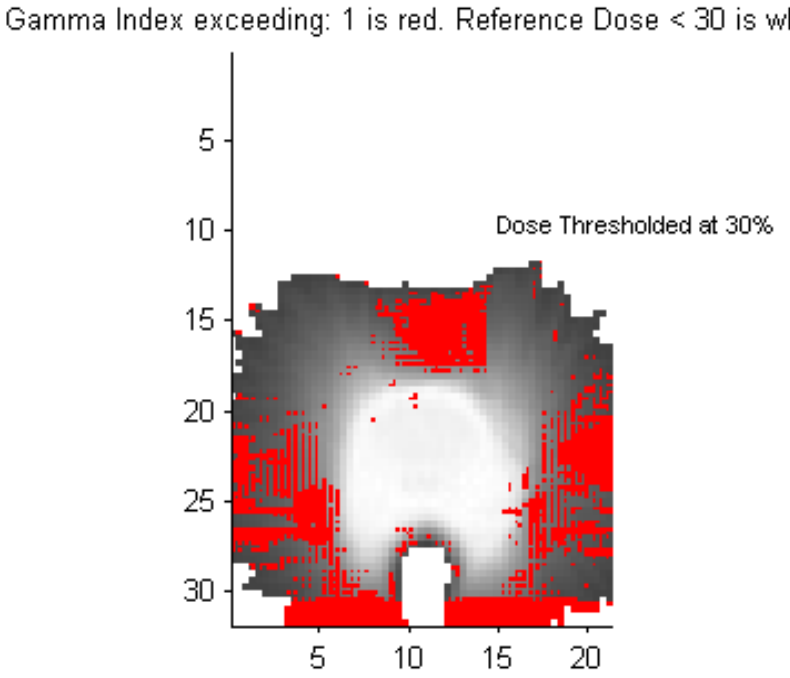

Figure 33: Gamma Pass/Fail diagram for RANDO Prostate patient 2 using a 3mm DTA and 3% dose difference tolerance. The analysis region was defined as the area of film receiving over 30% of the prescribed dose.

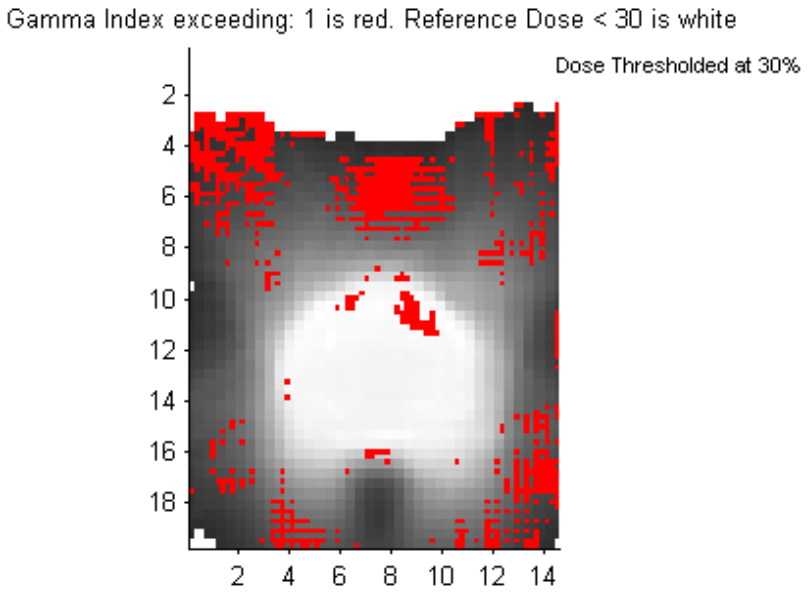

Figure 34: Gamma Pass/Fail diagram for RANDO Prostate patient 3 using a 3mm DTA and 3% dose difference tolerance. The analysis region was defined as the area of film receiving over 30% of the prescribed dose.

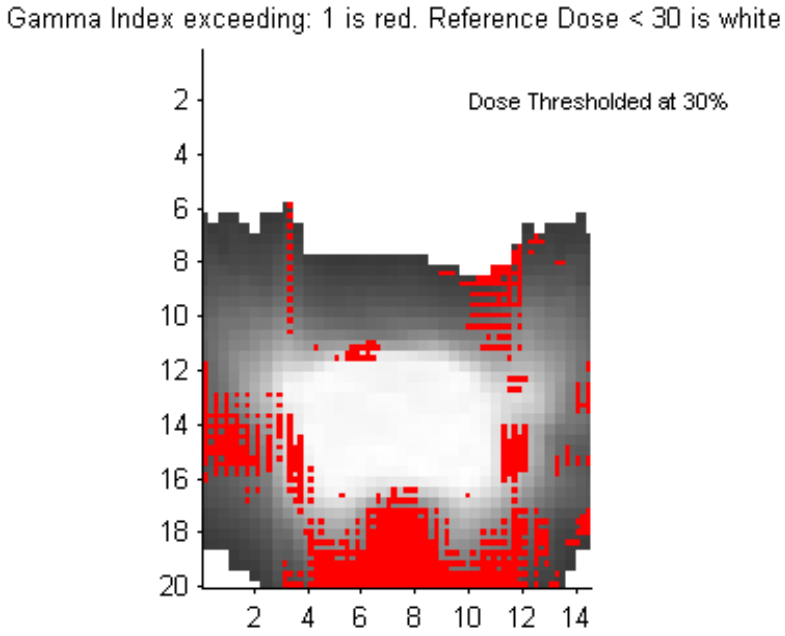

Figure 35: Gamma Pass/Fail diagram for RANDO Prostate patient 4 using a 3mm DTA and 3% dose difference tolerance. The analysis region was defined as the area of film receiving over 30% of the prescribed dose.

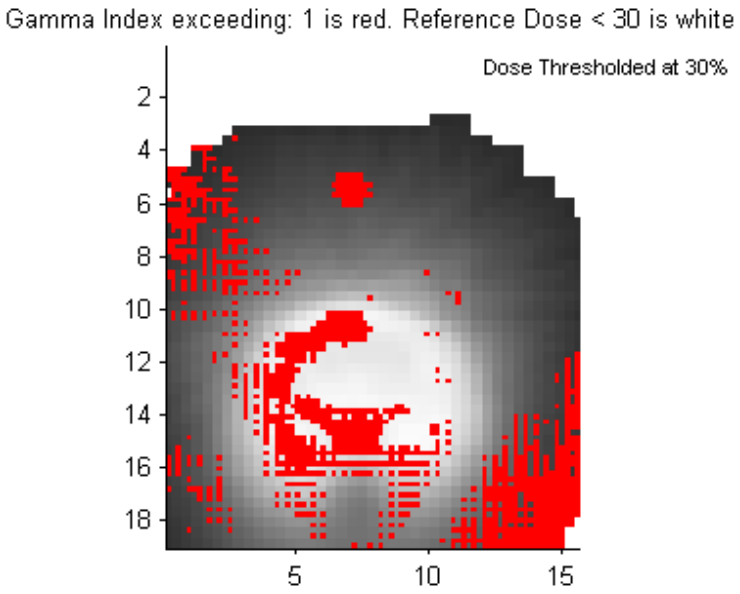

Figure 36: Gamma Pass/Fail diagram for RANDO Prostate patient 5 using a 3mm DTA and 3% dose difference tolerance. The analysis region was defined as the area of film receiving over 30% of the prescribed dose.

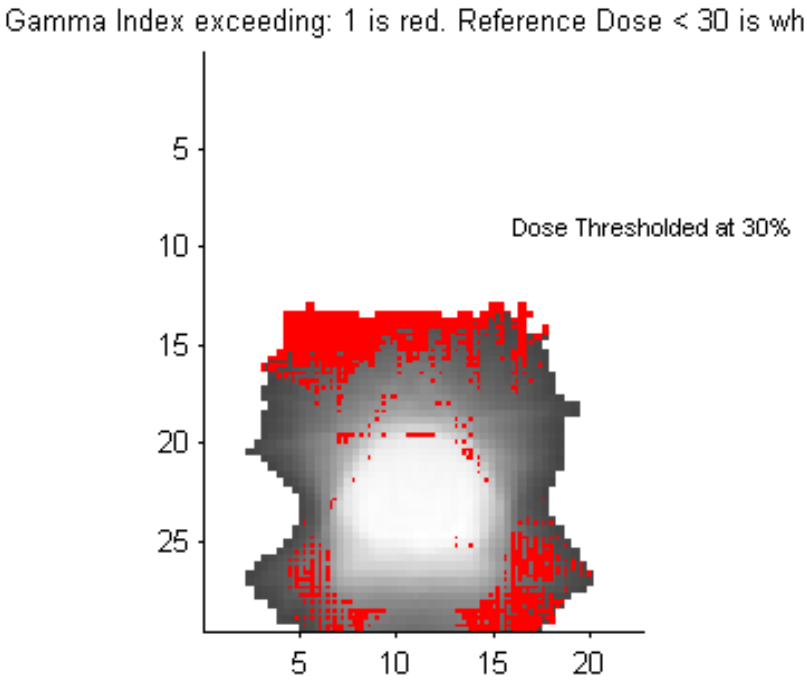

Figure 37: Gamma Pass/Fail diagram for RANDO Prostate patient 6 using a 3mm DTA and 3% dose difference tolerance. The analysis region was defined as the area of film receiving over 30% of the prescribed dose.

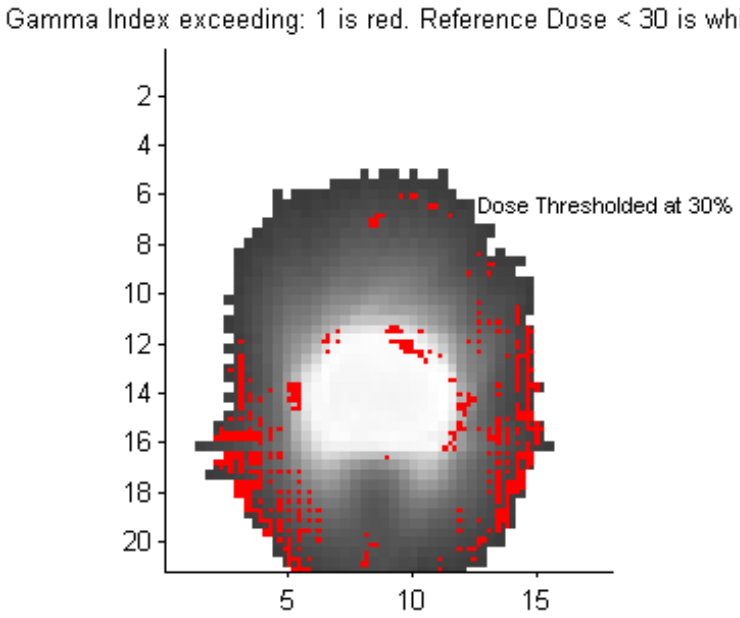

Figure 38: Gamma Pass/Fail diagram for RANDO Prostate patient 7 using a 3mm DTA and 3% dose difference tolerance. The analysis region was defined as the area of film receiving over 30% of the prescribed dose.

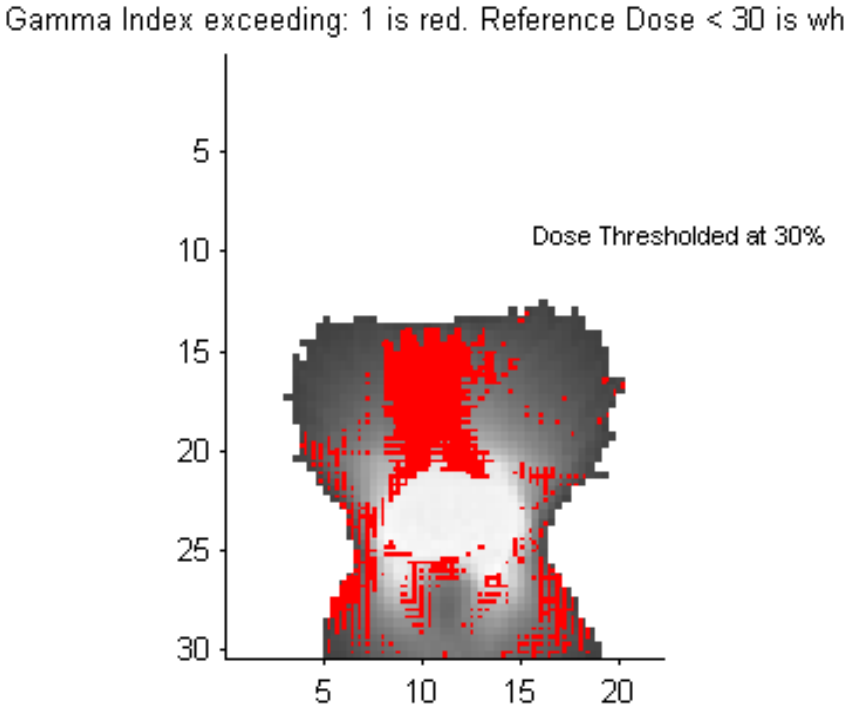

Figure 39: Gamma Pass/Fail diagram for RANDO Prostate patient 8 using a 3mm DTA and 3% dose difference tolerance. The analysis region was defined as the area of film receiving over 30% of the prescribed dose.

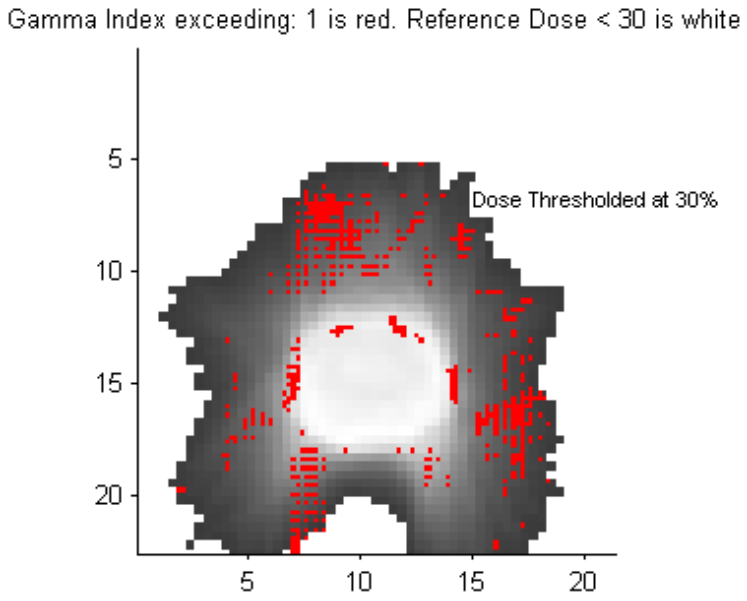

Figure 40: Gamma Pass/Fail diagram for RANDO Prostate patient 9 using a 3mm DTA and 3% dose difference tolerance. The analysis region was defined as the area of film receiving over 30% of the prescribed dose.

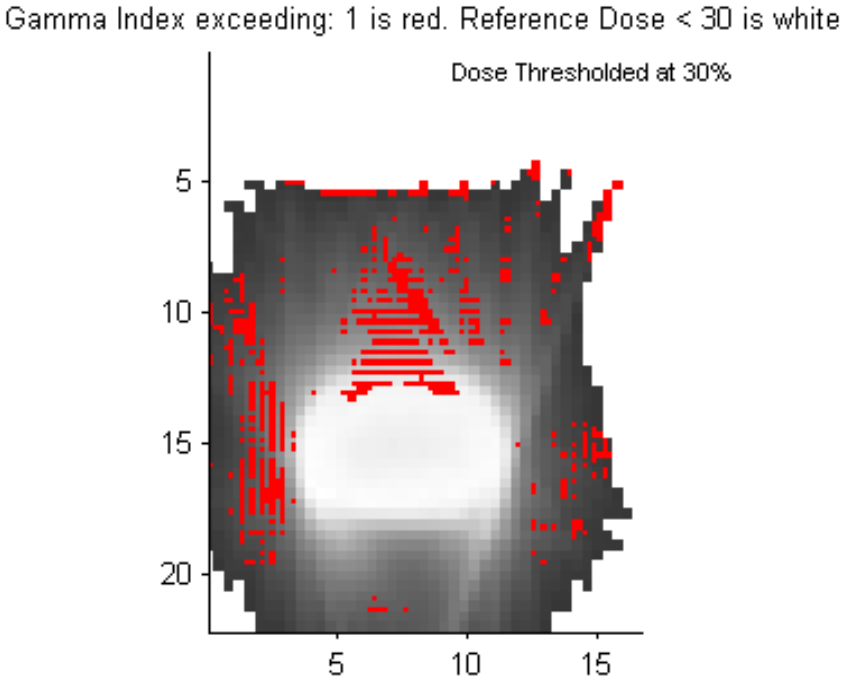

Figure 41: Gamma Pass/Fail diagram for RANDO Prostate patient 10 using a 3mm DTA and 3% dose difference tolerance. The analysis region was defined as the area of film receiving over 30% of the prescribed dose.

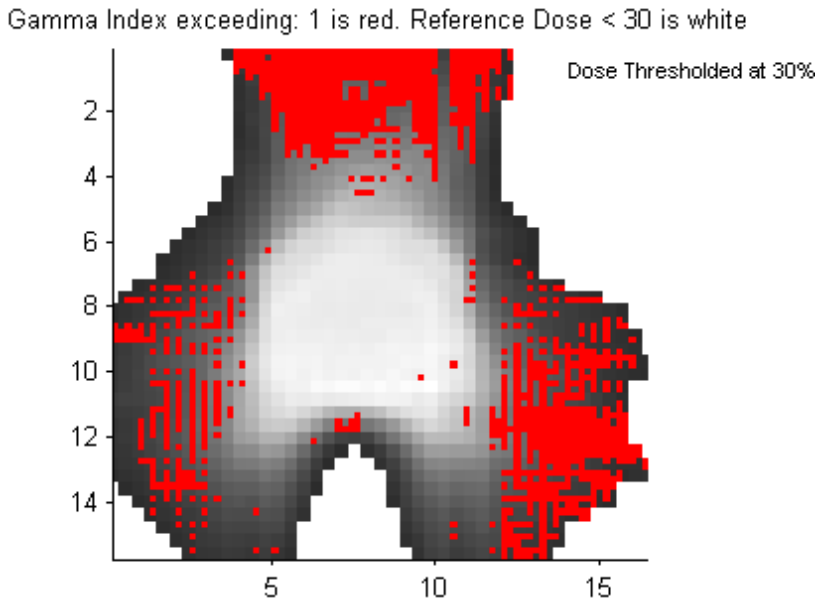

Figure 42: Gamma Pass/Fail diagram for RANDO Prostate patient 11 using a 3mm DTA and 3% dose difference tolerance. The analysis region was defined as the area of film receiving over 30% of the prescribed dose.

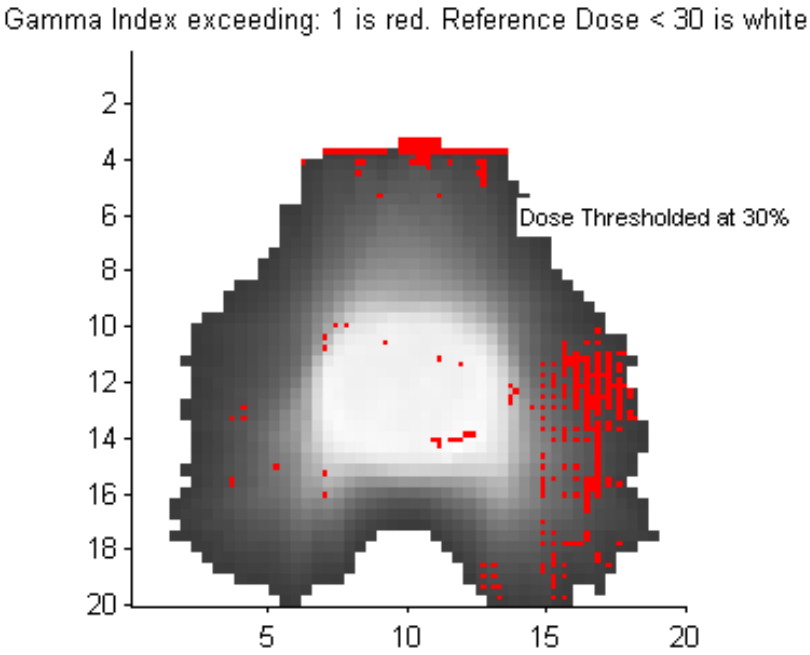

Figure 43: Gamma Pass/Fail diagram for RANDO Prostate patient 12 using a 3mm DTA and 3% dose difference tolerance. The analysis region was defined as the area of film receiving over 30% of the prescribed dose.

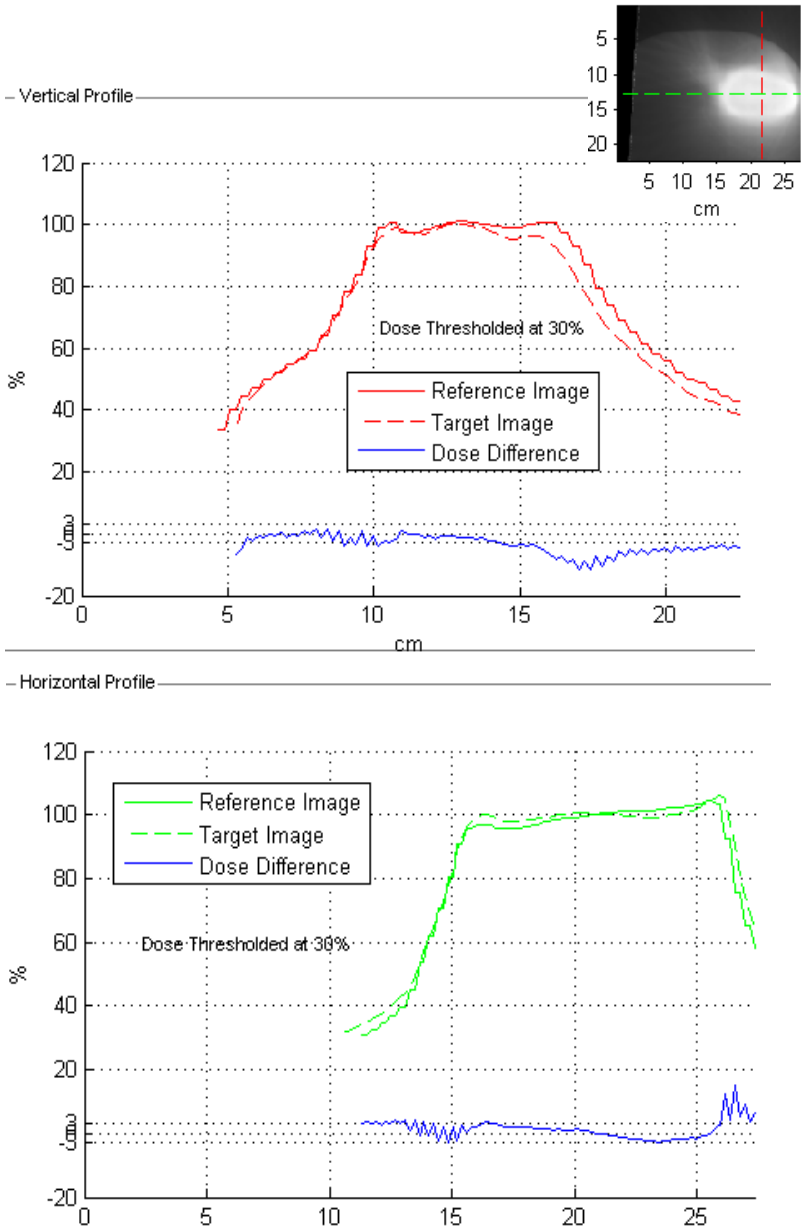

Figure 44: Horizontal and Vertical profiles for RANDO lung patient 1. Horizontal and vertical profiles spatially evaluate the dose distribution between the calculated and measured profiles.

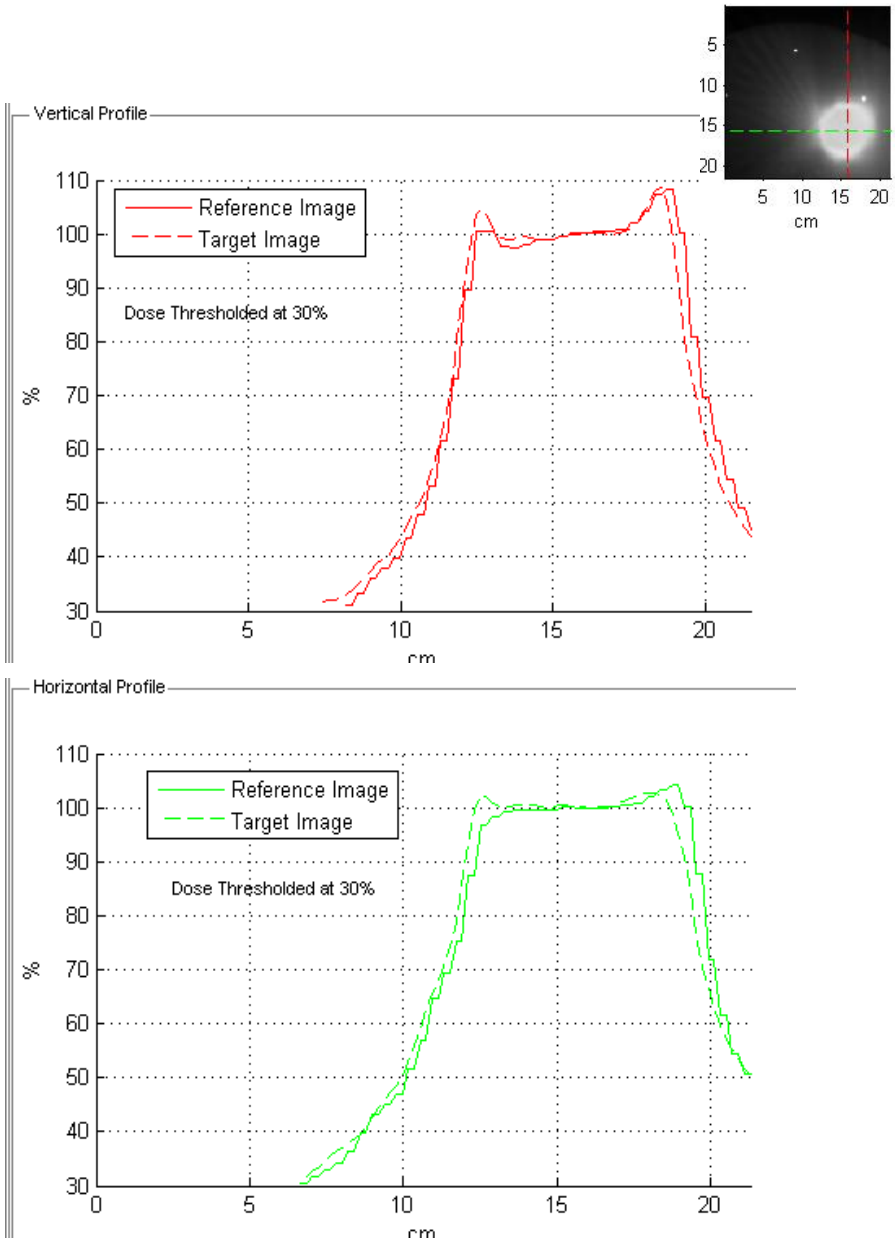

Figure 45: Horizontal and Vertical profiles for RANDO lung patient 2. Horizontal and vertical profiles spatially evaluate the dose distribution between the calculated and measured profiles.

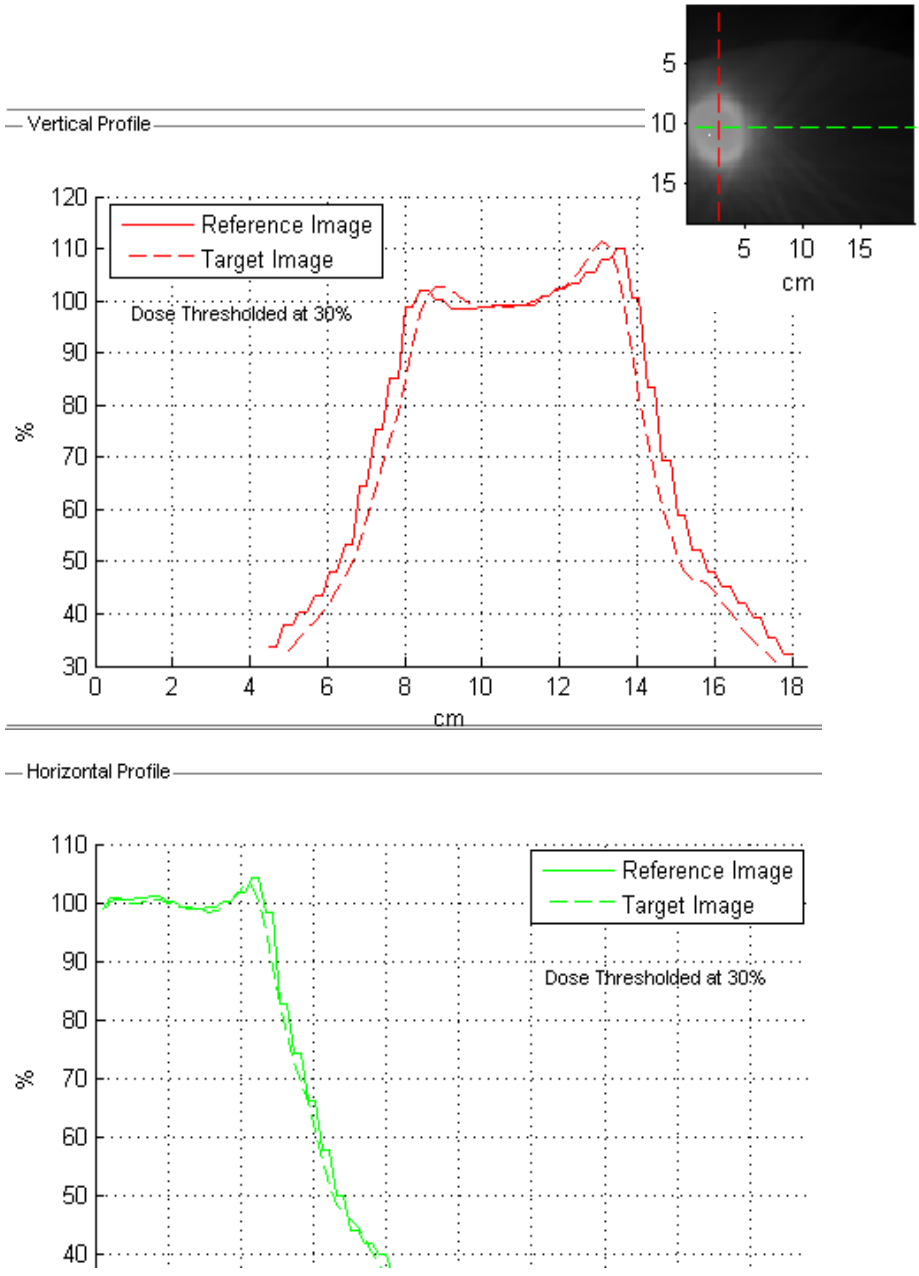

Figure 46: Horizontal and Vertical profiles for RANDO lung patient 3. Horizontal and vertical profiles spatially evaluate the dose distribution between the calculated and measured profiles.

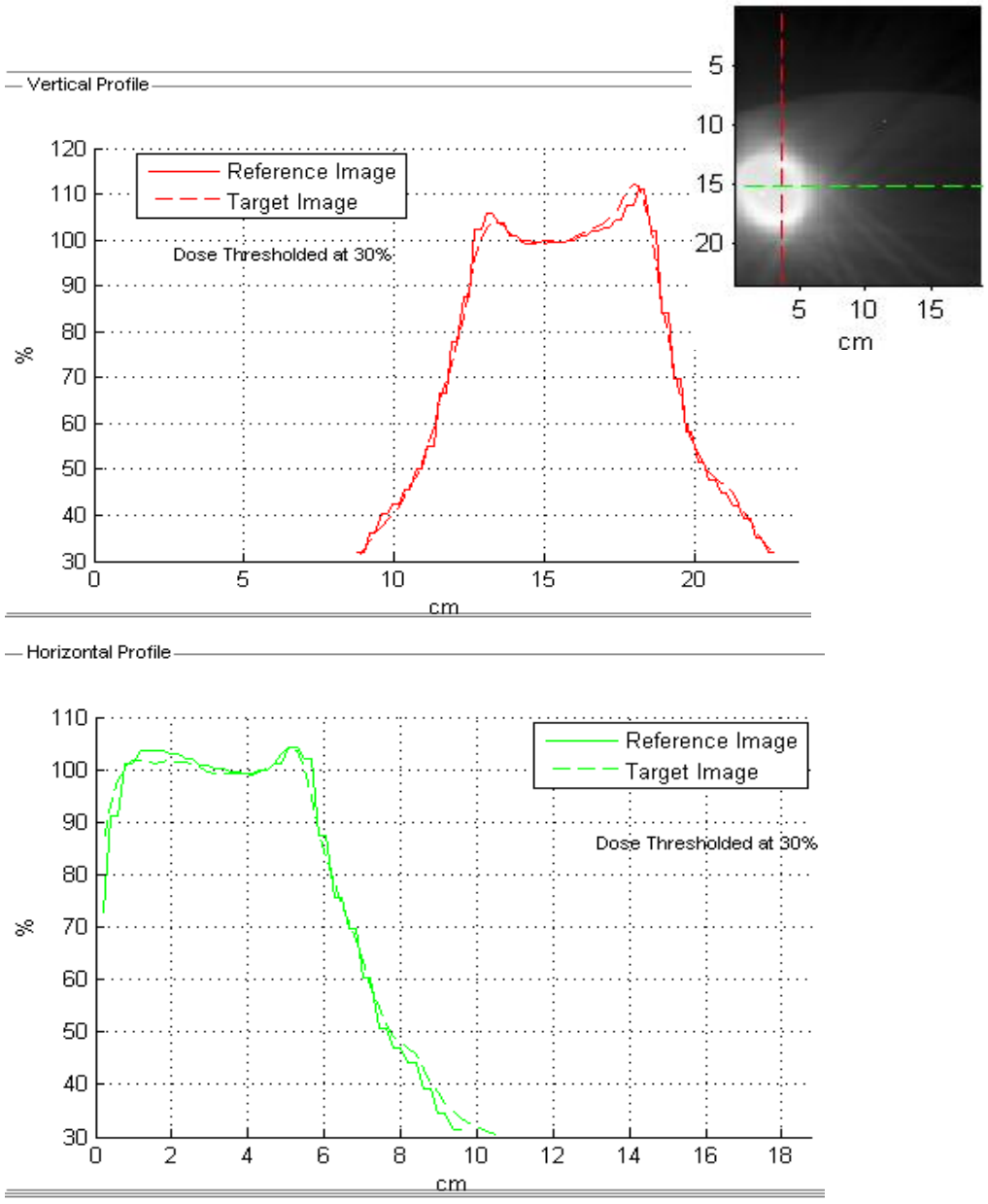

Figure 47: Horizontal and Vertical profiles for RANDO lung patient 4. Horizontal and vertical profiles spatially evaluate the dose distribution between the calculated and measured profiles.

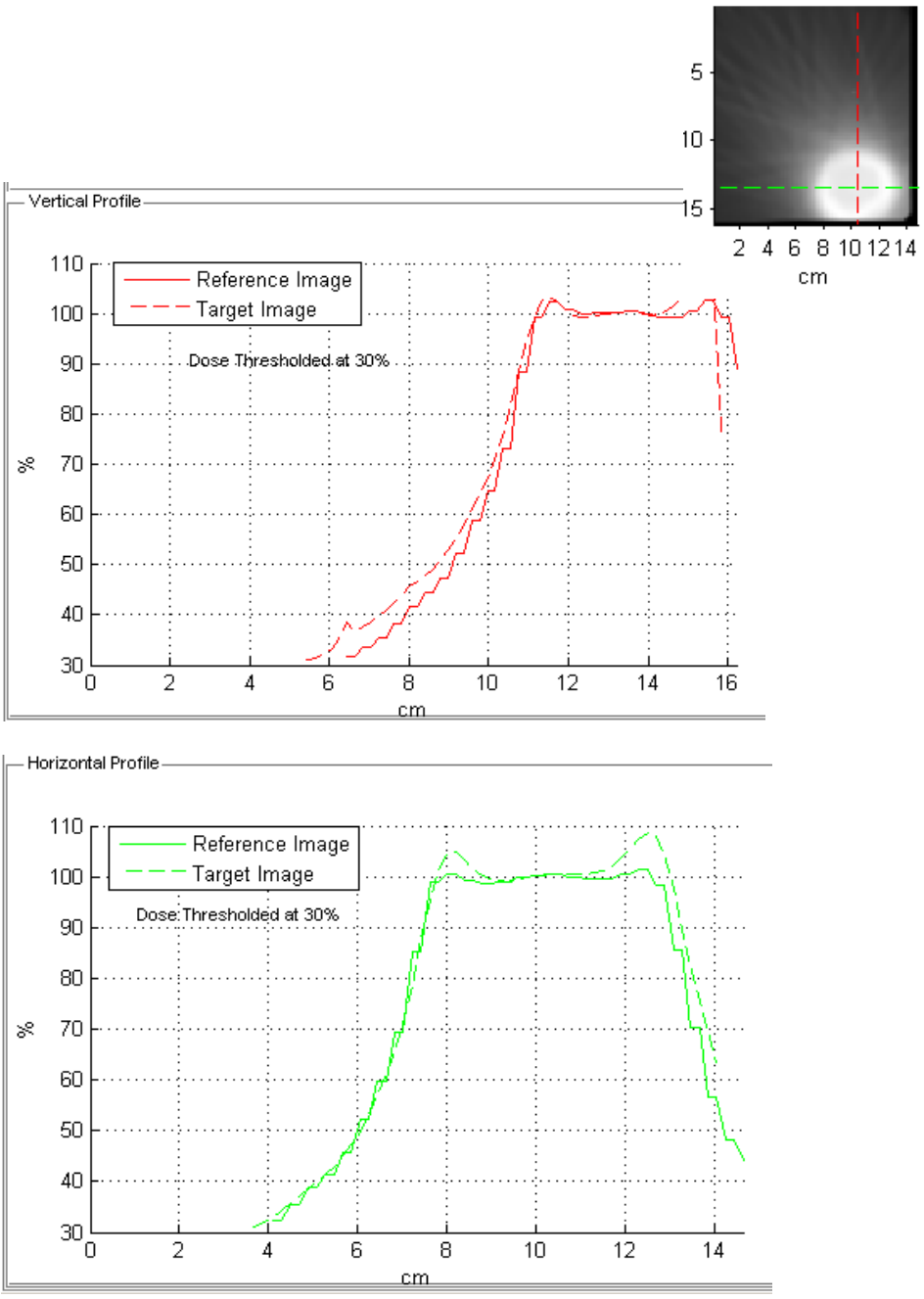

Figure 48: Horizontal and Vertical profiles for RANDO lung patient 5. Horizontal and vertical profiles spatially evaluate the dose distribution between the calculated and measured profiles.

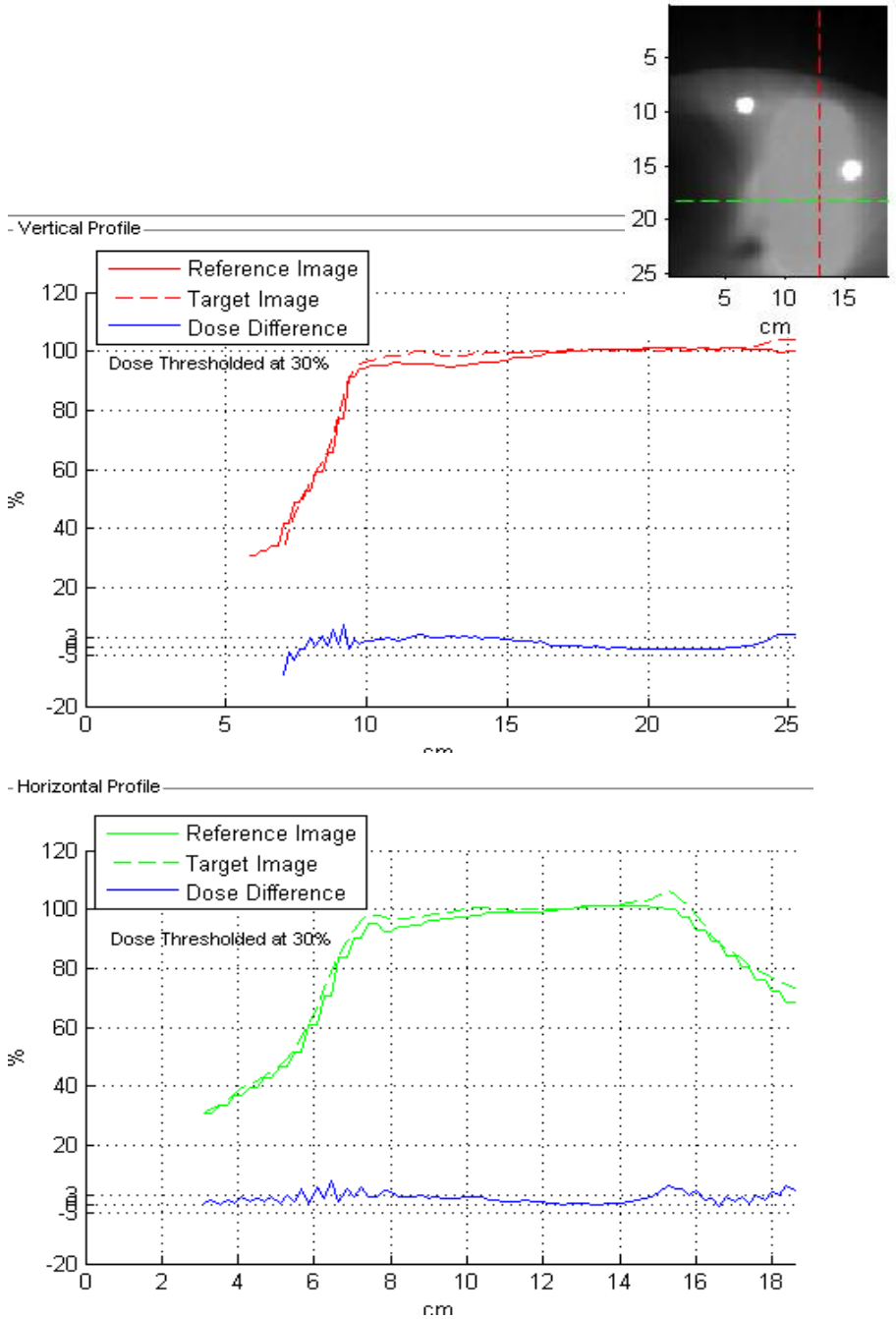

Figure 49: Horizontal and Vertical profiles for RANDO lung patient 6. Horizontal and vertical profiles spatially evaluate the dose distribution between the calculated and measured profiles.

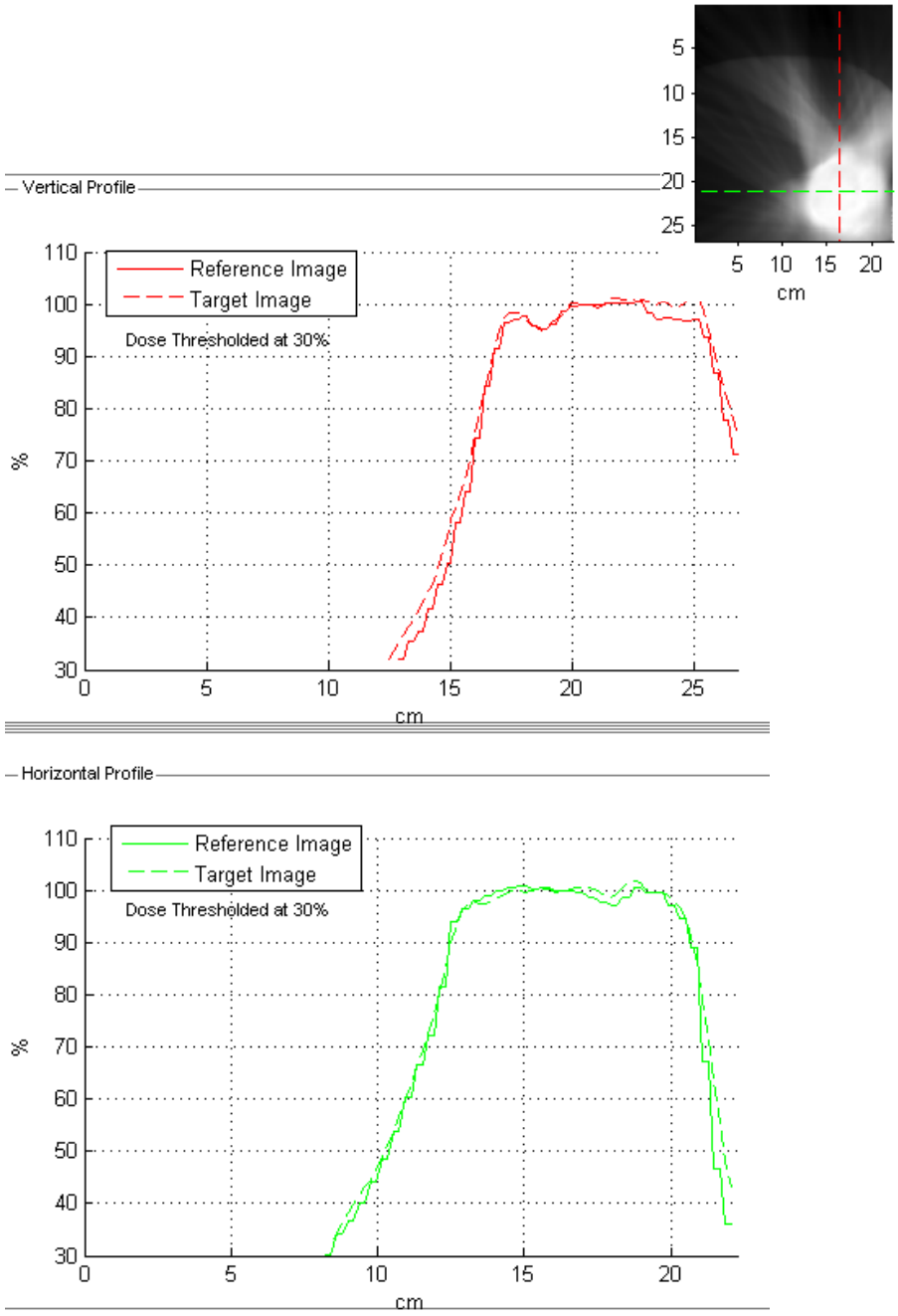

Figure 50: Horizontal and Vertical profiles for RANDO lung patient 7. Horizontal and vertical profiles spatially evaluate the dose distribution between the calculated and measured profiles.

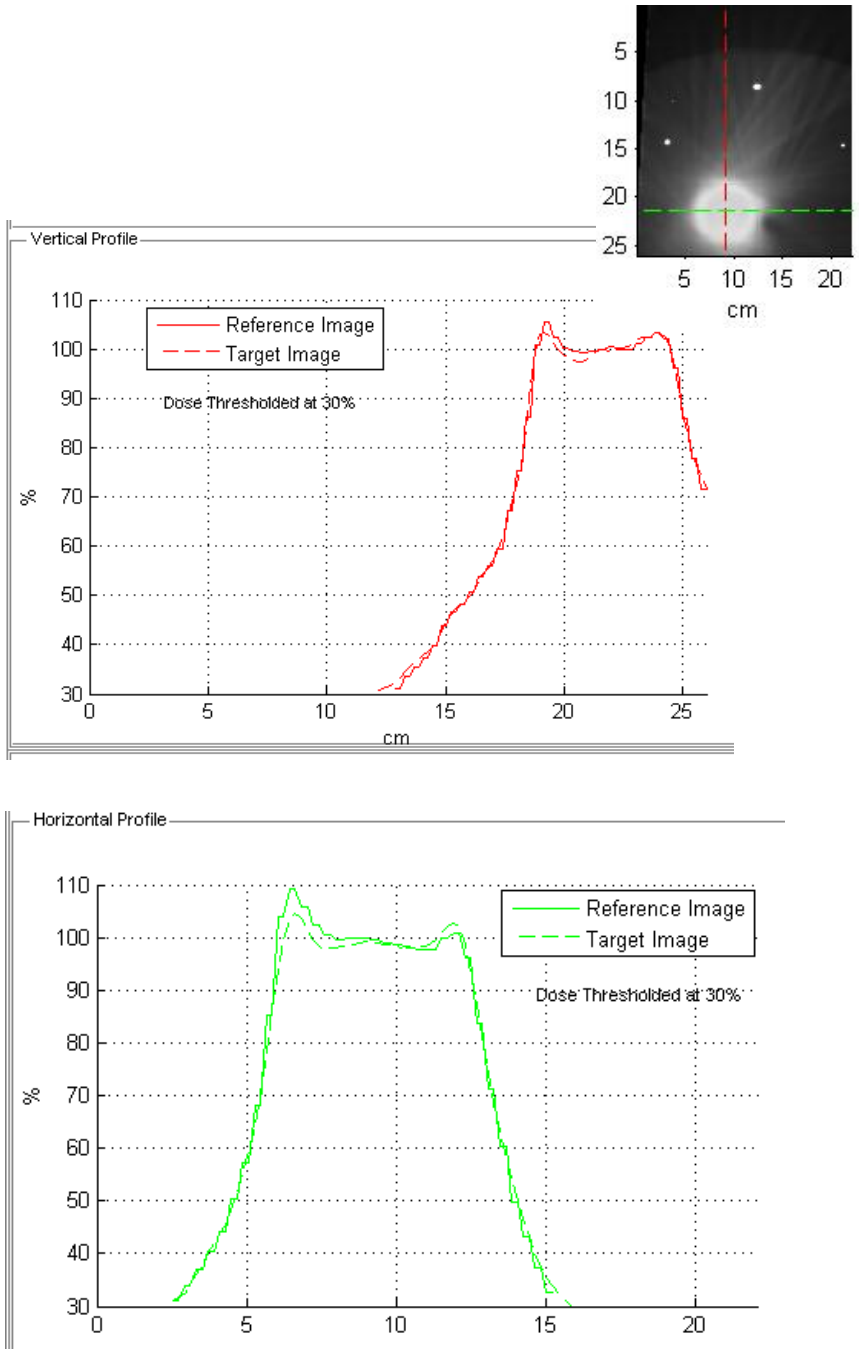

Figure 51: Horizontal and Vertical profiles for RANDO lung patient 8. Horizontal and vertical profiles spatially evaluate the dose distribution between the calculated and measured profiles.

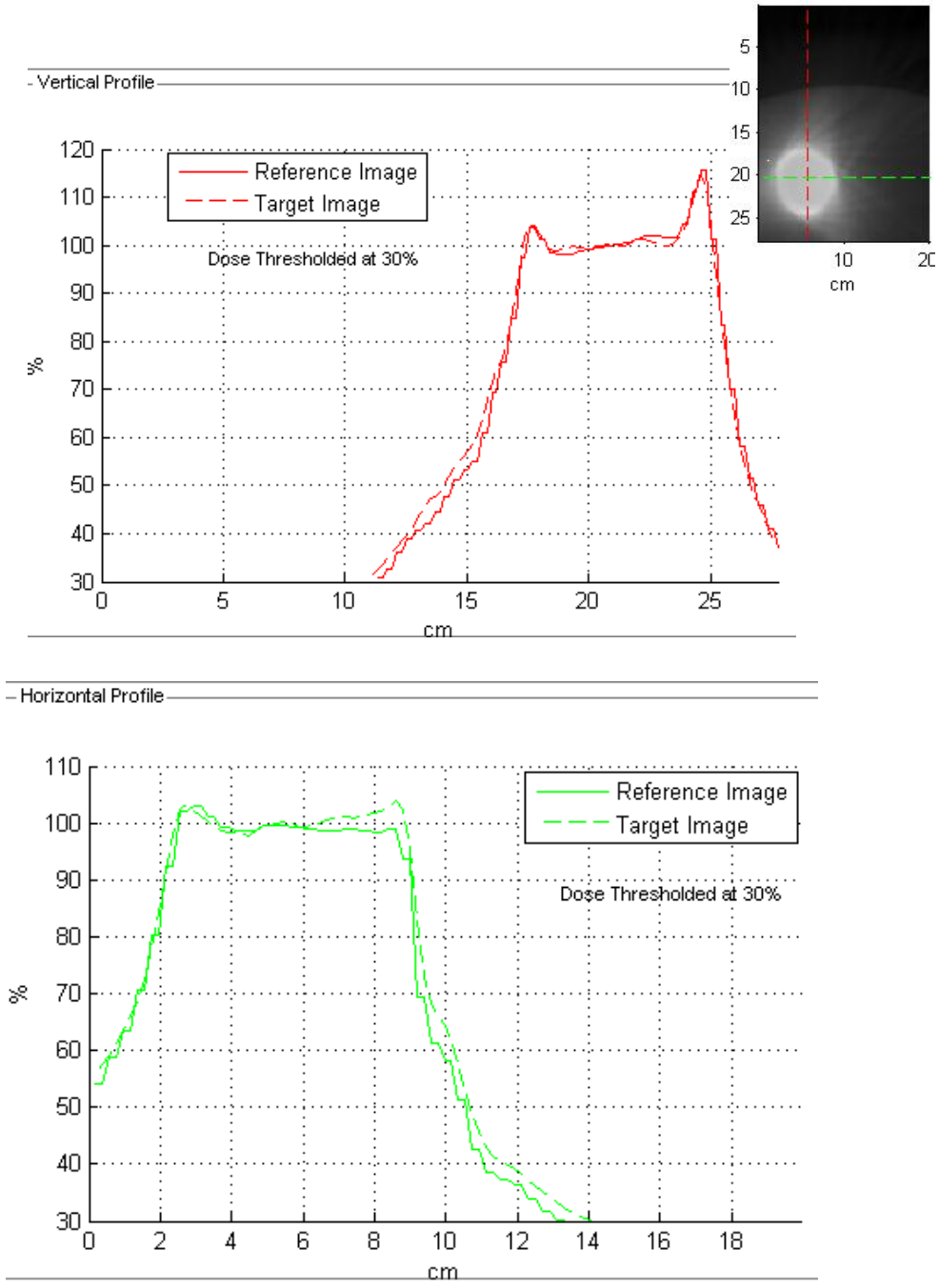

Figure 52: Horizontal and Vertical profiles for RANDO lung patient 9. Horizontal and vertical profiles spatially evaluate the dose distribution between the calculated and measured profiles.

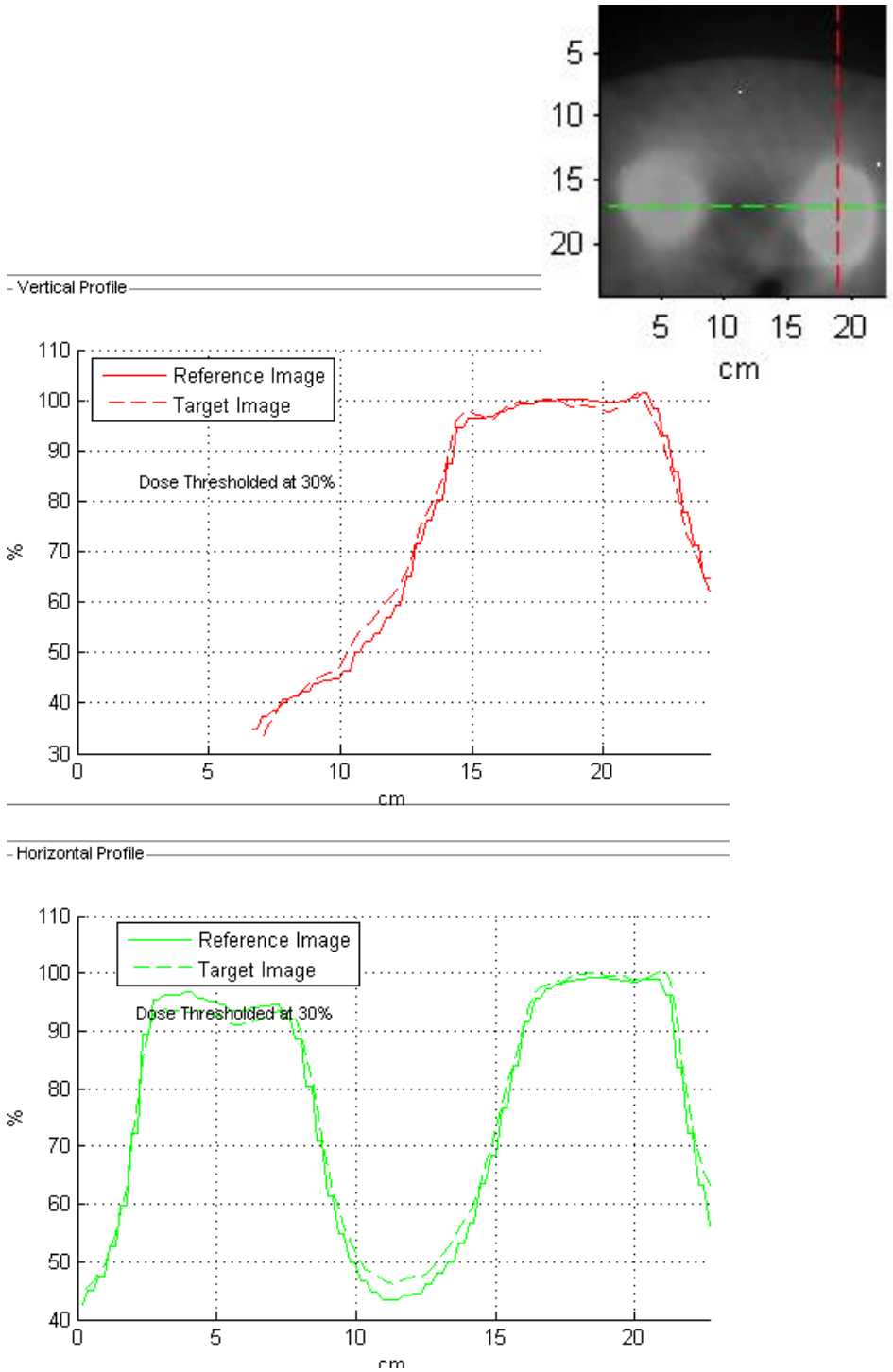

Figure 53: Horizontal and Vertical profiles for RANDO lung patient 10. Horizontal and vertical profiles spatially evaluate the dose distribution between the calculated and measured profiles.

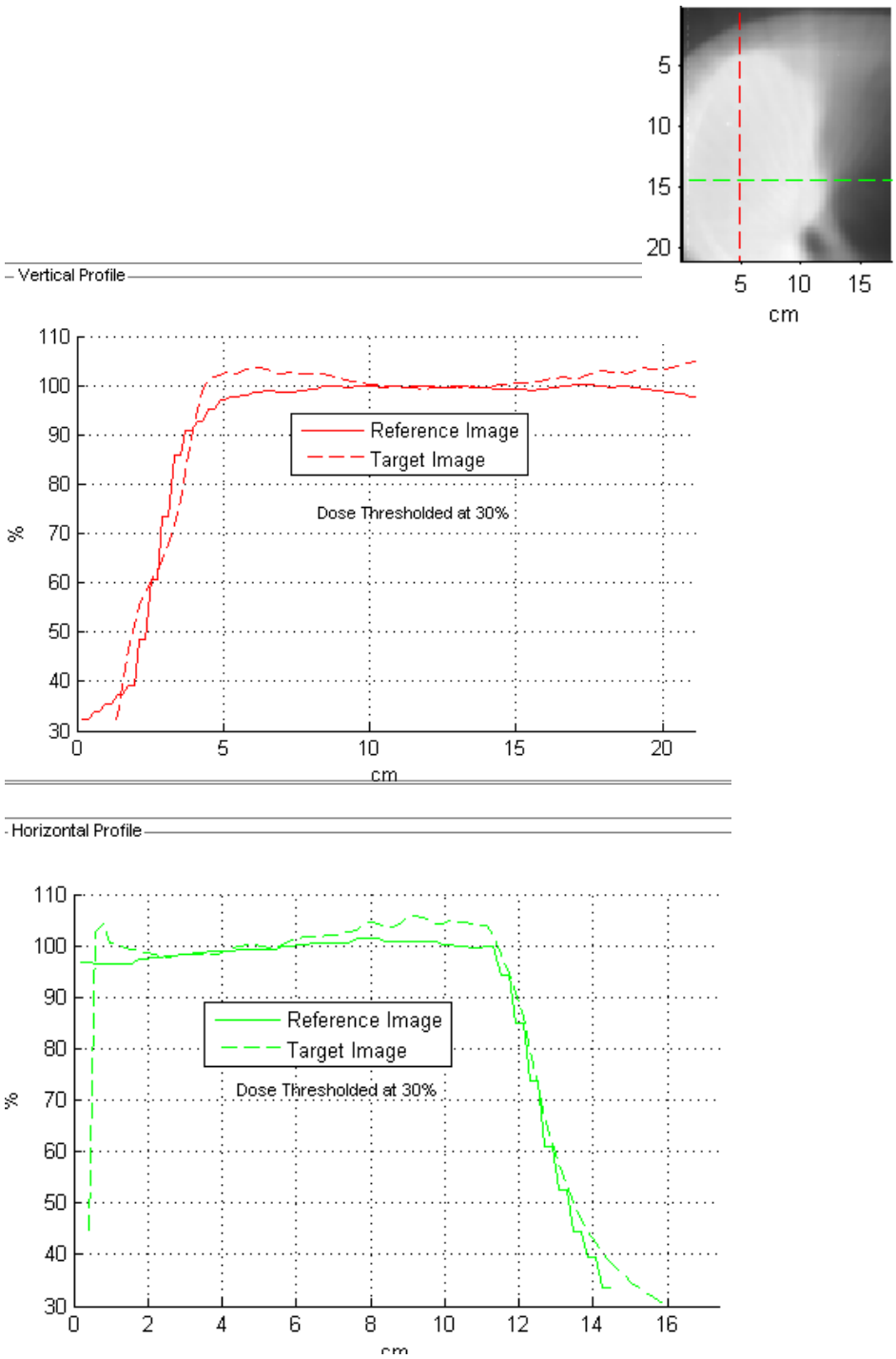

Figure 54: Horizontal and Vertical profiles for RANDO lung patient 11. Horizontal and vertical profiles spatially evaluate the dose distribution between the calculated and measured profiles.

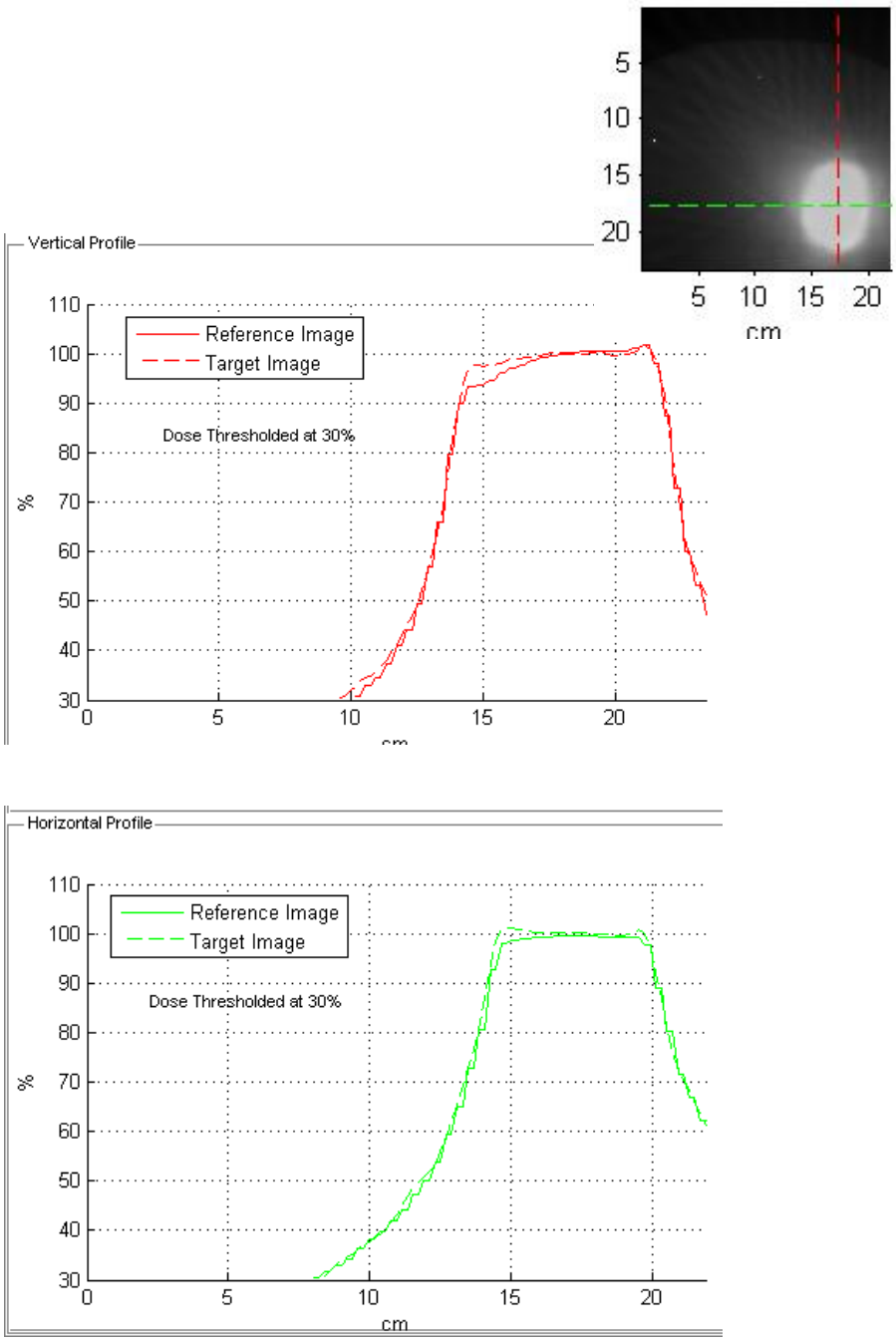

Figure 55: Horizontal and Vertical profiles for RANDO lung patient 12. Horizontal and vertical profiles spatially evaluate the dose distribution between the calculated and measured profiles.

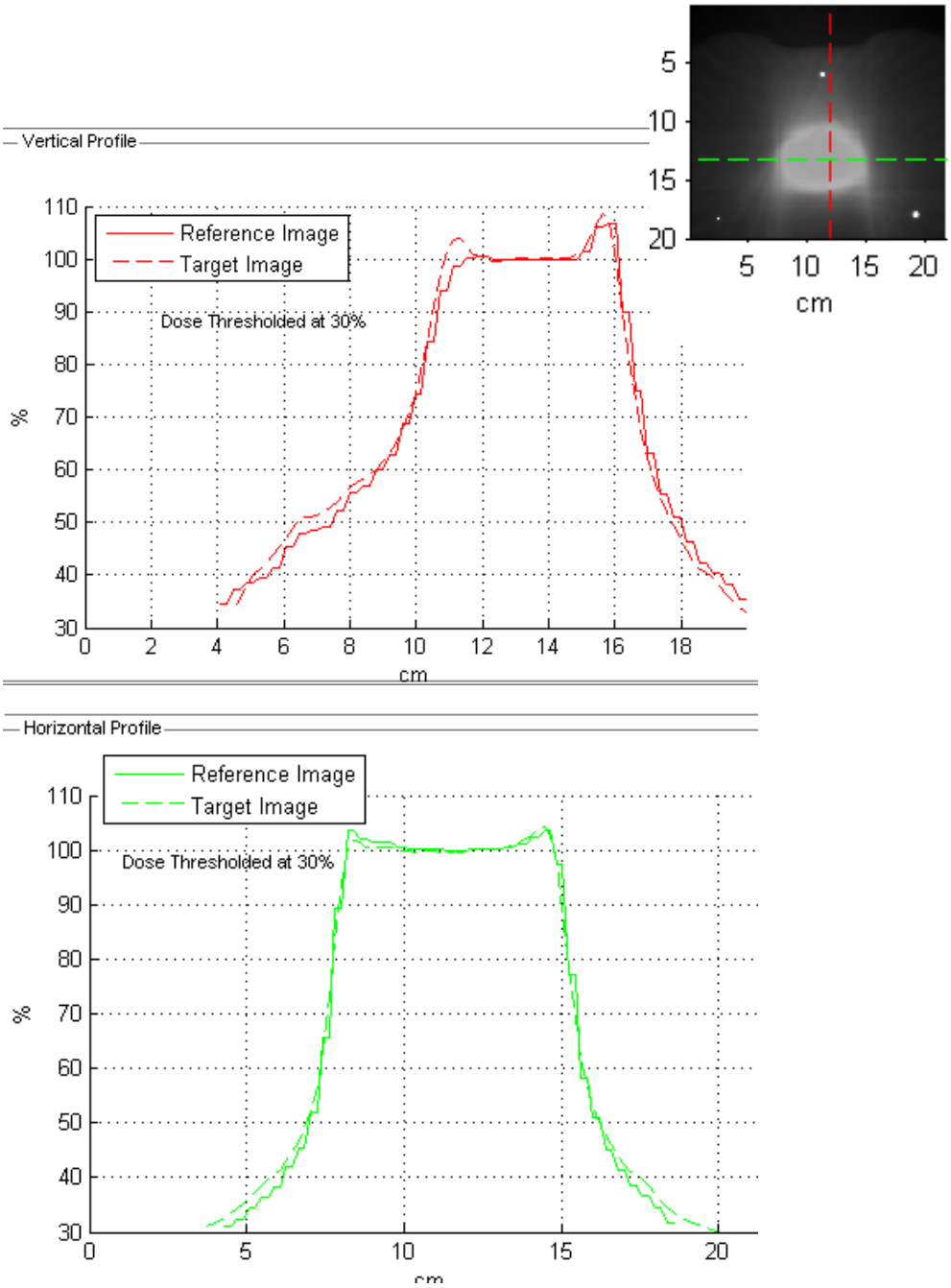

Figure 56: Horizontal and Vertical profiles for RANDO prostate patient 1. Horizontal and vertical profiles spatially evaluate the dose distribution between the calculated and measured profiles.

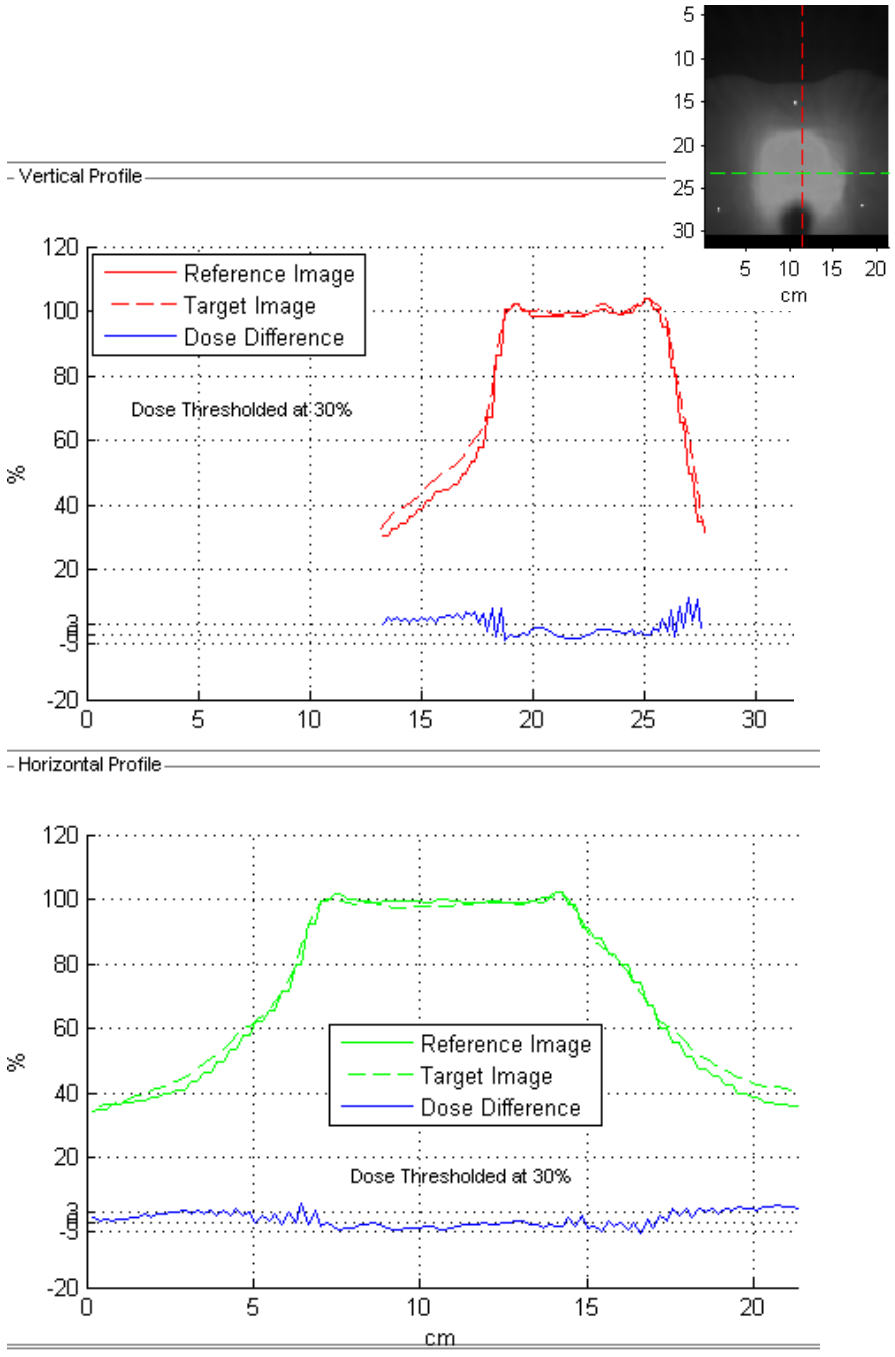

Figure 57: Horizontal and Vertical profiles for RANDO prostate patient 2. Horizontal and vertical profiles spatially evaluate the dose distribution between the calculated and measured profiles.

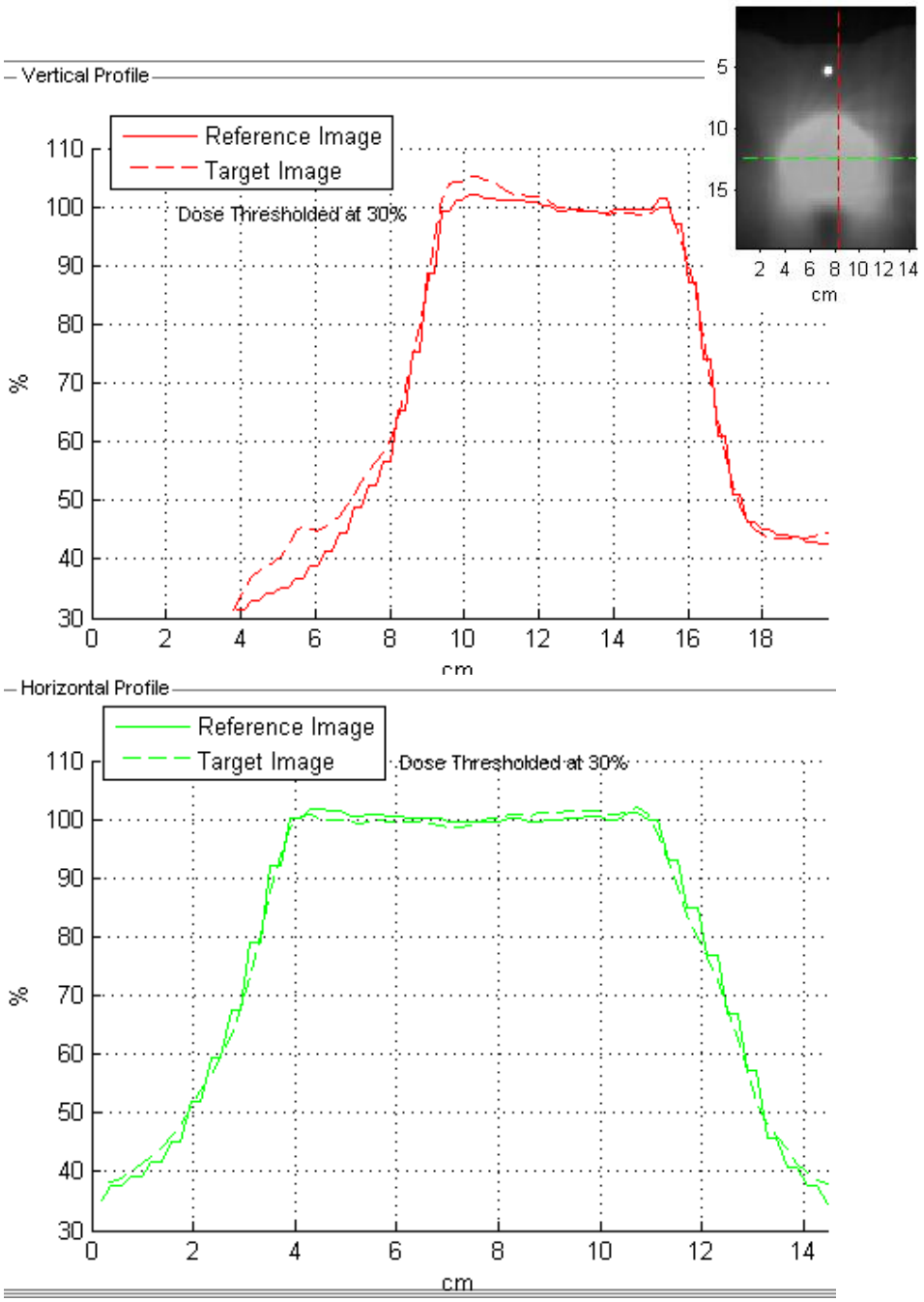

Figure 58: Horizontal and Vertical profiles for RANDO prostate patient 3. Horizontal and vertical profiles spatially evaluate the dose distribution between the calculated and measured profiles.

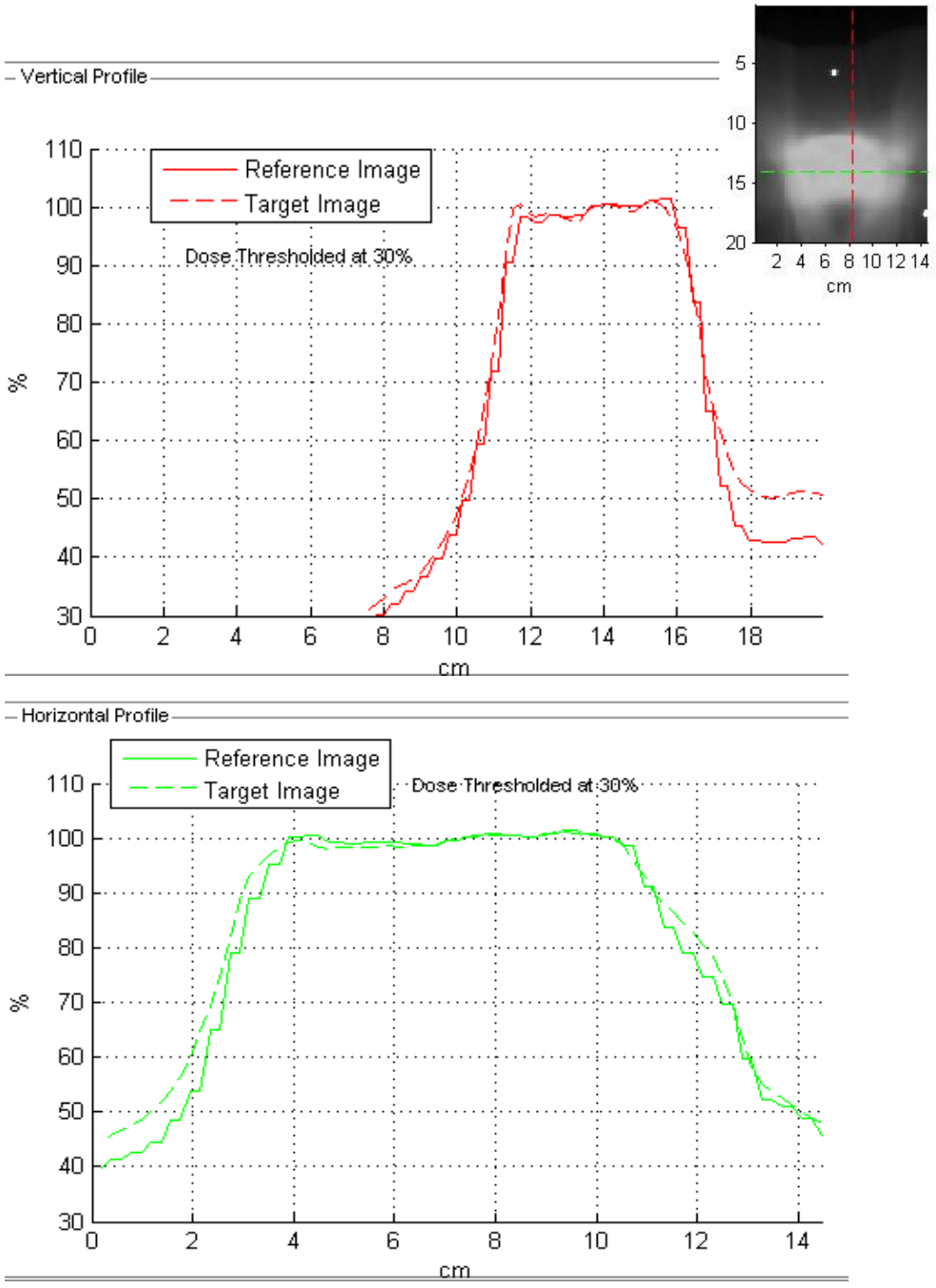

Figure 59: Horizontal and Vertical profiles for RANDO prostate patient 4. Horizontal and vertical profiles spatially evaluate the dose distribution between the calculated and measured profiles.

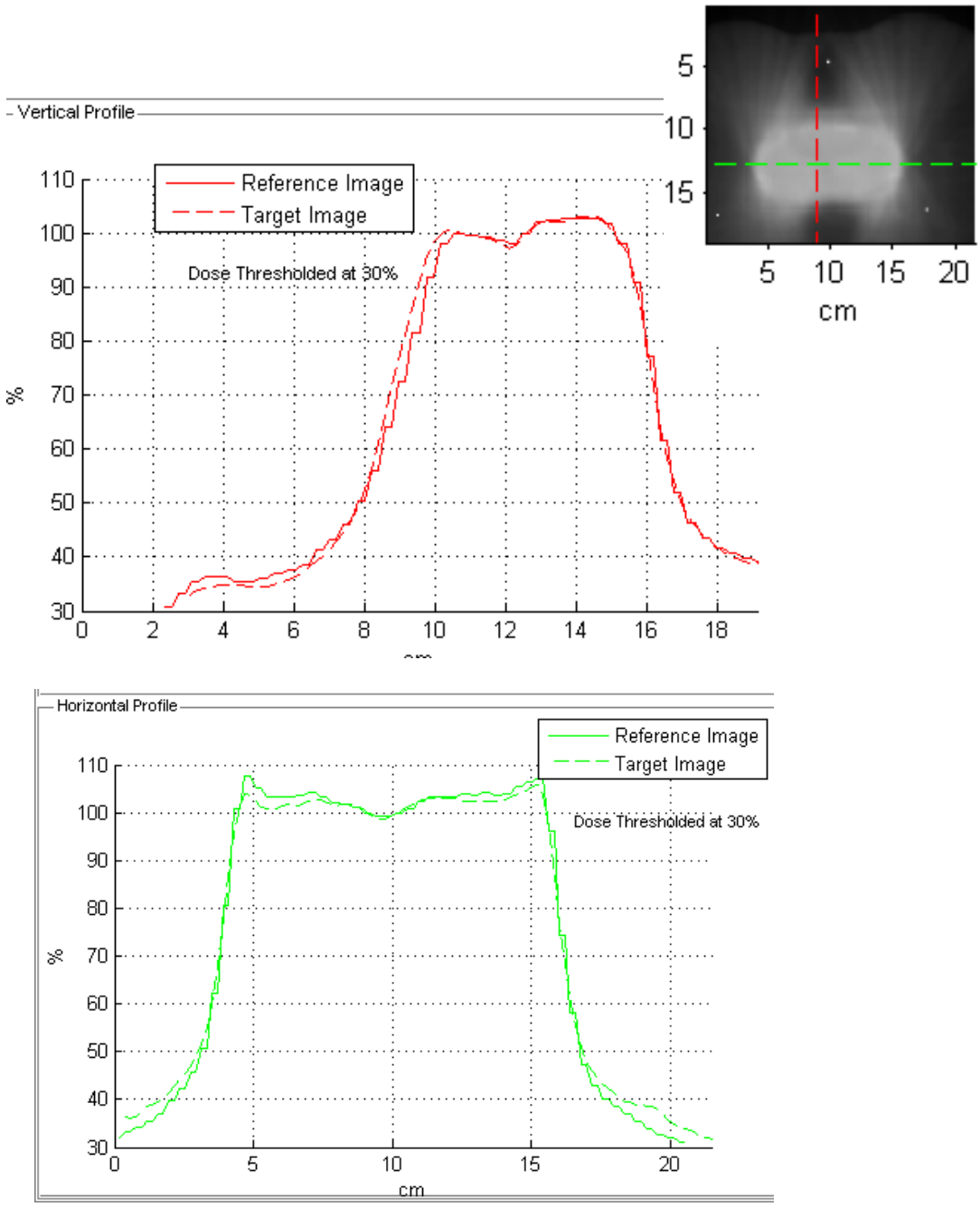

Figure 60: Horizontal and Vertical profiles for RANDO prostate patient 5. Horizontal and vertical profiles spatially evaluate the dose distribution between the calculated and measured profiles.

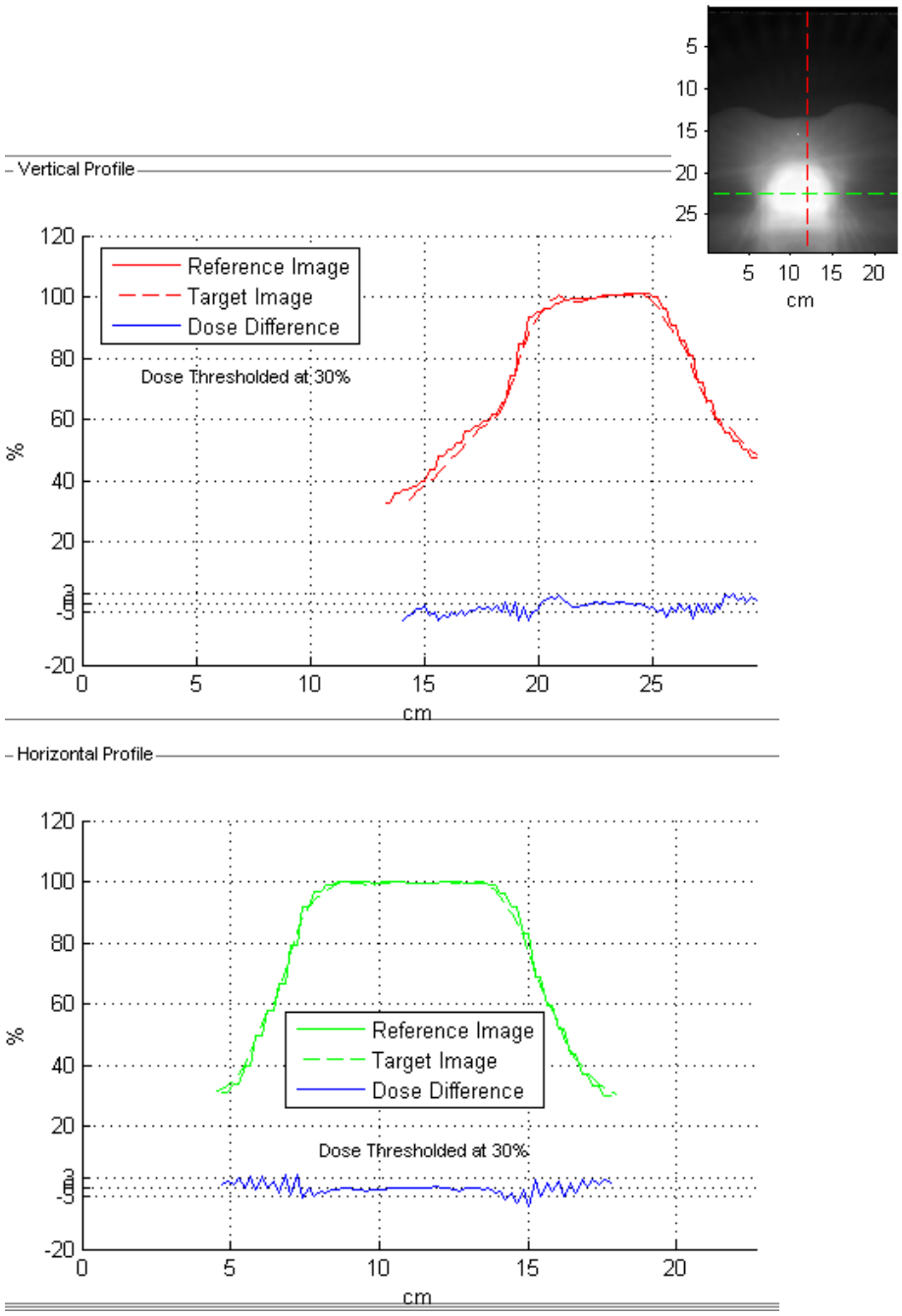

Figure 61: Horizontal and Vertical profiles for RANDO prostate patient 6. Horizontal and vertical profiles spatially evaluate the dose distribution between the calculated and measured profiles.

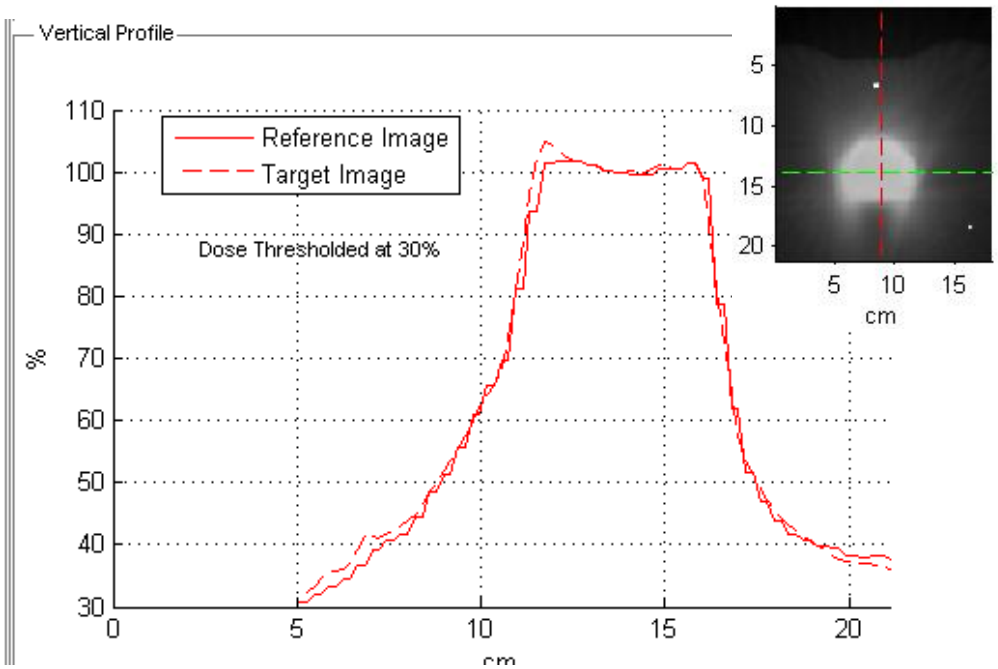

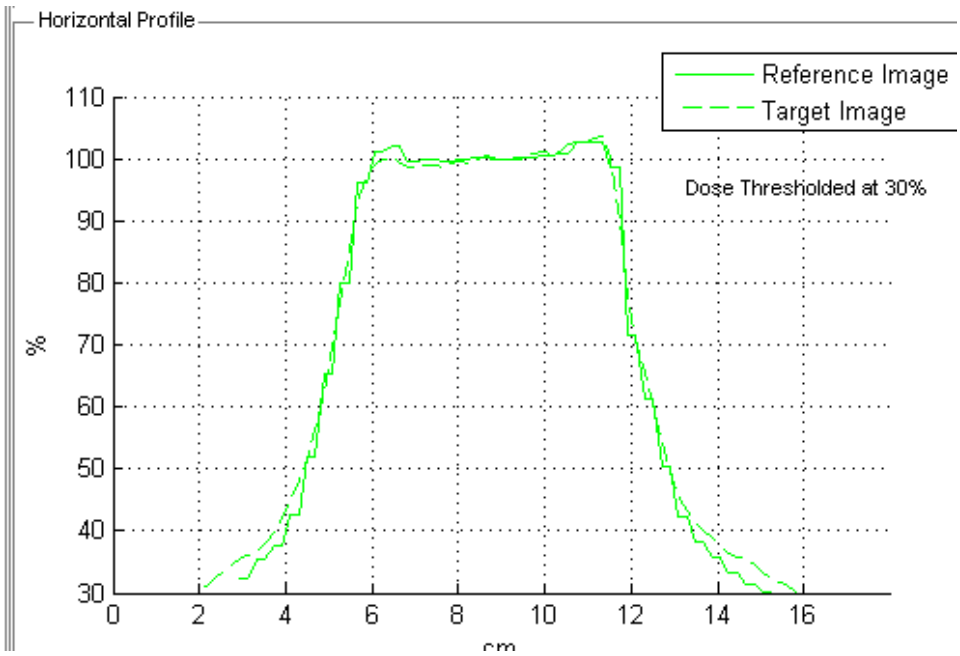

Figure 62: Horizontal and Vertical profiles for RANDO prostate patient 7. Horizontal and vertical profiles spatially evaluate the dose distribution between the calculated and measured profiles.

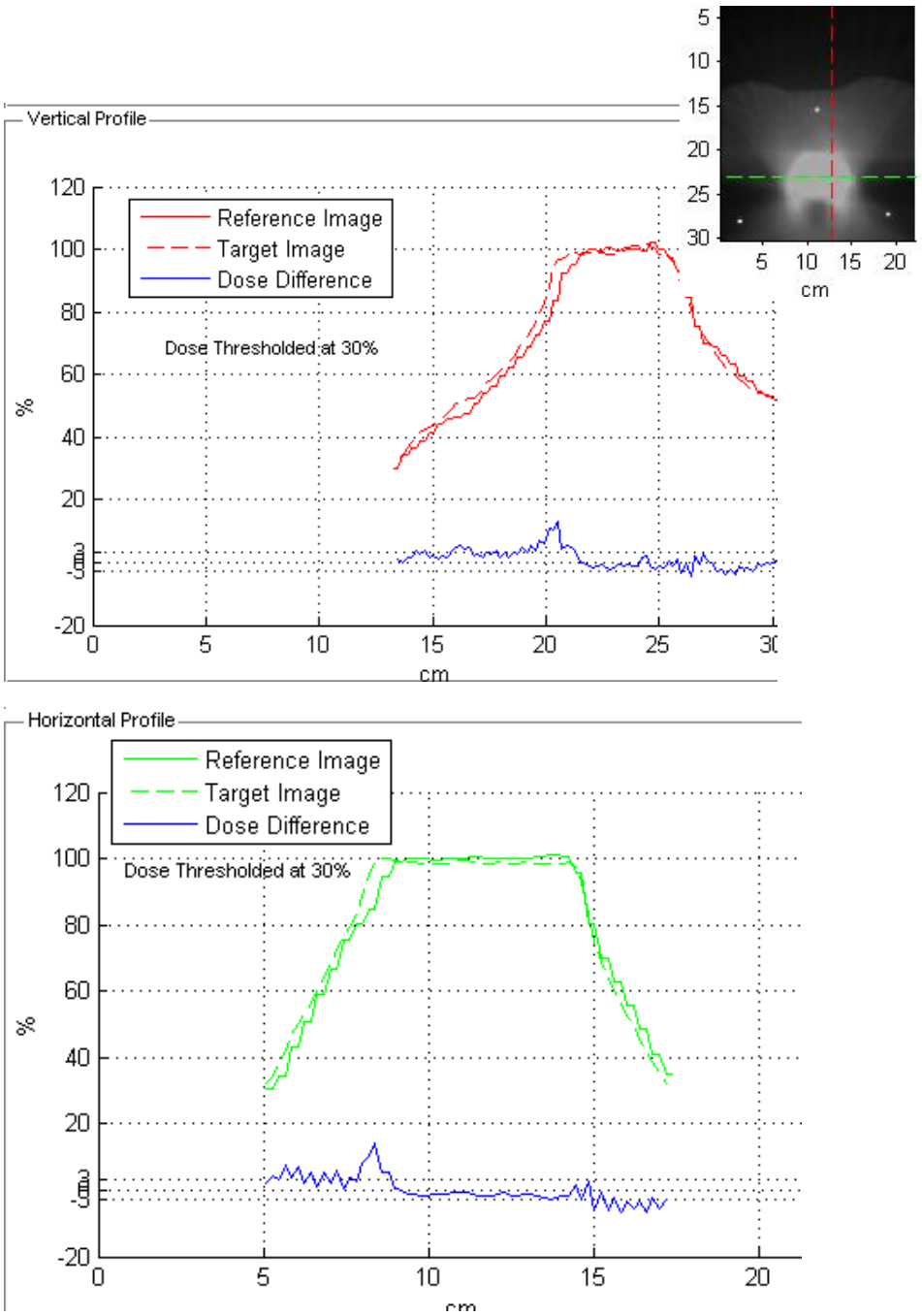

Figure 63: Horizontal and Vertical profiles for RANDO prostate patient 8. Horizontal and vertical profiles spatially evaluate the dose distribution between the calculated and measured profiles.

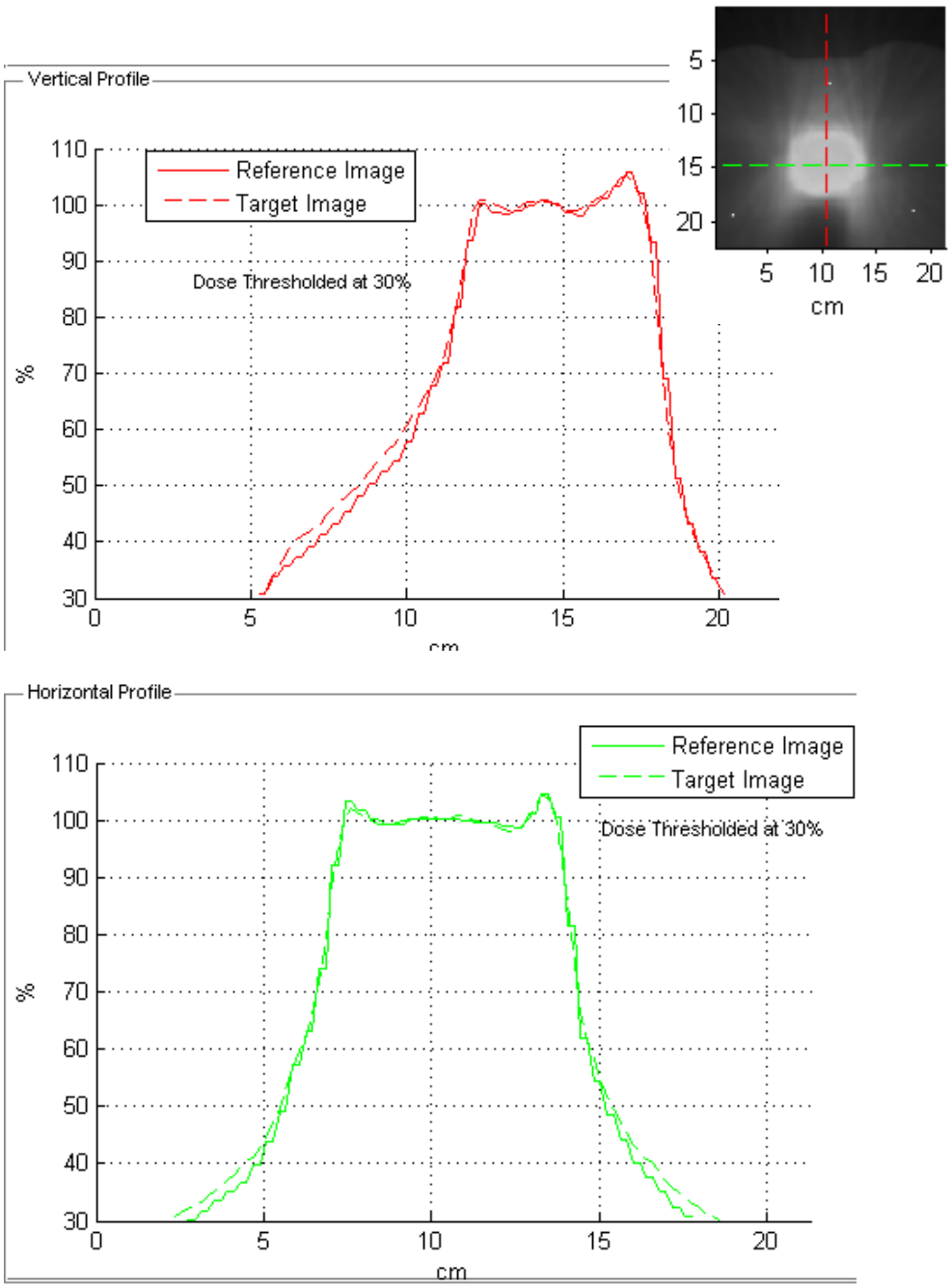

Figure 64: Horizontal and Vertical profiles for RANDO prostate patient 9. Horizontal and vertical profiles spatially evaluate the dose distribution between the calculated and measured profiles.

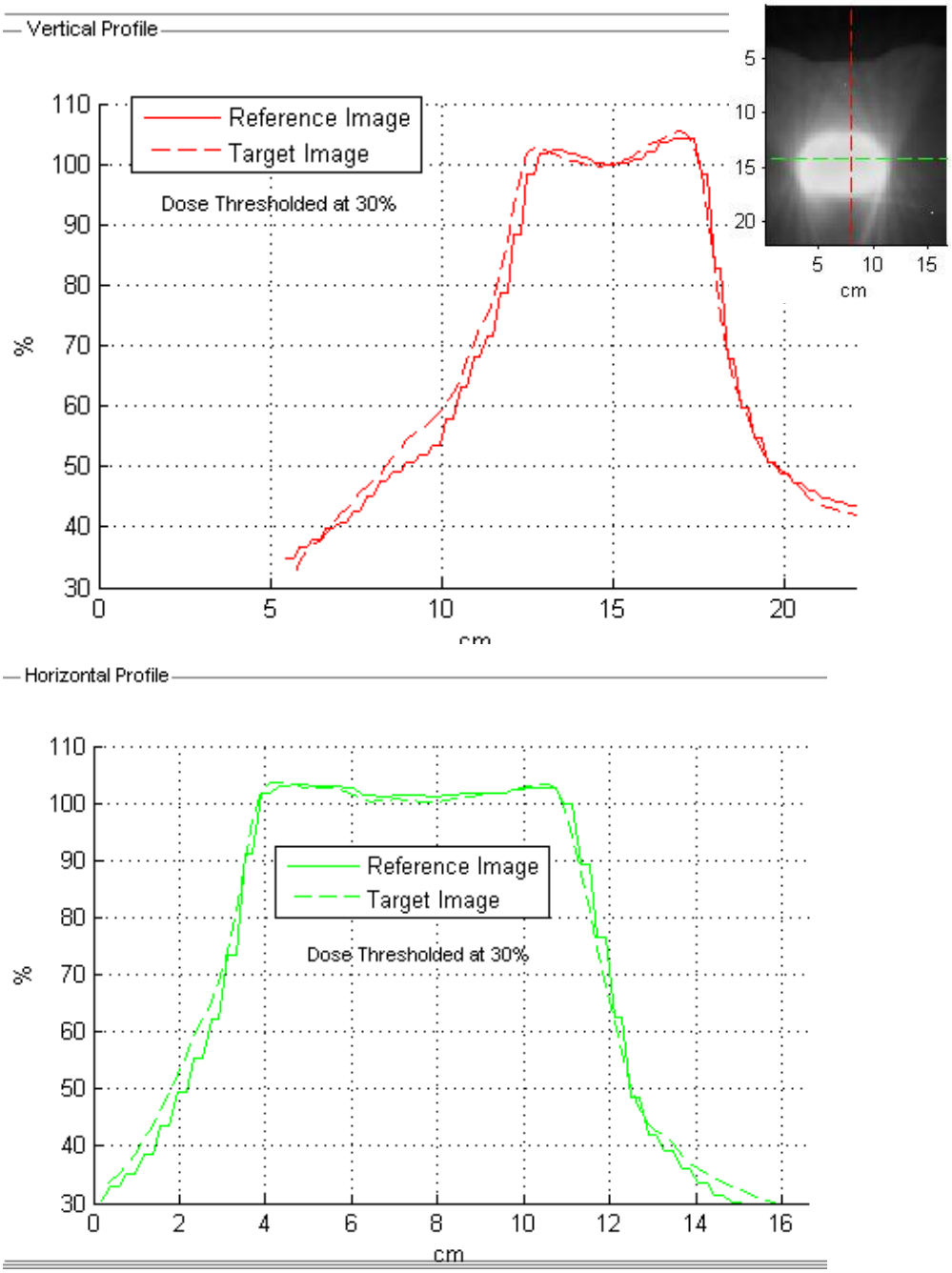

Figure 65: Horizontal and Vertical profiles for RANDO prostate patient 10. Horizontal and vertical profiles spatially evaluate the dose distribution between the calculated and measured profiles.

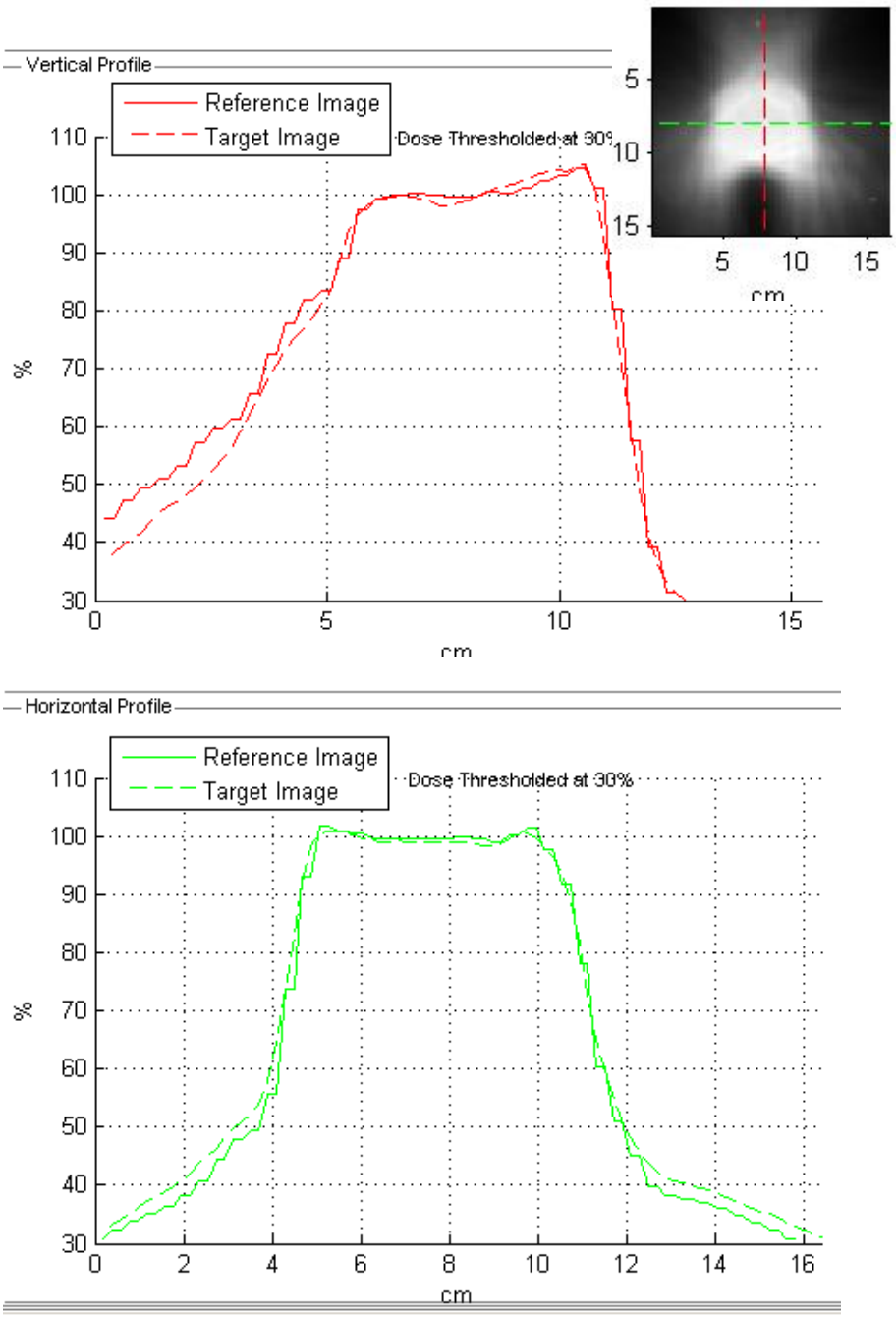

Figure 66: Horizontal and Vertical profiles for RANDO prostate patient 11. Horizontal and vertical profiles spatially evaluate the dose distribution between the calculated and measured profiles.

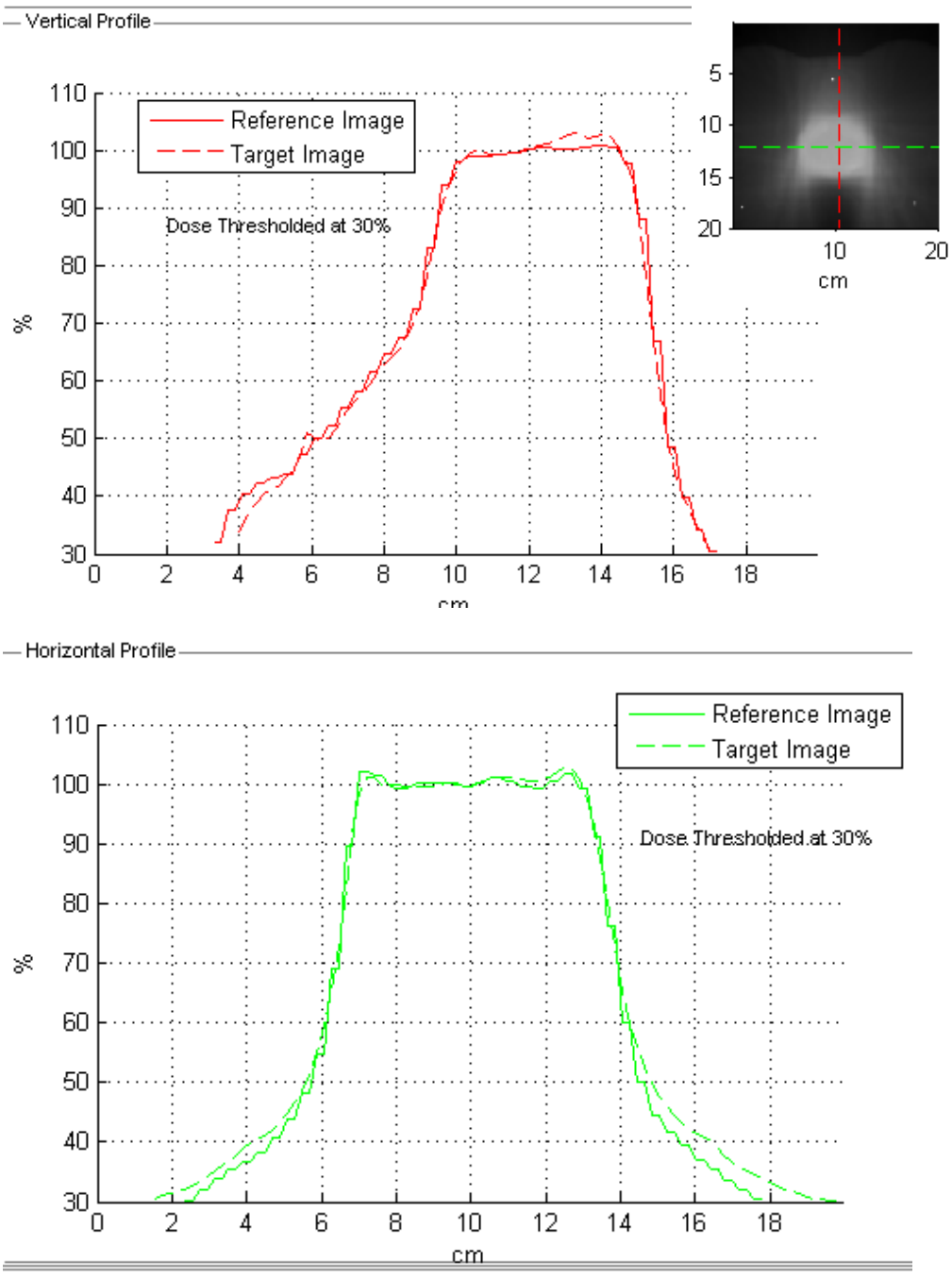

Figure 67: Horizontal and Vertical profiles for RANDO prostate patient 12. Horizontal and vertical profiles spatially evaluate the dose distribution between the calculated and measured profiles.

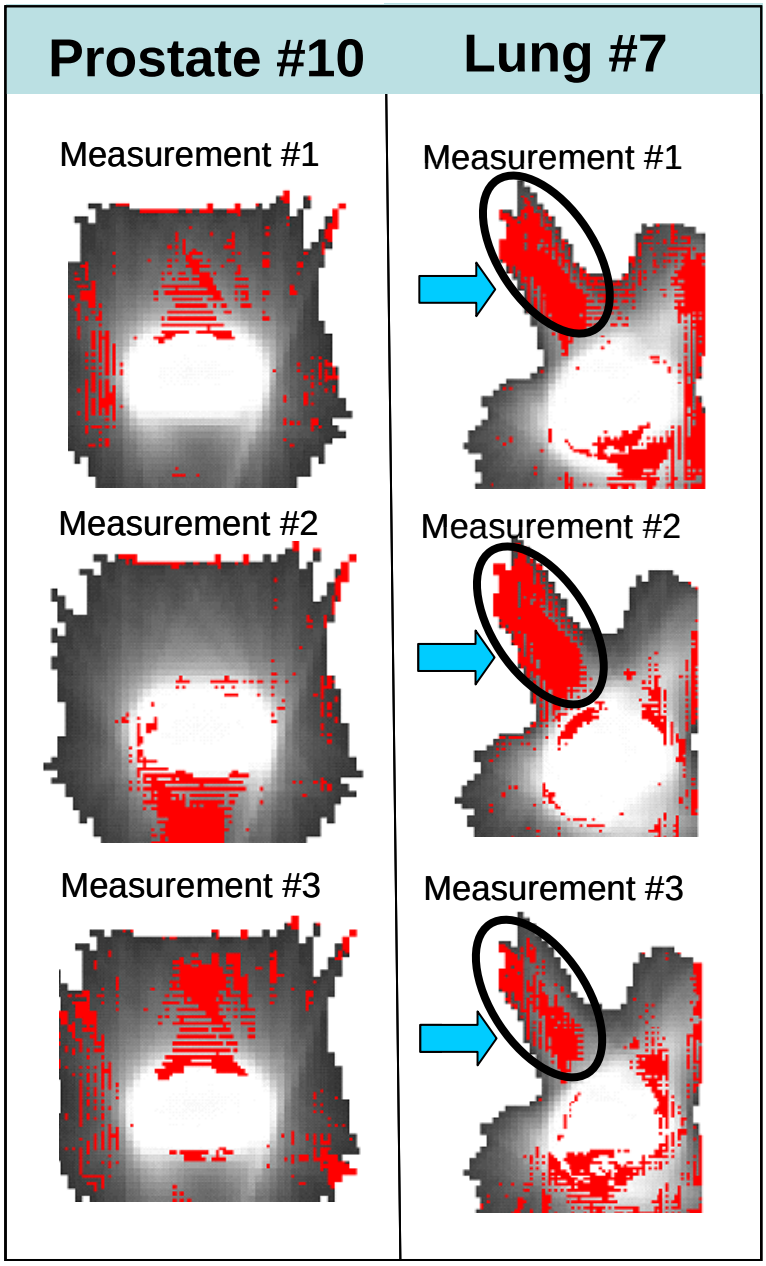

Figure 68: Repeat measurements for one prostate and one lung patient testing film reproducibility using the RANDO phantom.

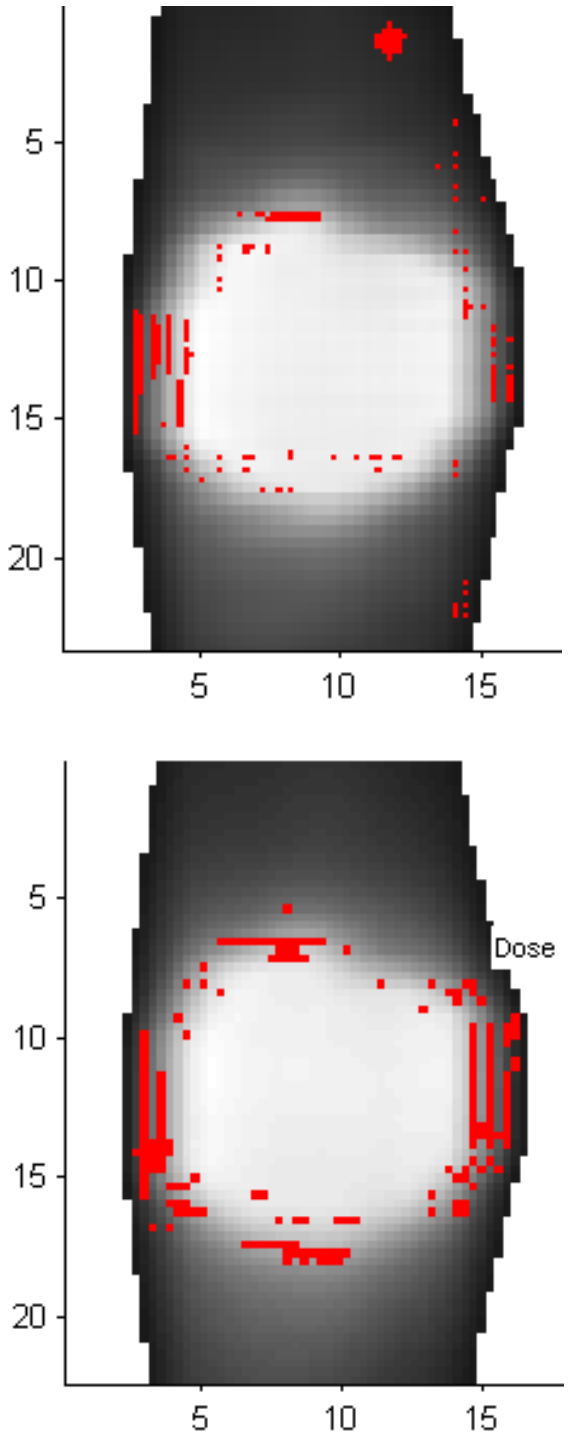

Figure 69: Gamma Pass/Fail diagram for MatriXX study patient 1 using a 3mm DTA and 3% dose difference tolerance. The modality being tested in the top image is Kodak EDR2 film. The modality being tested in the bottom image is the MatriXX detector.

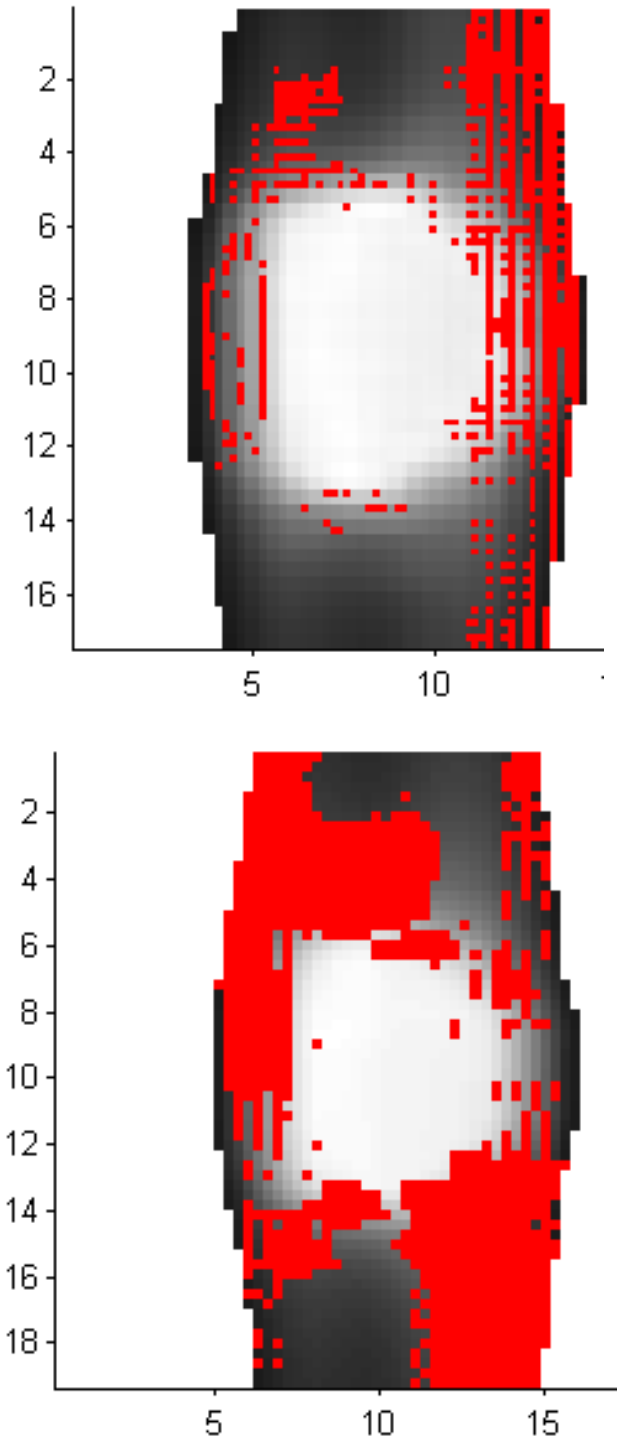

Figure 70: Gamma Pass/Fail diagram for MatriXX study patient 2 using a 3mm DTA and 3% dose difference tolerance. The modality being tested in the top image is Kodak EDR2 film. The modality being tested in the bottom image is the MatriXX detector.

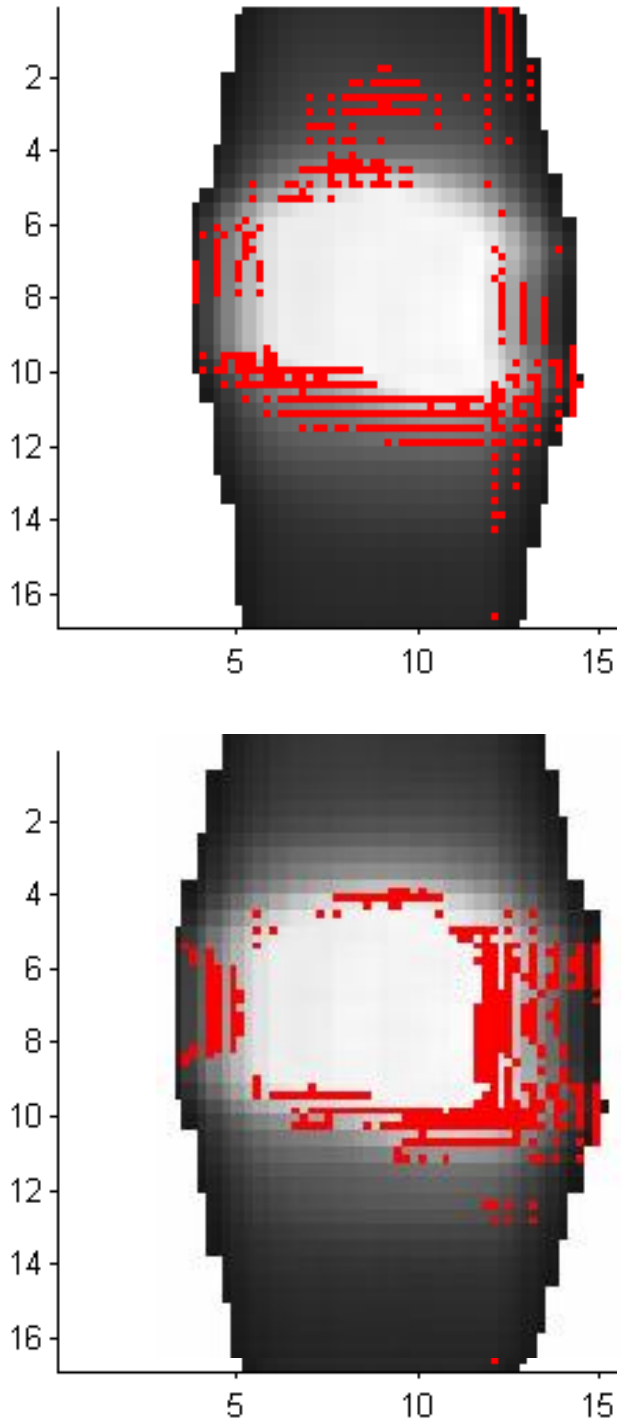

Figure 71: Gamma Pass/Fail diagram for MatriXX study patient 3 using a 3mm DTA and 3% dose difference tolerance. The modality being tested in the top image is Kodak EDR2 film. The modality being tested in the bottom image is the MatriXX detector.

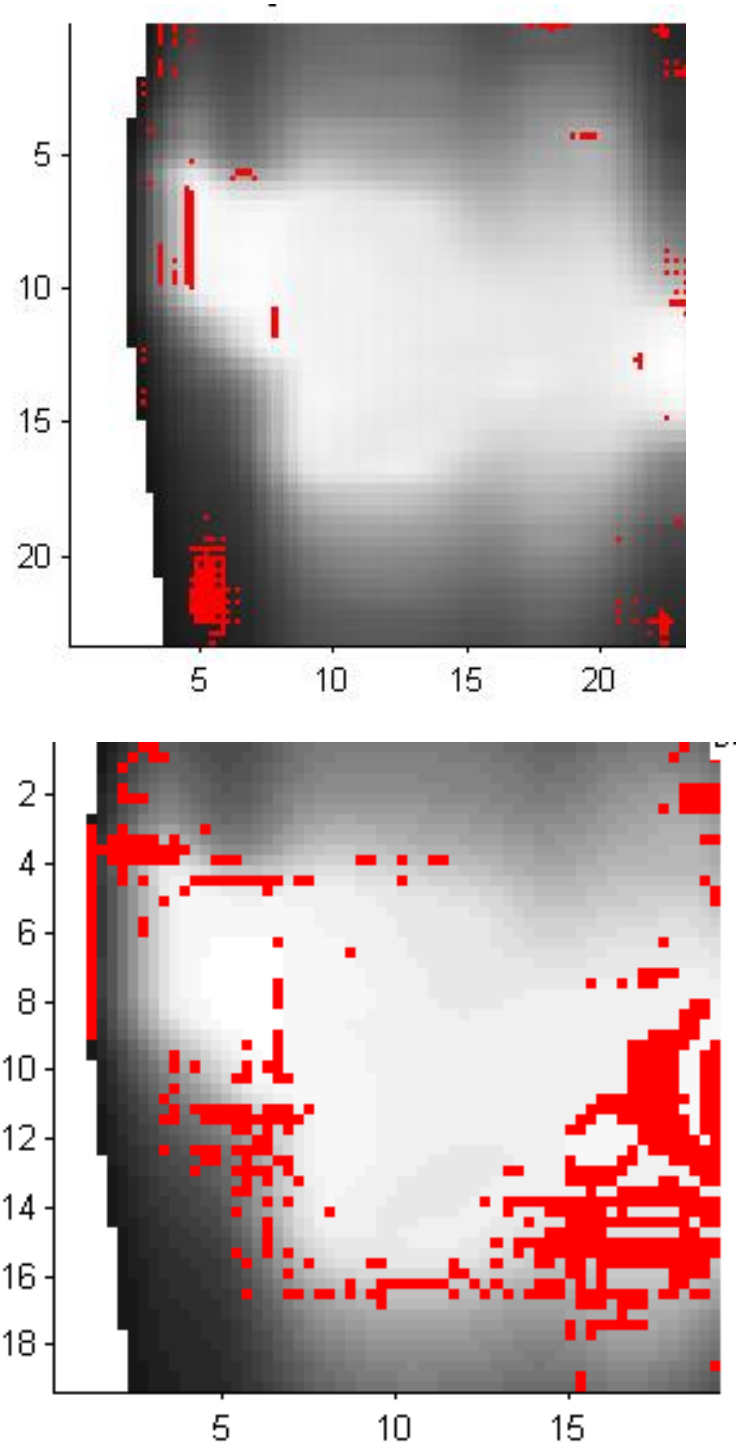

Figure 72: Gamma Pass/Fail diagram for MatriXX study patient 4 using a 3mm DTA and 3% dose difference tolerance. The modality being tested in the top image is Kodak EDR2 film. The modality being tested in the bottom image is the MatriXX detector.

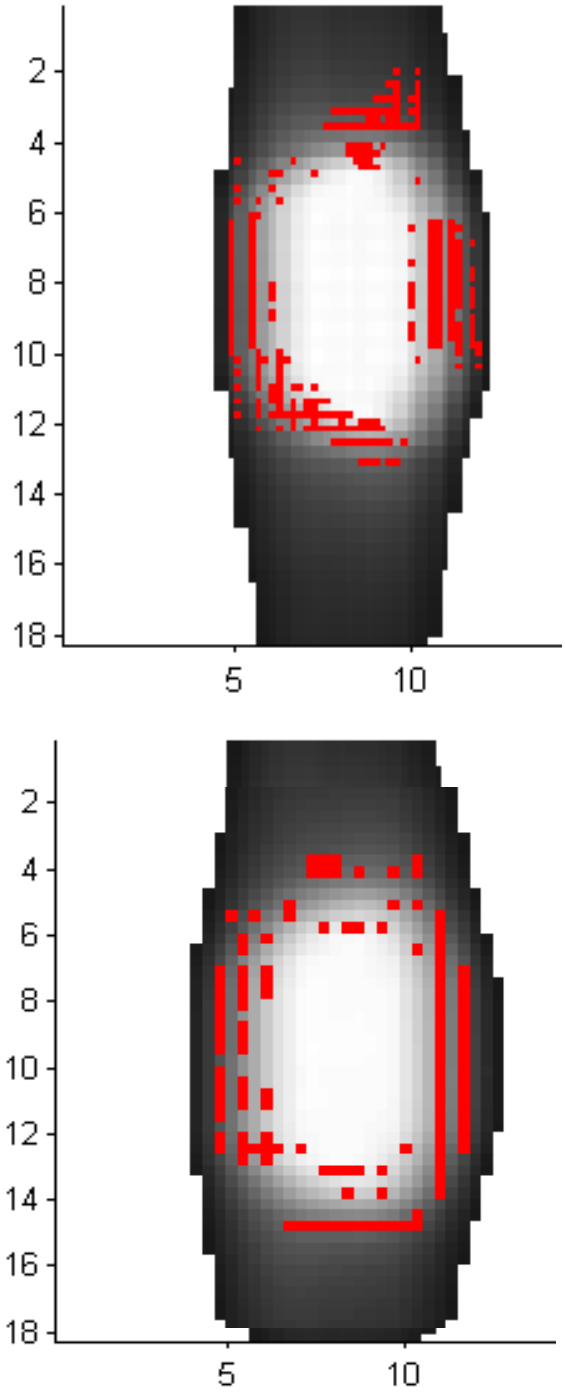

Figure 73: Gamma Pass/Fail diagram for MatriXX study patient 5 using a 3mm DTA and 3% dose difference tolerance. The modality being tested in the top image is Kodak EDR2 film. The modality being tested in the bottom image is the MatriXX detector.

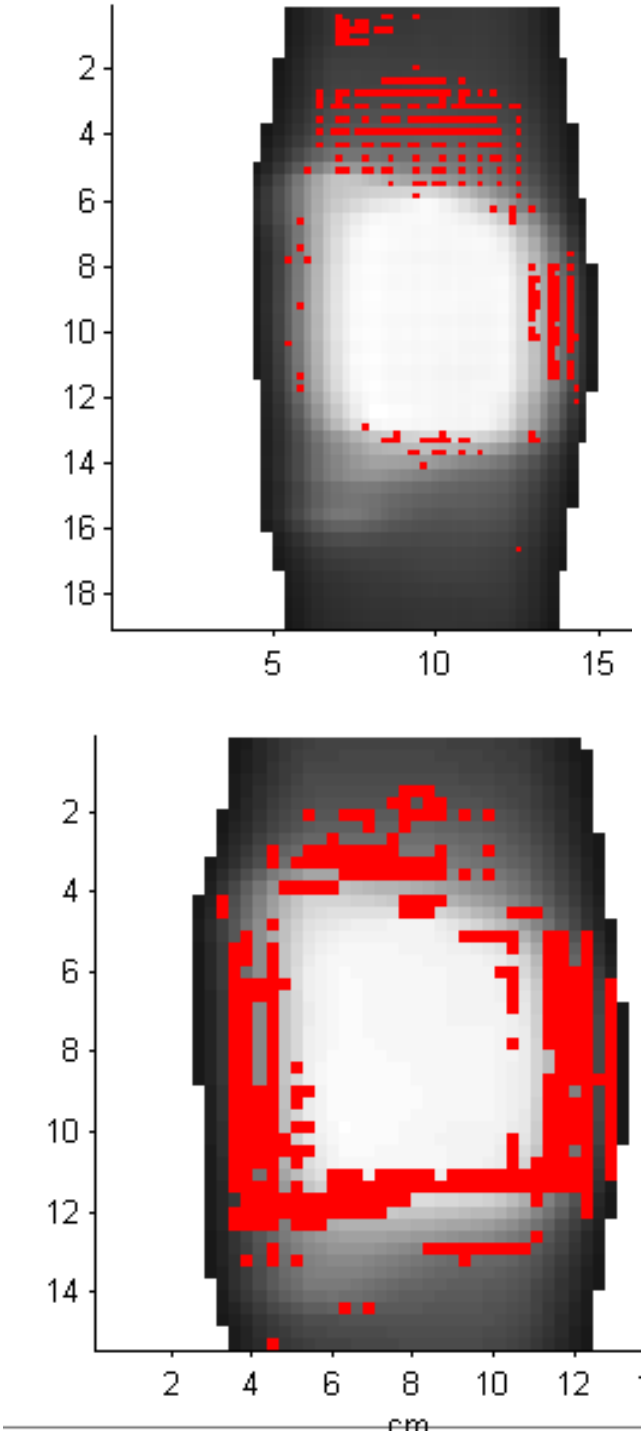

Figure 74: Gamma Pass/Fail diagram for MatriXX study patient 6 using a 3mm DTA and 3% dose difference tolerance. The modality being tested in the top image is Kodak EDR2 film. The modality being tested in the bottom image is the MatriXX detector.

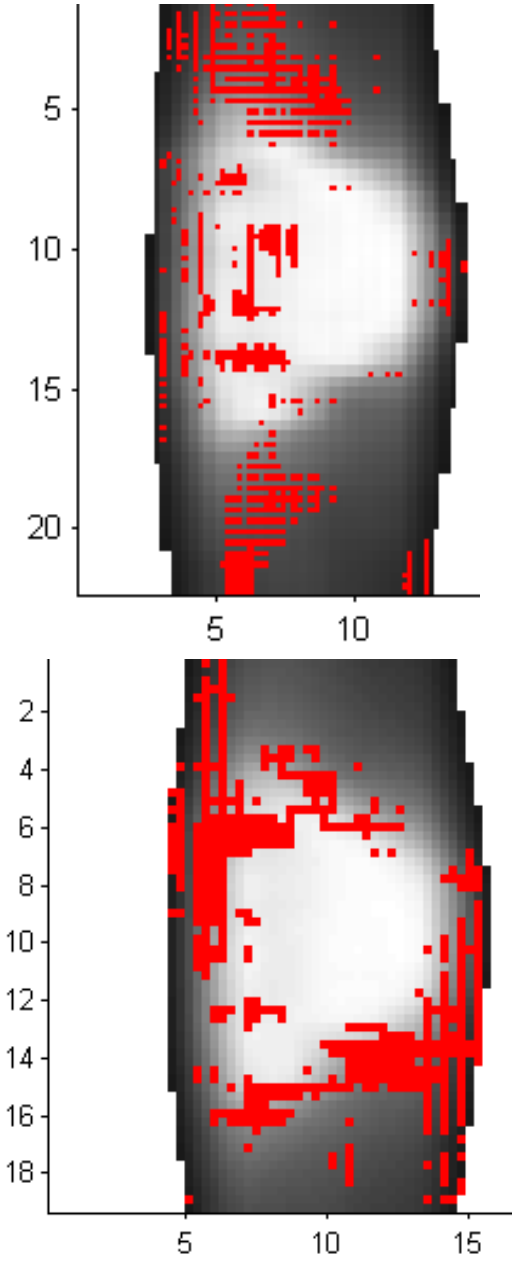

Figure 75: Gamma Pass/Fail diagram for MatriXX study patient 7 using a 3mm DTA and 3% dose difference tolerance. The modality being tested in the top image is Kodak EDR2 film. The modality being tested in the bottom image is the MatriXX detector.

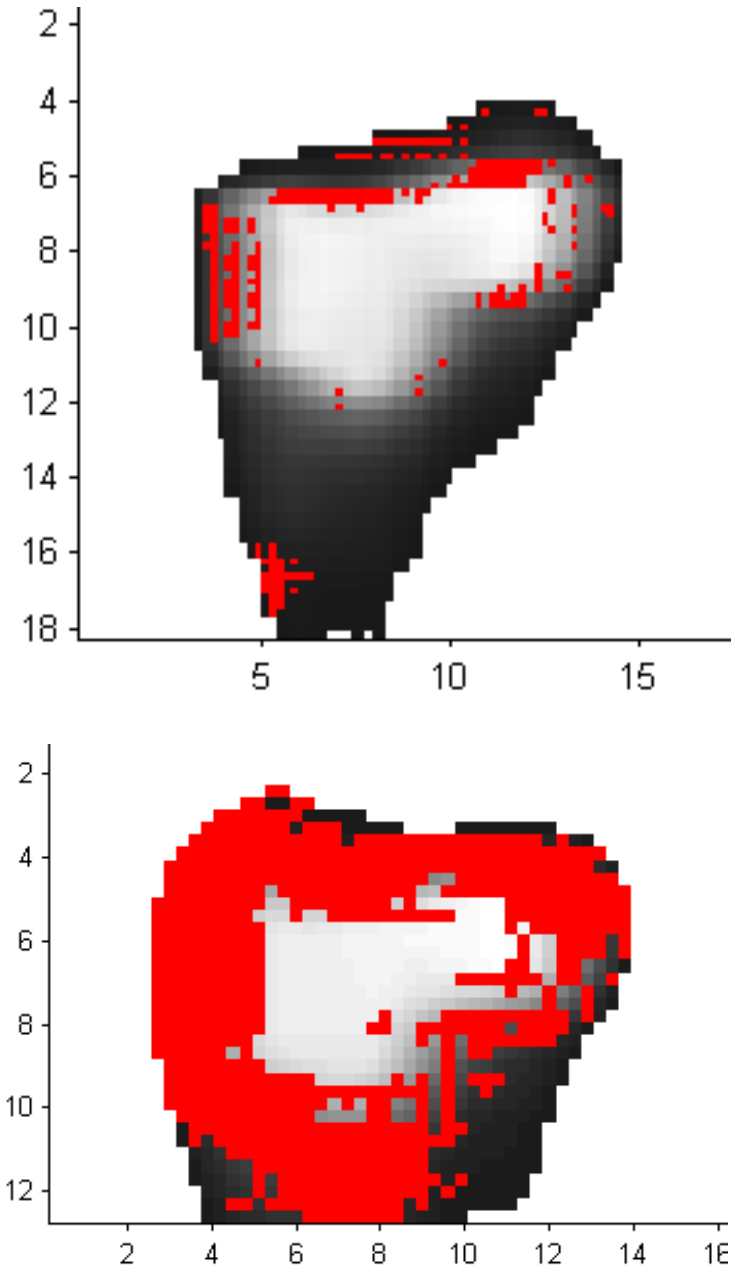

Figure 76: Gamma Pass/Fail diagram for MatriXX study patient 8 using a 3mm DTA and 3% dose difference tolerance. The modality being tested in the top image is Kodak EDR2 film. The modality being tested in the bottom image is the MatriXX detector.

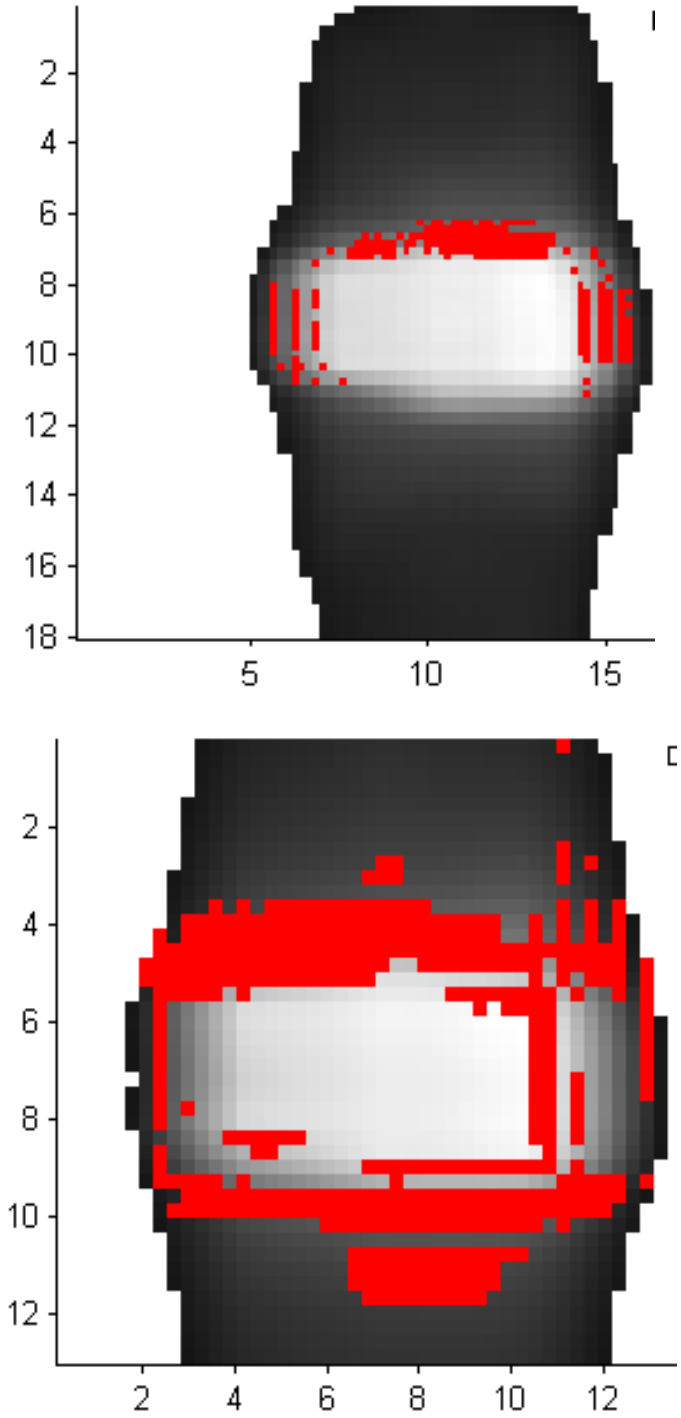

Figure 77: Gamma Pass/Fail diagram for MatriXX study patient 9 using a 3mm DTA and 3% dose difference tolerance. The modality being tested in the top image is Kodak EDR2 film. The modality being tested in the bottom image is the MatriXX detector.

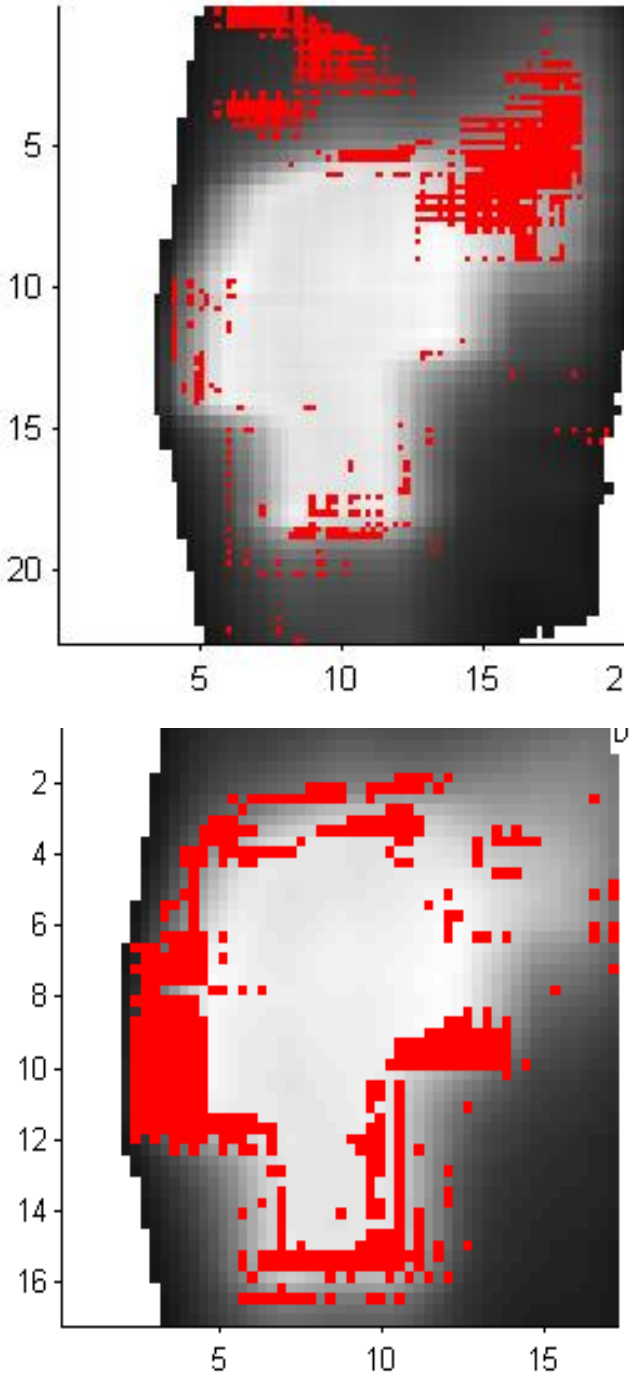

Figure 78: Gamma Pass/Fail diagram for MatriXX study patient 10 using a 3mm DTA and 3% dose difference tolerance. The modality being tested in the top image is Kodak EDR2 film. The modality being tested in the bottom image is the MatriXX detector.

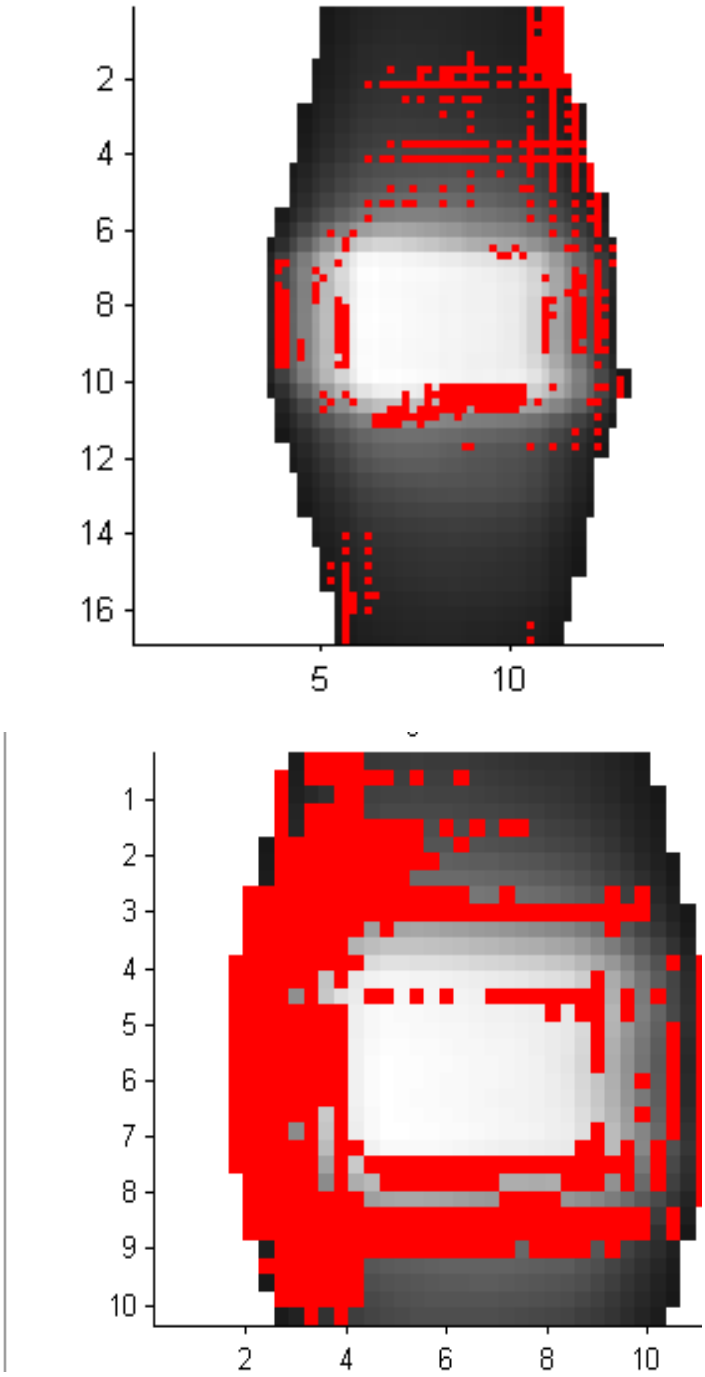

Figure 79: Gamma Pass/Fail diagram for MatriXX study patient 11 using a 3mm DTA and 3% dose difference tolerance. The modality being tested is Kodak EDR2 film. The analysis region was defined as the area of film receiving over 10% of the prescribed dose.

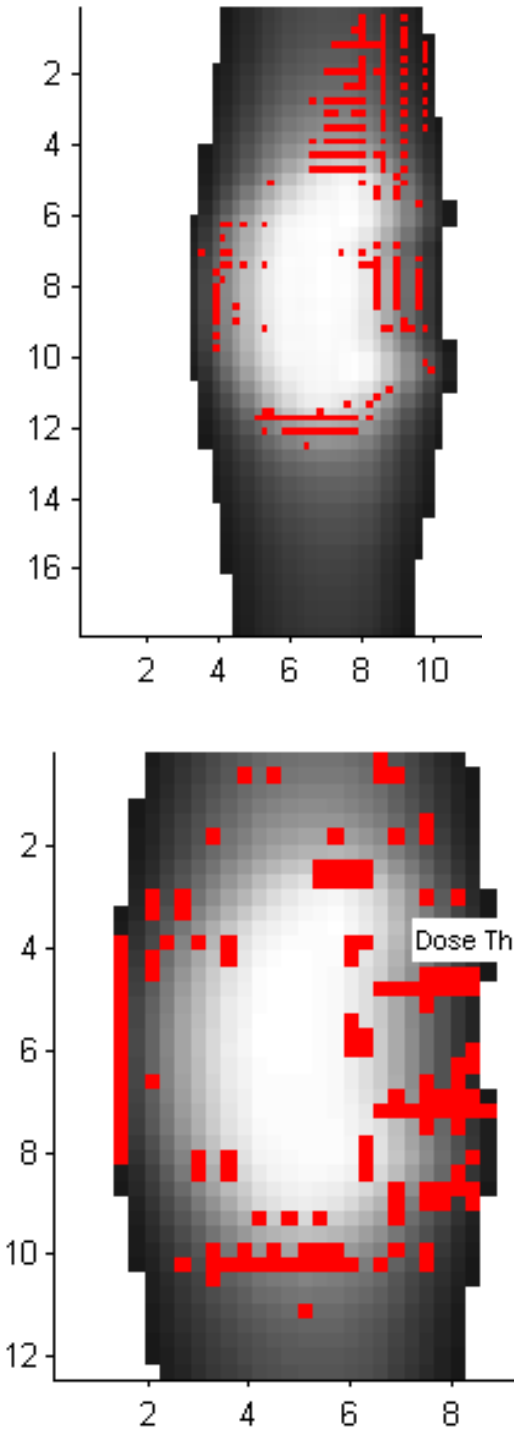

Figure 80: Gamma Pass/Fail diagram for MatriXX study patient 12 using a 3mm DTA and 3% dose difference tolerance. The modality being tested in the top image is Kodak EDR2 film. The modality being tested in the bottom image is the MatriXX detector.

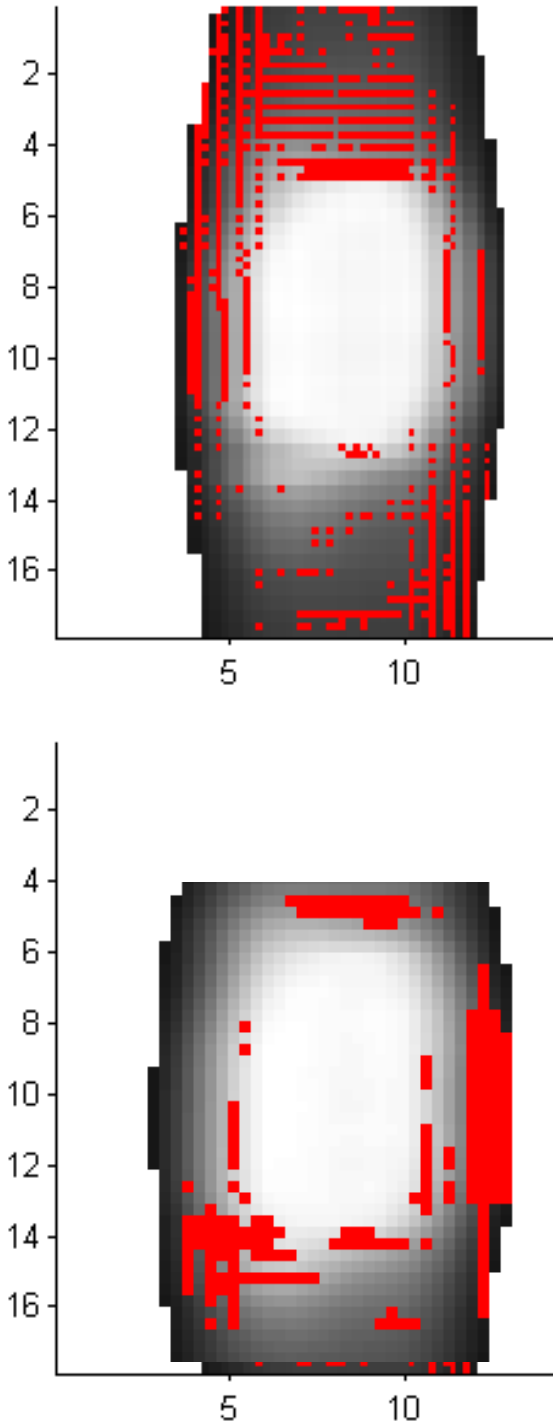

Figure 81: Gamma Pass/Fail diagram for MatriXX study patient 13 using a 3mm DTA and 3% dose difference tolerance. The modality being tested in the top image is Kodak EDR2 film. The modality being tested in the bottom image is the MatriXX detector.

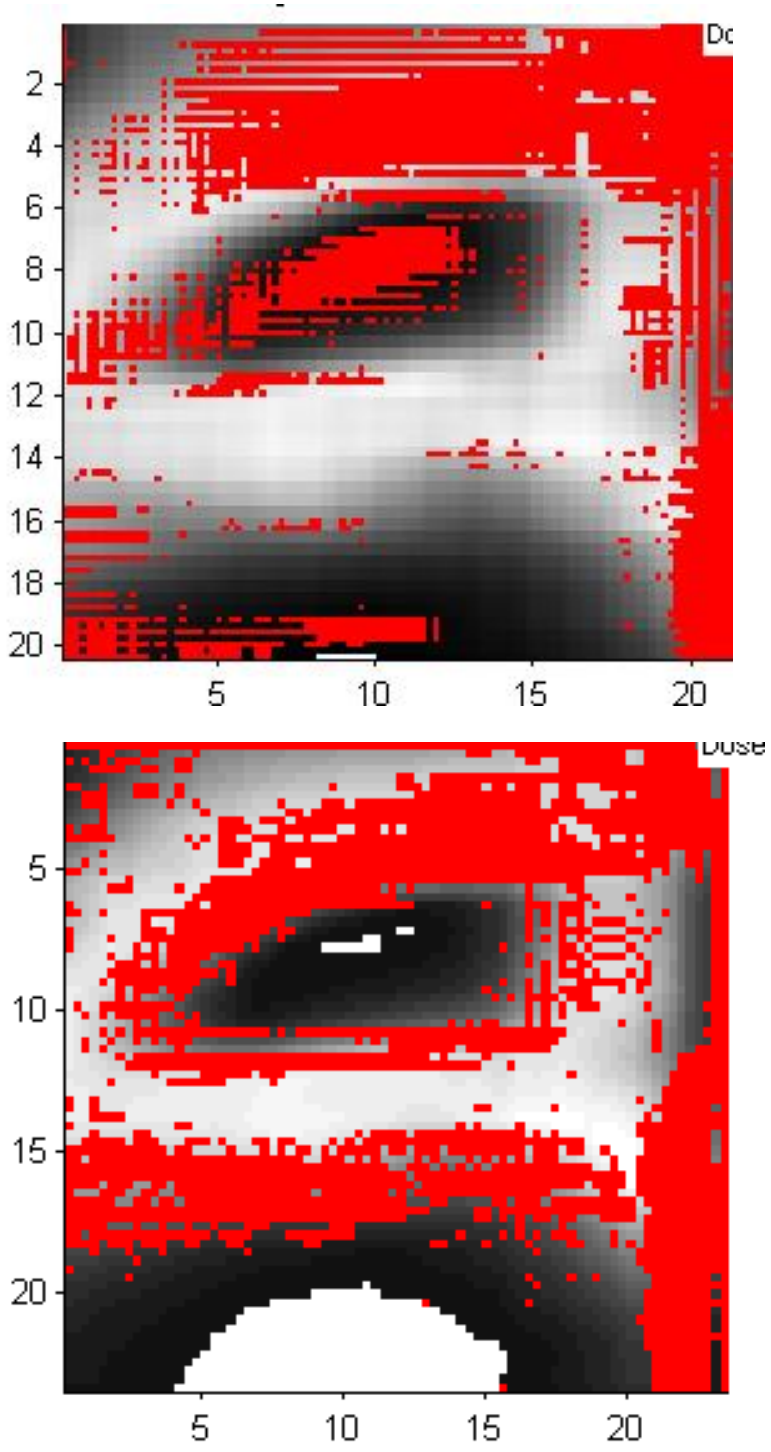

Figure 82: Gamma Pass/Fail diagram for MatriXX study patient 14 using a 3mm DTA and 3% dose difference tolerance. The modality being tested in the top image is Kodak EDR2 film. The modality being tested in the bottom image is the MatriXX detector.

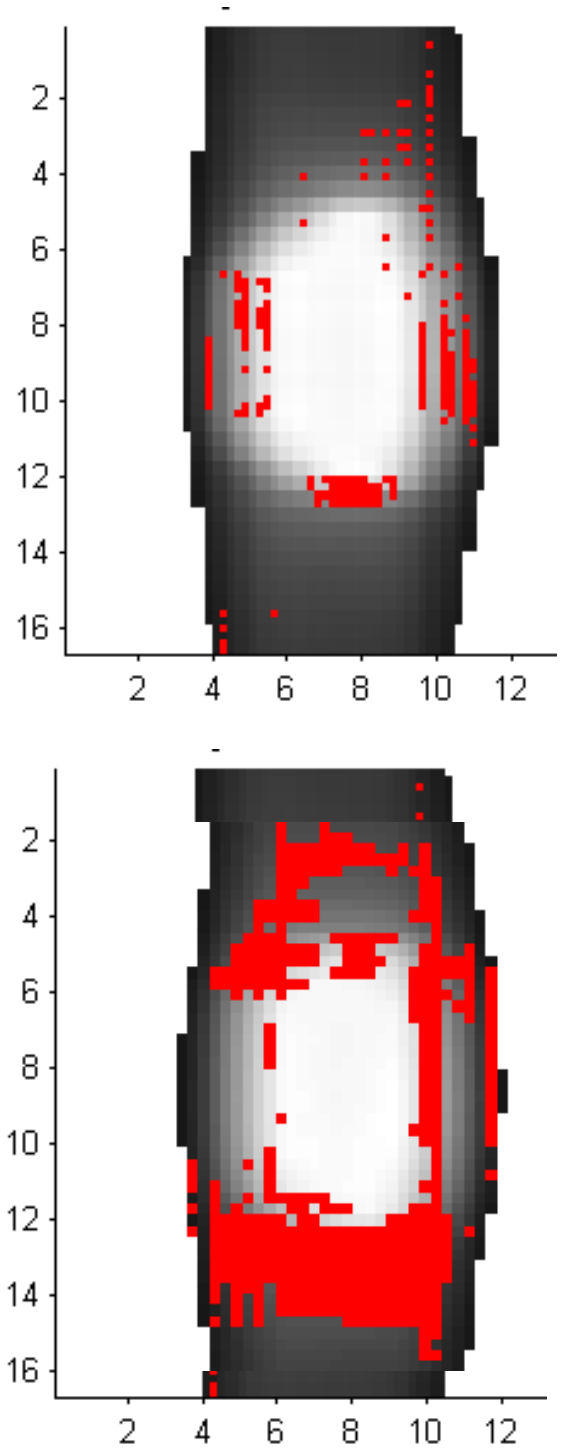

Figure 83: Gamma Pass/Fail diagram for MatriXX study patient 15 using a 3mm DTA and 3% dose difference tolerance. The modality being tested in the top image is Kodak EDR2 film. The modality being tested in the bottom image is the MatriXX detector.

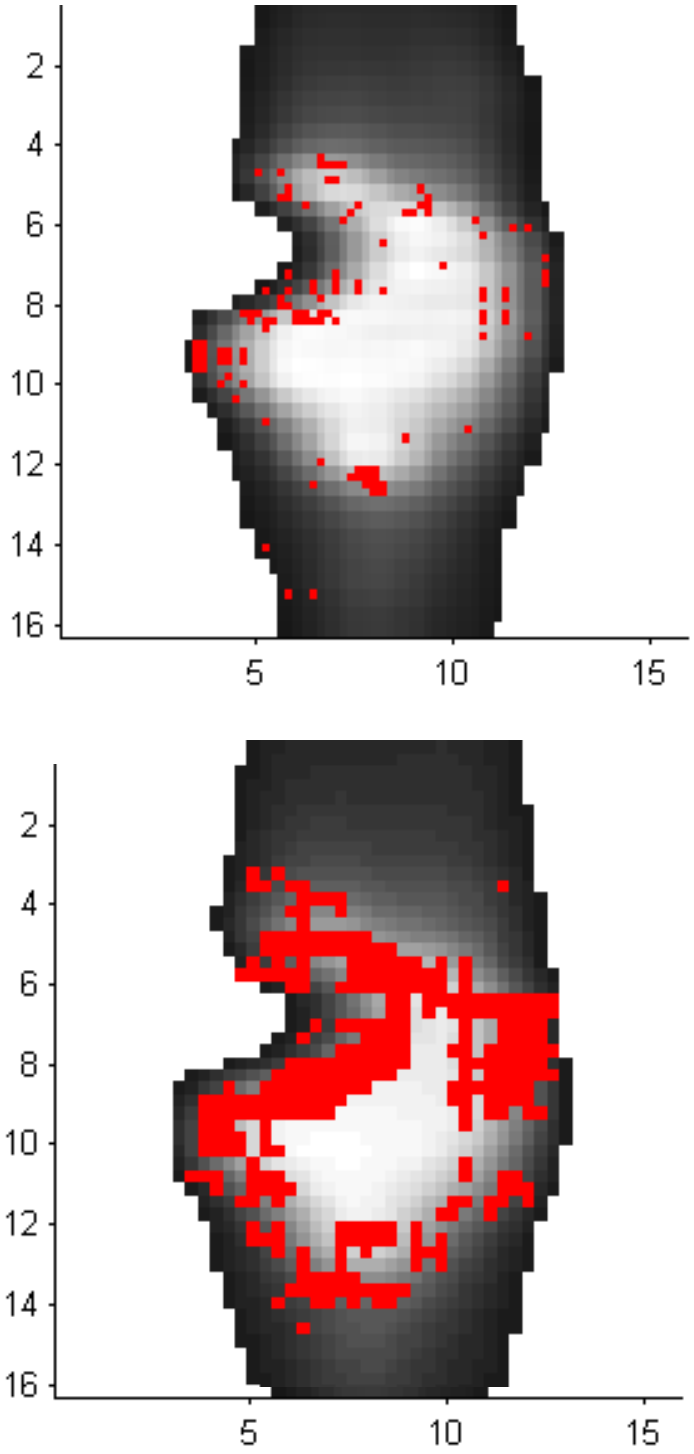

Figure 84: Gamma Pass/Fail diagram for MatriXX study patient 16 using a 3mm DTA and 3% dose difference tolerance. The modality being tested in the top image is Kodak EDR2 film. The modality being tested in the bottom image is the MatriXX detector.

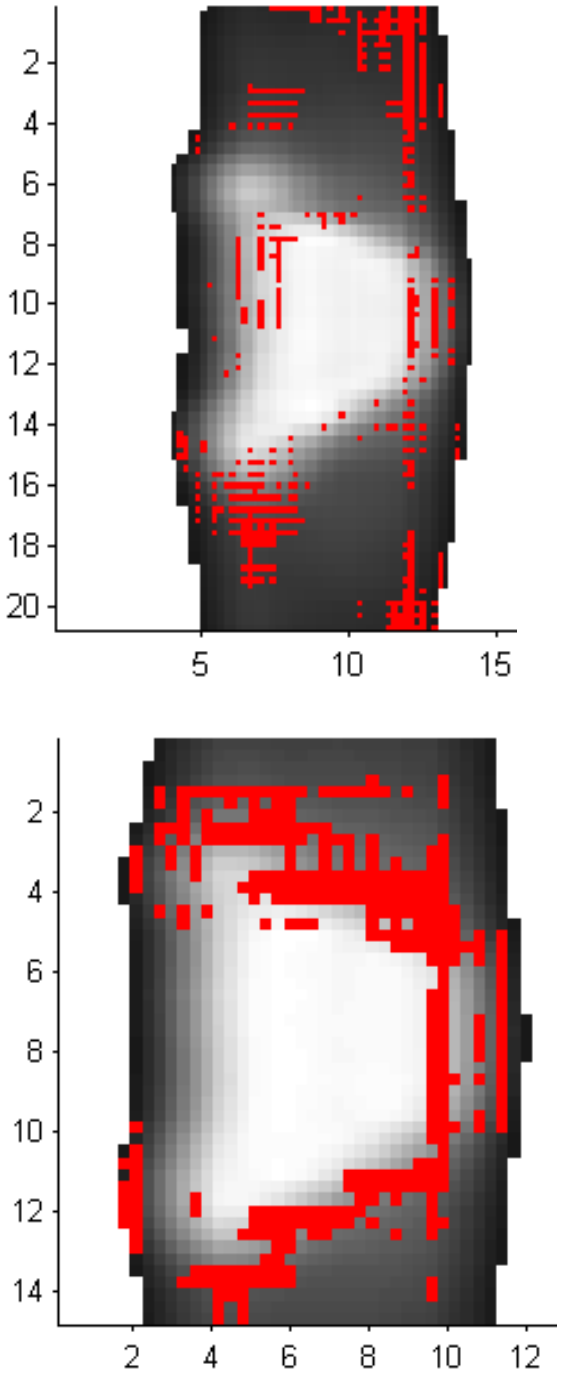

Figure 85: Gamma Pass/Fail diagram for MatriXX study patient 17 using a 3mm DTA and 3% dose difference tolerance. The modality being tested in the top image is Kodak EDR2 film. The modality being tested in the bottom image is the MatriXX detector.

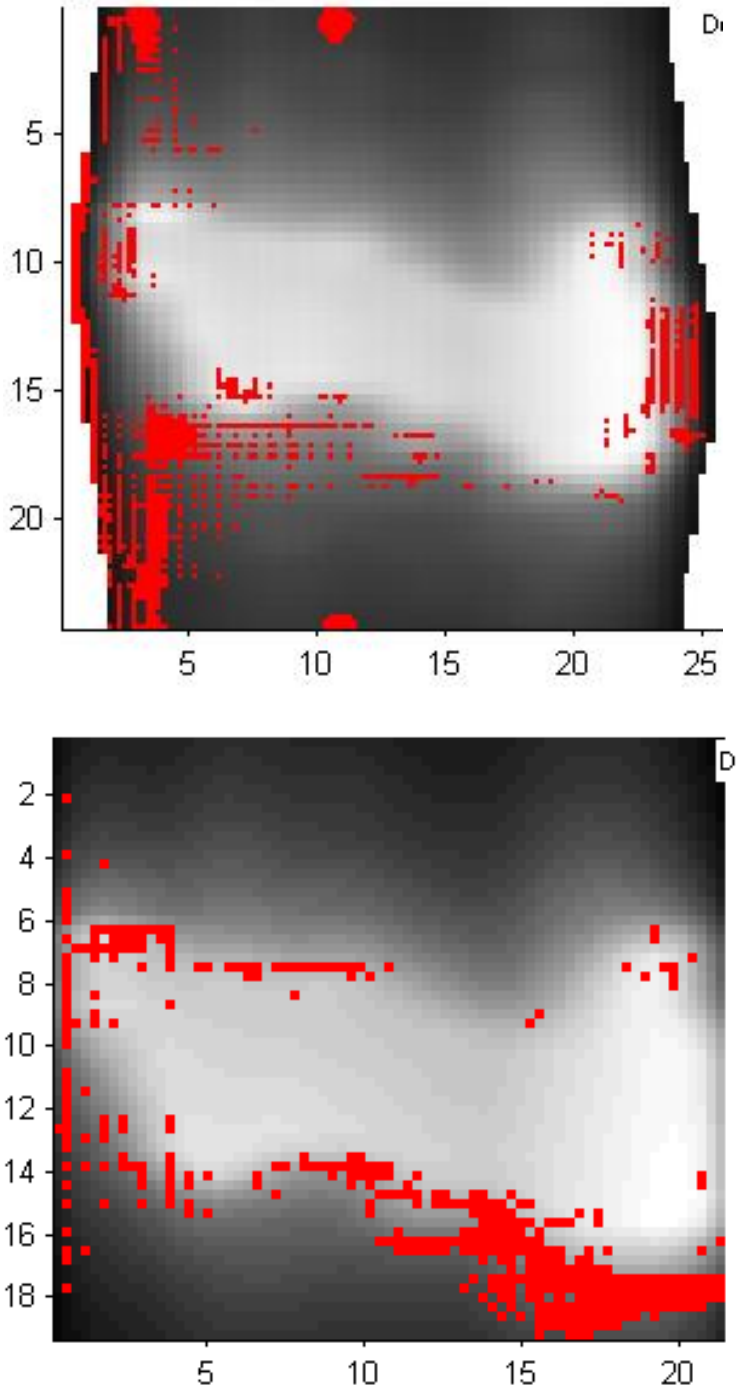

Figure 86: Gamma Pass/Fail diagram for MatriXX study patient 18 using a 3mm DTA and 3% dose difference tolerance. The modality being tested in the top image is Kodak EDR2 film. The modality being tested in the bottom image is the MatriXX detector.

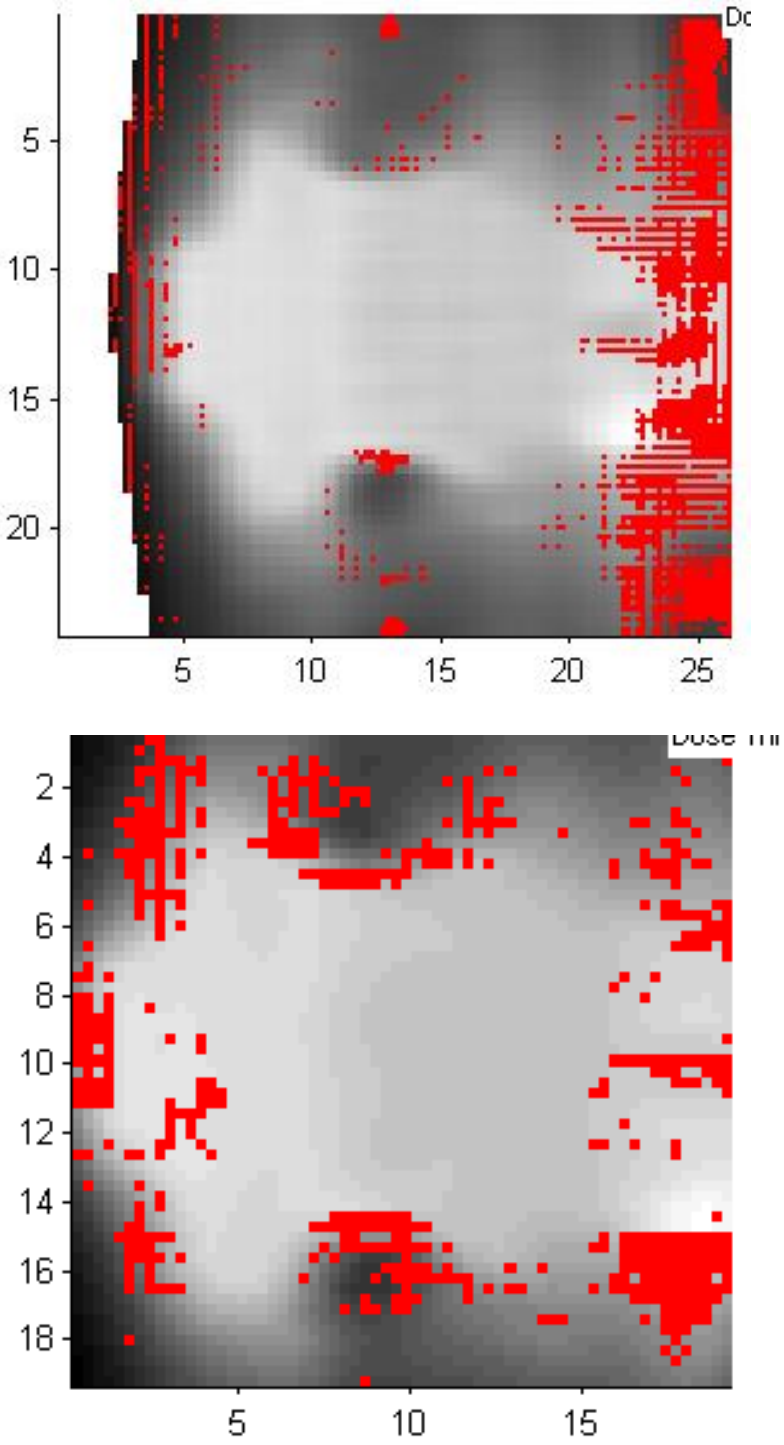

Figure 87: Gamma Pass/Fail diagram for MatriXX study patient 19 using a 3mm DTA and 3% dose difference tolerance. The modality being tested in the top image is Kodak EDR2 film. The modality being tested in the bottom image is the MatriXX detector.

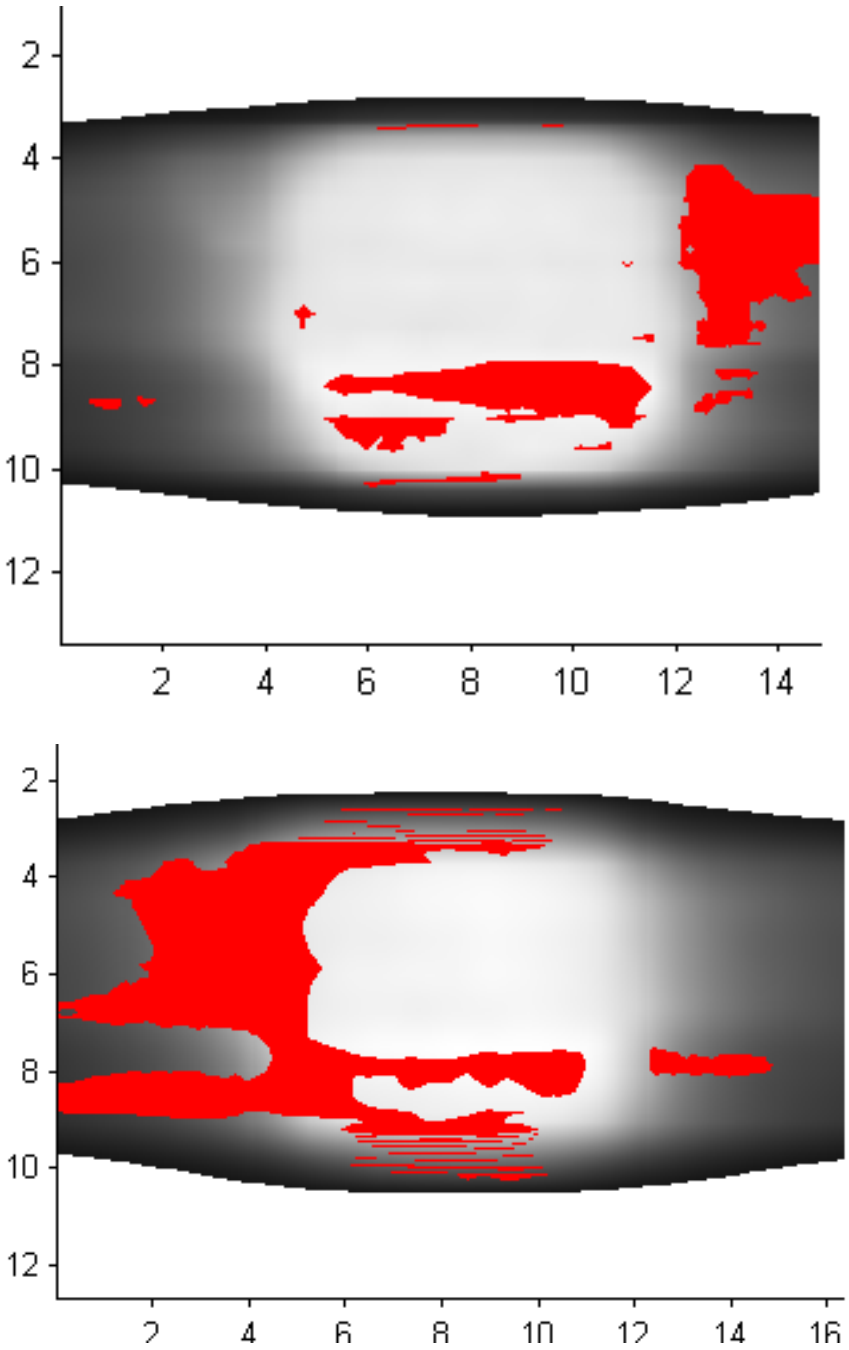

Figure 88: Gamma Pass/Fail diagram for MatriXX study patient 20 using a 3mm DTA and 3% dose difference tolerance. The modality being tested in the top image is Kodak EDR2 film. The modality being tested in the bottom image is the MatriXX detector.

APPENDIX II - Tables

Table 1 : The mean gamma index and the percent of pixels exceeding the gamma threshold with analysis criteria of 3mm DTA and 3% dose difference tolerance for the 24 RANDO phantom study patients.

	Lung Test Cases	
Patient Number	Mean Gamma Index	Percent Exceeding Gamma
1	0.82	30%
2	0.79	31%
3	0.71	23%
4	0.63	13%
5	1.13	49%
6	0.87	29%
7	0.82	30%
8	0.55	10%
9	0.64	16%
10	0.77	27%
11	4.57	55%
12	0.59	12%

	Prostate Test Cases	
Patient Number	Mean Gamma Index	Percent Exceeding Gamma
1	0.55	6%
2	0.61	18%
3	0.62	14%
4	0.67	18%
5	0.65	19%
6	0.69	20%
7	0.55	9%
8	0.72	24%
9	0.57	8%
10	0.55	10%
11	0.74	23%
12	0.50	5%

Table 2: The percent of pixels exceeding the gamma threshold with analysis criteria of 3mm DTA and 3% dose difference tolerance for the 20 MatriXX study patients.

Patient	Film	MatriXX
1	2.7%	5.8%
2	18.7%	45.1%
3	10.6%	8.6%
4	9.9%	13.9%
5	9.4%	10.2%
6	6.1%	21.5%
7	12.4%	21.7%
8	8.8%	58.4%
9	5.2%	26.9%
10	10.9%	17.2%
11	13.3%	42.2%
12	7.1%	13.8%
13	17.8%	15.5%
14	33.1%	44.1%
15	5.8%	32.6%
16	3.5%	23.1%
17	10.5%	21.7%
18	7.7%	8.7%
19	12.6%	13.4%
20	11.8%	22.8%
Average	10.8%	23.4%
Stdev	6.7%	13.8%

VITA

Michelle Neeley was raised in Lilburn, GA just outside of Atlanta. She received her Bachelor of Science degree in Physics from North Georgia College and State University in Dahlonega, GA in 2004. She spent the next three years traveling with her husband while he furthered his career as a Navy pilot. In 2007, Michelle returned to school at The University of Tennessee to obtain her Master's Degree in Physics with a concentration in Medical Physics. She received her Master's Degree in 2009, and looks forward to her new career as a Medical Physicist.